ABSTRACT

Title of Dissertation:	DEVELOPMENT OF A HYBRID 3D PRINTING STRATEGY FOR NIPPLE RECONSTRUCTION
	Sarah Miho Van Belleghem, Doctor of Philosophy, 2020
Dissertation directed by:	Fischell Family Distinguished Professor & Department Chair, John P. Fisher, Fischell Department of Bioengineering

Breast cancer and its most radical treatment, the mastectomy, significantly impose both physical transformations and emotional pain in thousands of women across the globe. Although reconstructive surgery is viewed as a possible recovery route for a lost symmetry and gender identity, it provides these patients with a breast mound whose most notable feature is scarring from the initial invasive procedure. Restoring the appearance of a nipple-areola complex directly on the breast represents an important psychological healing experience for these women and remains an unresolved clinical challenge, as current restorative techniques using Skin Flap Suturing (SFS) renders a flattened disfigured skin tab within a single year and requires subsequent surgeries. A tissue-engineered scaffold designed to integrate with the breast skin can not only aid in the development of a more robust and aesthetically pleasing nipple but can also aid in minimizing the patients' prominent

mastectomy scars. As 3D printing has become a popular and advantageous way to produce scaffolds with complex, patient-specific structures, this technology holds great promise for the fabrication of custom shaped nipple-areola grafts per any breast size. The work presented here is aimed at the development of a hybrid scaffold, composed of complementary biodegradable and synthetic hydrogels, that fosters the regeneration of a viable dermal layer in the form of a nipple-areola complex. The first aim of this research defined a dynamic dual bioink 3D printing strategy to produce soft tissue grafts that allow for enhanced host integration and volume retention. A new shape analysis technique utilizing CloudCompare software was also demonstrated to expand our available toolbox for assessing scaffold aesthetic properties. We then extended both modular printing and shape assessment techniques to the fabrication of a nipple-areola scaffold in the second aim, where both structural and bioactive components of the design were further adjusted. Lastly, the third aim explored the immune and vascular responses to these hybrid materials in a rigorous evaluation of an *in vivo* rat subcutaneous implantation study. Envisioned as subdermal implants, these nipple-areola bioprinted scaffolds have the potential to reduce subsequent surgical intervention by creating a lasting nipple-areola structure that harmoniously coexists with the patient's breast skin. The proposed system can be applied to current breast reconstruction practices post patient healing of silicone implantation.

DEVELOPMENT OF A HYBRID 3D PRINTING STRATEGY FOR NIPPLE RECONSTRUCTION

by

Sarah Miho Van Belleghem

Dissertation submitted to the Faculty of the Graduate School of the
University of Maryland, College Park, in partial fulfillment
of the requirements for the degree of
Doctor of Philosophy
2020

Advisory Committee:
Professor John P. Fisher, Chair
Professor Peter Kofinas, Dean's Representative
Associate Professor Helim Aranda-Espinoza
Assistant Professor Kimberly Stroka
Associate Professor Arthur Jung Nam

Dedication

To my mom, Audrey.

From the beginning, you have helped focus my energetic fervor for science into a field that is in desperate need of innovation. Your passion for developing and mentoring women in technology has deeply inspired every project idea- from MIT, to UMD, and will continue to beyond. You constantly encourage me to pursue my dreams and support me through every high and low point throughout this journey. You inspire me to be a better person, for all women and men, in this lifetime.

This one's for you, Mom!

Acknowledgements

I would love to thank my advisor, Dr. John P Fisher, for supporting every kooky project idea throughout the years and for generously supporting this dissertation project. I would also like to thank my committee members: Dr. Peter Kofinas, for an incredibly special mentorship; Dr. Helim Aranda-Espinoza, for the contagious excitement and guidance for the project; Dr. Kimberly Stroka, for being an inspiring female role model that helped center the scientific question of this work; and Dr. Arthur Nam, for enthusiastically joining our team and dedicating so many hours to show the clinical potential of this idea. The completion of this work definitely 'took a village', and I am so fortunate to lean on such talented friends and lab mates in the Tissue Engineering and Biomaterials Lab and the BIOE department. A special thank you to Kirstie Snodderly, Bhushan Mahadik, Zoe Mote, Arley Wolfand, and Leopoldo Torres Jr for their hard work and contributions to our publications. Finally, a huge thank you to my family for rallying behind me all these years!

Table of Contents

Dedication ii
Acknowledgements iii
Table of Contents iv
List of Tables vi
List of Figures vii
Chapter 1: Introduction to Nipple Reconstruction 1
1.1 Breast Cancer and its Threat on Nipple Tissue Health 1
1.2 Psychological Effects of Mastectomy 5
1.3 Skin Flap Suturing and its Common Setbacks 7
1.4 Engineering Nipple Tissue 11
1.4.1 Autologous Materials 12
1.4.2 Alloplastic Materials 13
1.4.3 Decellularized Matrices 14
1.4.4 Synthetic Materials 16
1.5 Conclusion 16
1.6 Dissertation Work Overview 17
Chapter 2: Recent Developments in Soft Tissue Engineering 19
2.1 Challenges that Accompany Autologous Grafts and Soft Tissue Implants 19
2.2 Common Scaffold Fabrication Methods Utilized in Soft Tissue Engineering . 21
2.2.1 Conventional Porogen Leaching 22
2.2.2 Hydrogel Casting 23
2.2.3 Synthetic Fiber Electrospinning 24
2.2.4 Additive Manufacturing 25
2.3 Current Setbacks in Extrusion Printing for Soft Tissue Engineering 29
Chapter 3: Hybrid 3D Printing of Synthetic and Cell-Laden Bioinks for Shape Retaining Soft Tissue Grafts 31
3.1 Introduction 31
3.2 Materials and Methods 33
3.3 Results and Discussion 38
3.3.1 Double Network Support Structure 38
3.3.2 Hybrid Printing 43
3.3.3 Scaffold Aesthetic Properties Mapped with CloudCompare 46
3.5 Conclusion 51
Chapter 4: Orchestrated Structural and Bioactive Matrices for Engineering a Nipple-Areola Construct 53
4.1 Introduction 53
4.2 Materials and Methods 55
4.3 Results and Discussion 60
4.3.1 Synthetic Ink Modification for *In Vivo* Application 60
4.3.2 *In Vitro* Nipple Implant Functionality 64
4.3.3 Nipple Projection Shape Retention 68
4.4 Conclusion 72
Chapter 5: Foreign Body Response to Hybrid Prints in a Rat Subcutaneous Model 73
5.1 Introduction 73

5.2 Methods and Materials 76
5.3 Results and Discussion 80
5.3.1 *In Vivo* Application of Hybrid 3D Printed Scaffolds 80
5.3.2 Cellular Characteristics of Surrounding Host Tissue 87
5.3.3 Tissue Characteristics of Surrounding Host Tissue 91
5.5 Conclusion 100
Chapter 6: Summary and Future Directions 101
6.1 Summary 101
6.2 Future Directions 104
6.2.1 Vascularization 105
6.2.2 Nipple-Areola Skin Graft 106
6.2.3 4D Bioprinting 109
Bibliography 111

List of Tables

Table 1.1. Documented SFS procedures by documented plastic surgeon……10

Table 5.1 Modifications to the ISO 10993-6 Standard. The cellular and tissue evaluation proposed by the *International Organization for Standardization* calls for the cell count of several inflammatory cells in each evaluated image (high powered 400X). Since the lowest magnification we were able to obtain was 20X, we tailored the analysis by redefining each score value, mimicking the terminology used in the ISO and included an additional section 'Degradation of Implant' to better describe how the host tissue is integrating with the degradable components of the hybrid scaffolds……81

List of Figures

Figure 1.1 Schematic Representation of Breast Cancer and its Various Treatments. A. The most common form of invasive breast cancer Ductal Carcinoma In Situ is characterized by the neoplastic proliferation of epithelial cells within the mammary gland lobules and ducts. These cancer cells can quickly spread throughout the ductal system, threatening the health of the nipple tissue. **B**. Breast Conserving Surgery or a Nipple-Sparing Mastectomy can be performed if the breast cancer tumor is greater than 5 cm away from the nipple-areola; however, if the cancer cells have metastasized into this region, the patient must undergo a **C**. Modified Radical Mastectomy procedure. **D**. The most common surgical technique to resect breast cancer tissue in invasive BC cases is shown above, where overlying skin, axillary lymph nodes, nipple-areola, and all mammary gland tissue is resected from the chest and a scar is left proceeding the surgery……...…….....3

Figure 1.2 Schematic Representation of Breast Reconstruction. Silicone implants can be implanted directly above the pectoral muscles of the chest, after the skin has been previously expanded via tissue expanders. The prominence of the central scar is magnified, and many patients undergo nipple reconstruction to lessen this effect……...……...…….....6

Figure 3.1 Description of Printed Inks and Hybrid Scaffold. **A**. Four-arm PEG monomers functionalized with norbornene and thiol end groups react when photoinitiator LAP is present within the solution, as alginate ionically crosslinks with itself with the presence of calcium ions; GelMA monomers mixed with cells and Irgacure 2959 results in a crosslinked cell-encapsulated bioink strand. **B**. Visual representation of alternating PEG and GelMA inks in a 1-1 pattern to create a hybrid scaffold. Complex architectures can be creating using this printing technique, such as **C**. human nose, **D**. ear, and **E**. thyroid cartilage (commonly known as the Adam's Apple). All scale bars represent 5 mm ……..……..…….....39

Figure 3.2: Swelling Characteristics A. Description of ink formulations with varying PEG molecular weight monomers where either i) a pure PEG crosslinked network, ii) added alginate for thickening purposes, and iii) a double network consisting of covalently crosslinked PEG and physically crosslinked alginate was formed. Brightfield images revealed that the interpenetrating networks resulted in the least visual swelling (red box). **B** diameter percent increase, **C** thickness percent increase, and **D** mass percent increase **E** mass swelling ratio were recorded. Discs (synthesized with molecular PEG weight 5K, 10K, or 20K Da) processed under various conditions (Pure PEG and PEG + Alginate contained no calcium soak, PEG + Crosslinked Alginate with calcium soak). n=6 and mean ± standard deviation is depicted. Data was analyzed using single factor analysis of variance (ANOVA) followed by Tukey's Multiple Comparison Test assuming normal data distribution with a confidence of 95% ($p<0.05$)……...…..……..42

Figure 3.3: Mechanical Testing of Various Print Patterns. A. Visual description of the various print patterns used to fabricate hybrid scaffolds. Uniaxial compression testing was performed on hybrid disc scaffolds both before and after experiencing GelMA digestion via collagenase IV. Mechanical properties, such as **B** compressive modulus, **C** fracture strength, and **D** toughness were characterized to ensure hybrid scaffolds exhibited similar properties to soft tissue. n=5 and mean ± standard deviation is depicted. Data was analyzed using single factor analysis of variance (ANOVA) followed by Tukey's Multiple Comparison Test assuming normal data distribution with a confidence of 95% ($p<0.05$)……...45

Figure 3.4: Complex Scaffold Shape Retention. **A** Noses were printed in various patterns of double network ink and GelMA and further subjected to collagenase IV digestion (Print patterns PEG:GelMA of 1:0, 2:1, 1:1, 1:2, and 1:3). **B** Scaffold dimensions were recorded and compared to its original fabricated form, specifically **C** width, length, and peak height. **D** Magnitude of curvature was also calculated and recorded for each hybrid pattern. n=4 and mean ± standard deviation is depicted. Data was analyzed using single factor analysis of variance (ANOVA) followed by Tukey's Multiple Comparison Test assuming normal data distribution with a confidence of 95% ($p<0.05$)……47

Figure 3.5: Color Maps Displaying Point Cloud Comparisons. A. Hybrid nose prints were 3D scanned with a Hexagon Romer Absolute Arm both before and after GelMA digestion, such that finite element meshes could be produced and compared. Color maps display deviations of the digested scaffold to its original form, where red/orange designate positive deviations (swelling) and green/blue designate negative deviations (shrinkage). Histograms displayed on the right graphically show the percentage of mesh points that deviated from their initial positions. Scale bar displays 8 mm……46

Figure 4.1: Components of the Hybrid Nipple-Areola Implant. Two bioinks (GelMA and MC-PEG) are co-printed in various patterns to create a hybrid regenerative scaffold. The GelMA bioink is composed of gelatin methacrylate polymers that can be crosslinked via UV light exposure when photoinitiator LAP is present. Fibroblasts can be encapsulated within the GelMA bioink and serve as a biodegradable region for host dermal integration. The MC-PEG synthetic ink is a double polymer network composed of methylcellulose autonomously interacting with its hydrophobic groups and poly(ethylene) glycol covalently crosslinked upon UV exposure……..59

Figure 4.2: *In Vitro* Implant Functionality. Hybrid nipple-areola scaffolds were 3D printed using the Envisiontec Bioplotter. **A**. CAD designs of each hybrid print, displaying the deposition of GelMA (pink) and PEG (purple) bioinks. **B**. Representative images of each hybrid print, both before and after collagenase digestion, scale bar 10 mm. **C**. Cell viability visualized via Live/Dead (Calcein AM green, live cells; Ethidium Homodimer red, dead cells). **D**. Uniaxial compression testing was performed on hybrid scaffolds both before and after experiencing collagenase digestion with respective compressive modulus recorded (n=3, $p<0.001$). **E**. Fluorescent images (n'=5, over n=3 biological

samples) were taken using a fluorescent microscope (Nikon) and processed using a configured MATLAB code. Cell viability was determined from the ratio of the number of live cells to the total number of cells. Data was analyzed using single factor analysis of variance (ANOVA) followed by Tukey's Multiple Comparison Test assuming normal data distribution with a confidence of 99.9% ($p<0.001$)……...……...……67

Figure 4.3: Nipple Projection Shape Retention while Subjected to Fibroblast Contraction. **A**. Projection flattening is a common occurrence in clinical nipple reconstruction while skin flap suturing techniques are used. **B**. Hybrid scaffolds with nipple geometry were printed with a high concentration of primary human dermal fibroblasts (10 million cells/mL) and cultured for 3 weeks *in vitro* under submerged conditions. The scaffolds were then 3D scanned, and their respective point clouds were compared. Color maps (center) display deviations of the contracted scaffold to its original form. Histograms (left) graphically display the percentage of points that deviated from their initial positions. Scale bar displays 3mm……...……..……66

Figure 4.4 : Quantitative Comparisons Between Hybrid Scaffold Type. **A**. Scaffold dimensions were recorded and compared to its original fabricated form, specifically **B** projection height, **C** projection diameter, and **D** projection curvature. Percent differences display a gradual decrease in scaffold shape, as the scaffolds experienced contraction over the 3-week *in vitro* culture. n=3 and mean ± propagated error depicted. Data was analyzed using single factor analysis of variance (ANOVA) followed by Tukey's Multiple Comparison Test assuming normal data distribution with a confidence of 95% ($p<0.05$)……...……..……71

Figure 5.1 Animal Surgery and Method for Capturing Images. **A**. Three hybrid scaffolds were subcutaneously implanted in the dorsal lumbar region of each rat. Two incisions were made, the first was the initial 20 mm dorsal midline incision over the thoracolumbar area, and the second was through the superficial cervical fascia (a thin layer of subcutaneous connective tissue). This allowed the implant to be stabilized, as tacking sutures resisted significant movement of the implant. **B**. Six images were taken for each central section in every resected implant. We defined the location of each image by the length of the scaffold's areola to normalize this process and ensure that each implant interaction was holistically represented. **C**. Representative images taken before implantation and **D**. after resection, where all samples appear to have maintained a nipple projection with minimal fibrotic capsule development. Scale bars represent 3 mm.…**…...……..……86**

Figure 5.2 Cellular Characteristics. **A**. Representative H&E 2X images pertaining to each scaffold type display a prominent nipple projection. **B**. Semiquantitative scoring evaluations for inflammatory infiltrate (pertaining to lymphocytes, plasma cells, and polymorphonuclear granulocytes) were evaluated by five blind scorers. On the left, colored dots (red, yellow, green, blue, and purple) represent the average score results in every scaffold type evaluation. On the right, a violin curve (type: kernel density estimation) portrays the probability density function of the averaged scores and represents the peak population

incidence of each interface (SC refers to the implant-subcutaneous interface, while FA refers to the fascia-implant interface). Results show a lower inflammation of immune cells in FA than in SC interfaces, with minimal-moderate infiltrate present **C**. Phagocytosis refers to the presence of macrophages, and the results depicted here show a dominating macrophage presence over other inflammatory infiltrate. **D**. Representative H&E 20X images that portrayed the cellular characteristics in and around the scaffolds. Scale bars represent 100 μm……..……..……90

Figure 5.3: Tissue Characteristics 1, Degradation of Implant and Neovascularization of Surrounding Tissue. **A**. Degradation of the biodegradable GelMA is expected in patterns containing the highest amount of this biomaterial (i.e. 1:3 and GelMA 0:1 control), and the average score results reflect this prediction. A striking contrast exists between FA and SC interfaces, which may be due to the increased shear stress induced by the contraction of underlying fascial muscles. **B**. Neovascularization is present in all scaffold types tested, signifying that granulation tissue is beginning to form. **C**. Blood vessels were counted in each 20X (n'=6 with n=4 biological samples) image and recorded to validate our previous blind score results. These quantitative image results display mean ± standard deviation and were analyzed using a two-group Paired Comparison plot followed by Tukey's Multiple Comparison Test assuming normal data distribution with a confidence of 95% (p<0.05). **D**. Representative H&E 20X images that display evidence of neovascularization in every scaffold type, where a red arrow points to the location of blood vessels and/or capillaries present at the tissue interface. Scale bars represent 100 μm……...……...…….93

Figure 5.4: Tissue Characteristics 2, Presence of Fatty Infiltrate. A. The subcutaneous interface experiences a proliferation of adipose tissue, which can be visualized by the high peaks of the gray violin curves. Large adipose vacuoles can be visualized in representative H&E images depicted in **B** (images taken at the implant-subcutaneous interface) and **C** (images taken at the fascia-implant interface). Scale bars represent 100 μm.……..**…….**95

Figure 5.5: Tissue Characteristics 3, Capsule Characterization. A. With all foreign objects introduced to the body, a fibrotic capsule forms at the boundary of the implant and is composed of giant nucleated macrophage cells and surrounding fibroblasts. Scoring results show that the capsule exists in a mild-moderate thickness. This was further quantified in **B**, where each image was evaluated at 3 separate points (n'=6, n=3). These quantitative image results display mean ± standard deviation and were analyzed using a two-group Paired Comparison plot followed by Tukey's Multiple Comparison Test assuming normal data distribution with a confidence of 95% (p<0.05). **C**. Representative Masson Trichrome images for capsule quantitative assessment can be seen on the next page. Scale bars represent 100 μm..……..98

Chapter 1: Introduction to Nipple Reconstruction

1.1 Breast Cancer and its Threat on Nipple Tissue Health

With the latest estimate of 276,480[1] new cases of invasive breast cancer occurring each year in the US, many female patients will face this malignant disease even with early diagnosis by annual mammographic screening. Breast cancer first begins at a single local site, most commonly in the cell lining of the lactiferous ducts (connection of lobules to the nipple, 80% of breast cancer cases), but can quickly break through the walls of the mammary glands or ducts and spread into the surrounding breast tissue (**Figure 1.1**). These abnormal cells can then infiltrate into the axillary lymph nodes and further to distant organs including the liver, lungs, pancreas, spleen, kidney, skin, heart, thyroid, ovary, bones, and brain[2]. Once the cancer begins to metastasize, most patients must undergo surgical treatment (commonly modified radical mastectomy, breast conserving surgery, or nipple-sparing mastectomy) on top of adjuvant therapies (cytotoxic chemotherapy, hormonal therapy, radiation therapy, targeted therapy, and immunotherapy) to resect the affected tissue and eradicate the remaining breast tumor cells that have spread to distant sites by the time of diagnosis[3,4]. The entire treatment process has a wide range of acute and long-term side effects that substantially affect the patient's quality of life[5,6]. Some of these side effects include peripheral neuropathy, dental issues, musculoskeletal symptoms, heart problems, menopausal symptoms, lymphedema, memory loss and cognitive function, infertility, and possible new cancers[7–9]. Even

with local and systemic treatment, approximately 40% of patients relapse and can ultimately die from metastatic breast cancer[2].

A significant number of patients (58%)[10] choose to have their breast tissue removed via mastectomy to avoid the negative side effects of adjuvant therapy and decrease the likeliness of cancer recurrence. There are several types of mastectomy surgical treatments, including simple mastectomy (SM, removal of entire breast and overlying skin), modified radical mastectomy (MRM, combines SM with removal of axillary lymph nodes), radical mastectomy (RM, combines MRM with removal of chest muscles), and skin-sparing mastectomy (SSM, involves removal of breast tissue, nipple, and areola, but most of the skin over the breast is saved and used only when breast reconstruction is performed immediately after the surgery)[11]. The most common mastectomy performed is the MRM, as SM and SSM are reserved for patients with small tumors that are not close to the surface of the skin and RM is an extensive surgery reserved for patients with tumors growing into the pectoral muscles. Alternatively, breast-conserving surgery (BCS, commonly known as a lumpectomy), where only the cancerous tissue is removed from the chest, has been developed to reduce the psychological distress of the patient and avoid postmastectomy syndrome and has been increasingly popular in the past two decades for low-risk procedures (i.e. cases where cancer has been locally contained and >5 cm from the nipple-areola complex). However, it is generally not an option in patients with a high tumor-to-breast ratio, those with multicentric cancers, or those with inflammatory or locally advanced cancers[12].

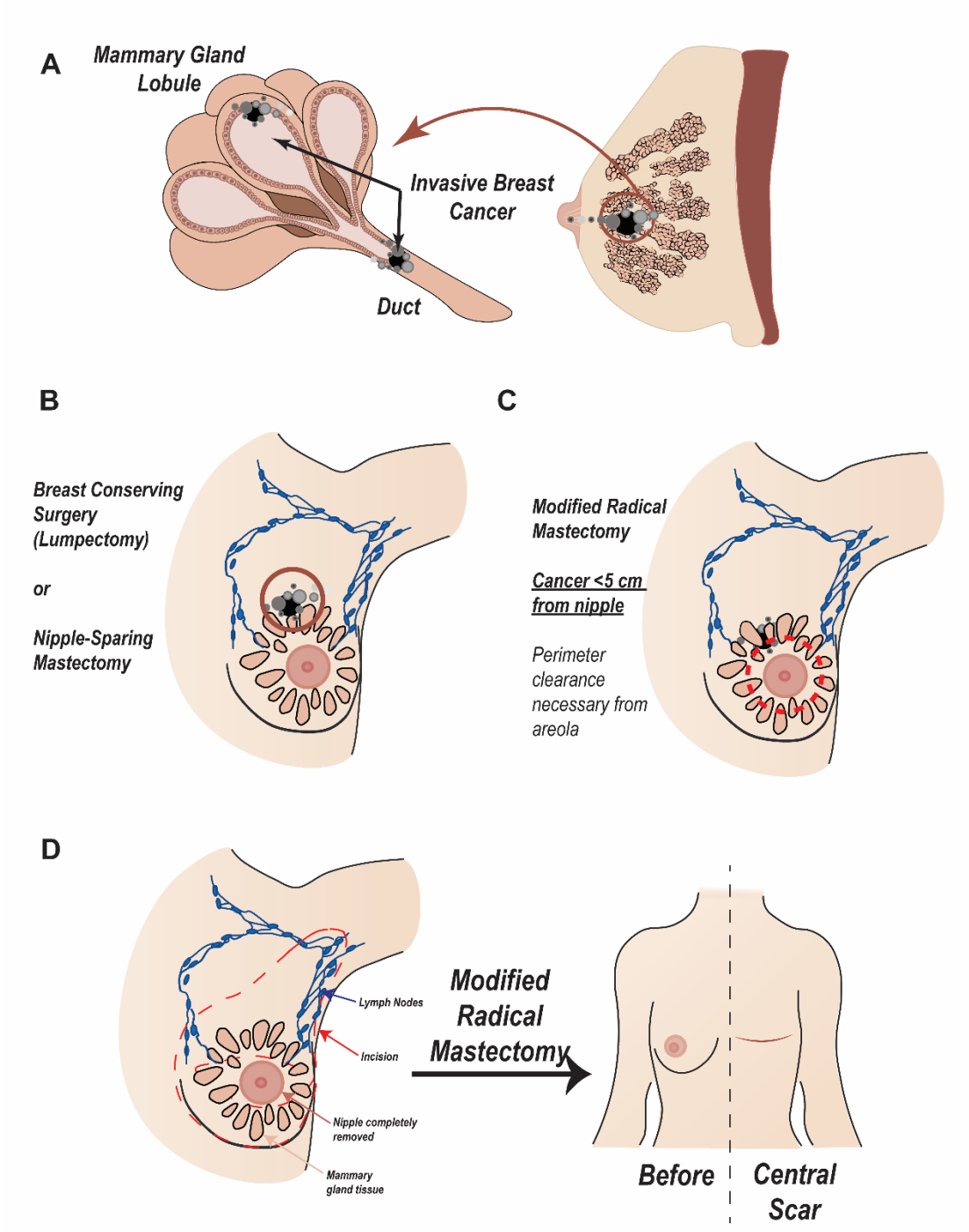

Figure 1.1: Schematic Representation of Breast Cancer and its Various Treatments. A. The most common form of invasive breast cancer Ductal Carcinoma In Situ is characterized by the neoplastic proliferation of epithelial cells within the mammary gland lobules and ducts. These cancer cells can quickly spread throughout the ductal system, threatening the health of the nipple tissue. **B**. Breast Conserving Surgery or a Nipple-Sparing Mastectomy can be performed if the breast cancer tumor

is greater than 5 cm away from the nipple-areola; however, if the cancer cells have metastasized into this region, the patient must undergo a **C**. modified radical mastectomy procedure. **D**. The most common surgical technique to resect breast cancer tissue in invasive BC cases is shown above, where overlying skin, axillary lymph nodes, nipple-areola, and all mammary gland tissue is resected from the chest and a scar is left proceeding the surgery.

The nipple-sparing mastectomy (NSM) is the third most common surgical technique that, similar to BCS, has been developed to preserve the entire nipple-areola complex and the breast skin envelope at the time of the mastectomy. Again, this technique is reserved for early breast cancer cases that are deemed oncologically safe for the patient. Currently there is no available standard protocol for NSM procedures[13]. Because of this, the surgeon is often confronted with a conflict at the time of the procedure; a better cosmetic outcome results if more subcutaneous fat is left after the resection of the breast tissue, however, all of the breasts underlying tissues must be completely removed to avoid the risk of disease recurrence[14]. It remains difficult to identify the correct layer between the subcutaneous fat and glandular breast tissue, and thus there is a higher probability that residual tissue left after the resection may still contain the disease. Some surgeons may also limit NSM procedures in patients with a low amount of subcutaneous fat because they are prone to experience noticeable wrinkling, capsular contracture, and/or skin necrosis due to insufficient vascularization[15].

In most breast cancer cases, the cancer has spread through the ductal tract of the mammary glands and impacts the health of the nipple tissue, resulting in the inability to undergo nipple-sparing mastectomy[16]. Ductal carcinoma in situ (DCIS) is the most

common form of preinvasive breast cancer and is characterized by the neoplastic proliferation of epithelial cells limited to the lactiferous ducts[12]. Many surgeons believe that it is essential to remove the nipple-areola complex when a mastectomy is performed, as the breast cancer nipple-involvement can vary from 25-50% in published DCIS cases[17,18].

Systemic therapies, including chemotherapy, targeted therapy, and hormonal therapy, are often combined with some type of surgery but are not effective in curing the disease alone. Though the risks of complications are nearly twice as high for women who undergo mastectomy than those in BCS procedures, many BCS-eligible women continue to have the invasive radical modified mastectomy (~22,000 cases/year) due to reluctance to undergo radiation therapy after BCS, desire for uniform aesthetic outcomes, and fear of cancer recurrence[19]. Furthermore, women who are diagnosed with breast cancer in one breast are likely to choose to have the unaffected breast removed as well (contralateral prophylactic mastectomy)[20,21].

1.2 Psychological Effects of Mastectomy

Breast cancer survivors are a unique group of patients that face many challenges, some of which include side-effects of ongoing hormone therapy (joint pain)[22], weight gain related to adjuvant therapy[23], persistent fatigue[24], early menopause[25], and psychological challenges that accompany alterations in body image[26]. Many reports indicate that >70% of patients experience pain and depression posttreatment of the disease, with sleep disturbances listed as another common symptom[27,28]. Trauma experienced during initial treatments of chemotherapy and its

side effects, including radiation fatigue, nausea, hair loss, changes in taste, headache, and anxiety, can be recalled with a mere glance at the patients' scars[5,29]. Mastectomies can be life-saving surgeries, but for better or for worse, breasts are so deeply tied to the identity and self-esteem that for many female patients, losing one or both of their breasts difficult to mentally process.

There are many roads to emotional recovery, such as pharmaceutical treatments for depression and anxiety, psychiatric therapy, and even restorative efforts, which is why many doctors emphasize how important it is for women to prioritize their mental health at every stage of breast cancer treatment. Supportive care programs, psychospiritual integrative therapy, and psychosocial support programs have been shown to result in reduced frequency, duration, and intensity of treatment-related symptoms[30,31]. Many patients have found breast reconstruction increases their sense in quality of life, and a good majority (63%[32]) of all patients enduring a mastectomy in the US undergo these breast reconstruction procedures. Reconstruction of the breast mound using silicone implants has made it possible to rebuild a mirage of the natural organ lost from surgery, which helps the patient psychologically heal from significant tissue mass loss (**Figure 1.2**). Plastic surgeons have found, however, that the restoration of the critical visual landmark -the nipple-areola complex- is influential in the emotional recovery of their patients[33]. Without the visual cue that the nipple-areola complex provides, the reconstruction is merely a mound whose most notable feature is the central scar left from the mastectomy.

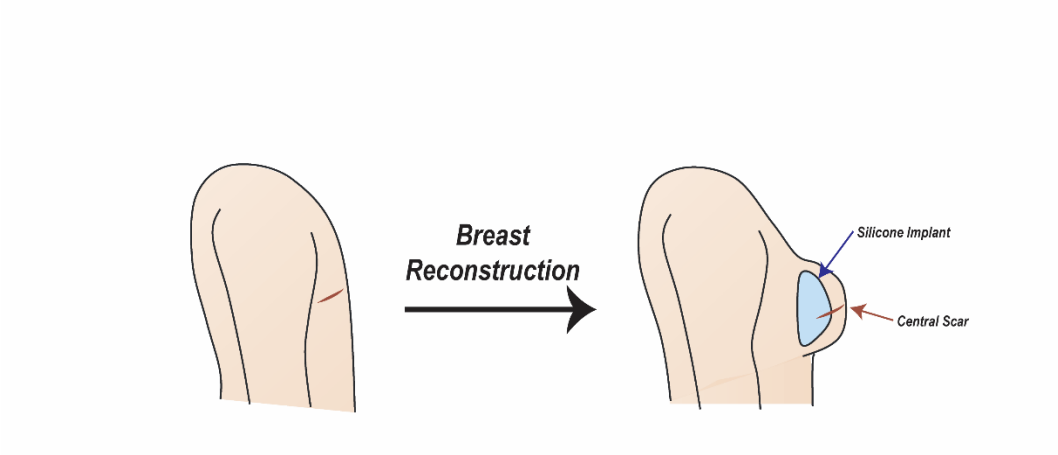

Figure 1.2: Schematic Representation of Breast Reconstruction. Silicone implants can be placed directly above the pectoral chest wall, after the skin has been previously expanded via tissue expanders. The prominence of the central scar is magnified, and many patients undergo nipple reconstruction to lessen this effect.

1.3 Skin Flap Suturing and its Common Setbacks

To ease the physical, psychological, and social challenges breast cancer survivors face, nipple reconstruction using Skin Flap Suturing (SFS) has become a regular post-operative procedure following patient healing of the initial silicone implantation (typically 3-5 months, once swelling and inflammation has subsided)[34] that aims to rebuild the appearance of the new breast tissue. The mammary glands, majority of breast tissue responsible for producing milk, and the lactiferous ducts, tubules responsible for delivering the milk to the surface of the skin, have been removed during the MRM procedure rendering the remaining breast tissue non-functional. Breast reconstruction allows the patient to rebuild the look of this tissue with the implantation of silicone implants within the chest wall. Due to the loss of natural breast tissue function, nipple reconstruction does not require the constructed

nipple to act as a vessel to transport milk and properly function. Thus, skin located at the highest point of the reconstructed breast mound is incised to small skin flaps that are sutured together to build an elevated skin tab. Additionally, intradermal tattooing is effective for creating areolar hyperpigmentation, while darker pigmented skin harvested from the patient's inner thigh or groin can also be used as grafts to produce the characteristic coloration of the areola around the projection[35].

The outcome of local skin-tissue flaps is an inevitable loss of projection with contracture due to wound healing effects. The sutured knot initially experiences local hemostasis and inflammation from leaky damaged blood vessels, triggering an influx of activated platelets and white blood cells to the injured site. Immune cells have been shown to secrete collagenase, among other proteolytic enzymes, which immediately begin to degrade the forced collagen network of the knot[36]. Granule tissue formation (fibroblast growth and deposition of new extracellular matrix by the excrement of collagen I and fibronectin) and epithelialization (proliferation and crawling of epithelial cells atop the wound bed providing a cover for the new tissue) are necessary for the projection to effectively heal and maintain its proper shape; however, wound contraction and scar formation can affect these processes[37]. Recruited myofibroblasts attempt to decrease the size of the wound by gripping the wound edges and contracting using cellular mechanisms similar to those of smooth muscle cells[36]. The skin lesion is usually healed within 3 weeks; however, the end product is not aesthetically ideal. A flattened disfigured skin tab results, where the collagen matrix has been poorly reconstituted and further develops into connective

scar tissue. Studies comparing several SFS techniques demonstrate a disappointing 70% loss of projection within 12 months due to complications in scar contracture, retraction forces from surrounding skin, and inadequate vasculature[38–40]. Multiple incision techniques have been investigated, such as C-V flaps, Skate flaps, Star flap, and Purse-String Suture (**Table 1.1**), but regardless of the skin flap incision pattern used the result remains a flattened skin tab scar that these women repeatedly fix throughout life[41–46]. The act of repetitive reconstructive surgery is yet another detrimental psychological challenge these women face, adding even more difficulty to overcoming their disease. In order to improve clinical outcomes from nipple reconstruction, better technologies to control nipple flattening and a more reliable method for the construction of a normal-looking nipple need to be developed.

SFS Documented Procedures			
Author	**Year**	**Surgical Technique**	**Notes**
Berson MI[47]	1946	Berson's Technique	three identical triangular sections excised; margins of triangles are sutured together
De Cholnoky T[48]	1966	Everted navel	
DiPirro ME[49]	1970	DiPirro Technique	Modification of Berson's; four triangular wedges
Muruci A[50]	1982	Double dermal-fat flap	
Barton FE Jr[51]	1982	Maltese-cross dermal-epidermal flap technique	
Little JW III[52]	1983	Quadrapod flap	
Silversmith[53]	1983	Silversmith Technique	modification of quadrapod flap
Hartrampf CR Jr[54]	1984	Omega flap	
Kon M[55]	1984	Three Flaps	
Chang WH[56]	1984	T Flap	
Cohen IK[57]	1986	Pinwheel Flap	
Little JW[58]	1988	Skate Flap	
Cronin ED[43]	1988	S Flap	
Kroll SS[59]	1989	Dual Opposing-tab-flap	
Anton LE[60]	1991	Star Flaps	
Jones G[61]	1994	C-V Flap	
Teimourian B[62]	1994	Propeller Flap	
Eng J[63]	1996	Bell Flap	
Thomas SV[64]	1996	Thomas Technique	Cutaneous-flap with a shape of rectangular plus circle
Rubino C[65]	2003	Arrow Flap	Modifications to Thomas SV technique
Gamboa-Bobadilla[66]	2005	Top Hat Technique	
Germano D[67]	2006	Fleur-de-lis Flap Technique	
Hammond DC[68]	2007	Skate Flap Purse-string Design	
Brackley PT[61]	2009	Modified C-V Flap	
Zhong T[58]	2009	Modified Skate Flap	
Farace F[69]	2010	Modified Arrow Flap	
Van Laeken N[70]	2011	Two-Step Purse-string Suture Technique	
Jamnadas-Khoda B[71]	2011	Cigar Roll Flap	
Karabagli Y[72]	2012	E Flap	
Elizabeth Clark S[73]	2014	CC-V Flap	augmentation of C-V flap
Butz DR[74]	2015	C-Y Trilobed Flap	

Table 1.1: Documented SFS procedures by plastic surgeons

1.4 Engineering Nipple Tissue

The technical objective of nipple reconstruction is to create the appearance of a nipple-areola complex that maintains projection and is symmetrical with the contralateral breast in terms of pigmentation and size. Symbolically, it represents the final chapter of the breast reconstruction process and lends a meaningful sense of closure for the patient. Previous reports have documented that nipple reconstruction enhances the self-esteem in patients and decreases the feeling of distress due to the mastectomy procedure itself[75–77]. Some have even reported that women are more likely to undergo a mastectomy if the nipple can be reconstructed[78]. Overall, this process undeniably provides psychological benefit to the patient, and therefore is an essential component in the breast reconstruction process.

An ideal reconstruction of the nipple-areola complex requires symmetry in position, size, shape, texture, pigmentation, and permanent projection. Even within the same patient, however, the nipple-areola anatomy can be remarkably variable. The nipple itself may project as much as 1cm, with a diameter of approximately 4-10 mm, and the surrounding areola averages 3.0-4.5 cm in diameter[34,79]. Its projection results from underlying mammary ducts that converge to one central point, producing a dynamic semi-rigid structure that can be stimulated (either by direct contact or neural stimuli) to gradually change in height. Since a wide variability exists in dimension, color, and texture, the nipple-areola complex is generally regarded as the prominent elevated structure centered within a pigmented area located on the apex of the breast mound.

Several attempts have been made to address this topic using a tissue engineered approach. Sprinkled throughout the past 75 years in literature, research groups have implanted a variety of materials to create a nipple projection, including autologous materials (cartilage[80–83], fat[84,84,85], and contralateral nipple[34,86–88]), alloplastic materials (hyaluronic acid[89,90], calcium hydroxyapatite[91,92], and artificial bone substance[85]), decellularized matrices (rolled dermal grafts[38,93,94], cadaveric nipple tissue[95]), and synthetic materials (internal[96,97] or external silicone prosthetics[98–101]). Although many claim some methods are superior to others, undesirable aspects persist with each method.

1.4.1 Autologous Materials

Initiated by Adams in 1944[87] and further described by Millard in 1972[88], the nipple-sharing method (the implantation of autologous contralateral nipple grafts) has remained as one of the most popular methods documented in nipple reconstruction history. The results recorded excellent pigment and texture match and high patient satisfaction. This procedure does have its limitations, however, as it is only applied to patients with 5-6mm excess projection (diagnosed as hypertrophic). Some patients may also be hesitant to exchange one normal nipple for two inferior ones, and there are possible complications that accompany the procedure- including donor site morbidity, pain, scarring, infection, and loss of sensation in both the reconstructed and contralateral nipples[86,102].

Autologous cartilage tissue implantation for nipple reconstruction was first introduced by Brent and Bostwick in 1977[103]. This first attempt resected cartilage from the patient's rib at the costochondral-sternocostal joint. Several groups followed suit[80–83], as this implantation only averaged a 26.1% projection loss after 45 months. However, complications did arise, such as ischemia, infection, and further migration of the cartilage tissue. Increased operative time and donor site morbidity were the biggest downfalls of this procedure, and many surgeons feel that the increased invasiveness of obtaining a graft outweighs the marginal cosmetic benefit.

The autologous material that provides a nipple projection with the most natural tactile properties is adipose tissue. Donor fat can be harvested from the abdominal region using aspiration cannulas, concentrated into 1cc syringes, and injected into a sutured flap[84]. Unfortunately, this technique does result in loss of projection (up to 60%)[104] due to postoperative fat necrosis and inadequate vascularization. Therefore, repetitive reconstruction is necessary in order for this technique to be effective.

1.4.2 Alloplastic Materials

With advancements in materials engineering, alloplastic materials have become the most promising matrices that can be used to produce a lasting nipple projection. Hyaluronic acid stands out as the most attractive contender, as cases report high patient satisfaction and a projection that can be maintained for 12 months[89,90]. Injections do need to be performed at 2, 4, and 7 months to create the final result, and maintenance injections are required as this matrix is highly

degradable. Calcium hydroxyapatite (Radiesse) is a more robust injectable, however, this filler has been found to interfere with breast cancer screenings as it remains radiopaque in mammograms[91,105]. Thus, although alloplastic material injections have been found to bleed into the surrounding breast tissue and may interfere with oncologic surveillance, they do have a clear advantage when compared to autologous reconstruction due their lack in donor site morbidity.

Ceratite, an implant labeled as artificial bone substance, presented the highest complication rate (18%)[85] in reported alloplastic materials. This implant, composed of 20% tricalcium phosphate and 80% hydroxyapatite, was initially developed for use in craniomaxillofacial reconstruction[106]. Unlike the injectable materials mentioned above, this material was implanted subdermally and resulted in flap necrosis and an extrusion of the artificial bone. Other stiff implants (composed of synthetic polytetrafluoroethylene)[107] have also been shown to extrude from the body, and it's possible that the increased pressure from the nipple flap combined with the rigidity of the materials likely causes this extrusion.

1.4.3 Decellularized Matrices

From burn treatments to breast reconstruction, the use of acellular dermis has become a popular method to restore a variety of tissues. Detergents and chaotropic agents such as Triton X, sodium dodecyl sulfate, and deoxycholate are used to carefully decellularize donor tissue, creating matrices that contain both natural structure and composition of dermal extracellular matrix (ECM) and can be further

implanted for regenerative purposes. AlloDerm, a human-derived acellular dermis, has been cut and folded upon itself to create a nipple projection in previous reports. Although this matrix greatly guided neovascularization throughout the projection, the AlloDerm-augmented nipples displayed a shrinkage of 50-70% and failed to produce a statistically significant improvement in projection when compared to traditional SFS reconstruction[38,93]. In addition, the cost of each AlloDerm nipple implant could range up to $1500, rendering it as the most expensive material that provides no discernible benefit for nipple projection[94].

This past October 2020 marked a critical timepoint in nipple reconstruction history. BioAesthetics, a biotechnology startup, announced that it has significantly surpassed its Series A $2.5 million for its premiere product NACgraft, a decellularized cadaveric nipple tissue implant[108]. The substantial support for the NACgraft is exciting, as it validates the market's need for a regenerative nipple-areola graft. The group has previously shown that the residual DNA content of the NACgraft is well below the threshold that is comparable to commercial acellular products[109,110] such as TissueMend, Restore, GraftJacket, and AlloDerm, and that its intact extracellular components of collagen, elastin, and cell-adhesion molecules aid in the acceptance of the graft in a *Rhesus macaque* study[95]. One can speculate, however, that patient preference for the cadaveric donor tissue may waver when presented with an alternative tissue-engineered implant.

1.4.4 Synthetic Materials

Mimicking current breast reconstructive practice, small gum-drop silicone and polyurethane implants have been subdermally placed in patients to create a nipple projection. Unintuitively, these materials resulted in a myriad of complications. Patient safety was a concern due to the materials accompanying risks of hematoma, toxicity, allergic and immune reactions, and potential carcinogenicity[97]. Silicone rods have also been reported to result in a 100% rate of local flap necrosis and rod extrusion[96]. Given these outcomes, silicone implants are not regularly used in nipple reconstruction.

In addition to implants, silicone has also been used to create external nipple prosthetics. In this case, custom prosthetics offer patients a nonsurgical option for nipple reconstruction[98,99]. A prosthetist can create a life-like nipple-areola complex by creating a mold from a previous impression of the contralateral nipple. This silicone nipple-areola can then be attached to the breast mound with silicone tape or other adhesives. Patients greatly enjoy this option because of the customization aspect of this process, but these prosthetics can be uncomfortable to wear and do not carry the benefit of an integrated persistent projection with the breast[100,101].

1.5 Conclusion

In all surgical cases, the main complication that plagues nipple reconstruction continues to be projection flattening and poor cosmetic outcomes. Autologous materials are generally accepted by the host but disadvantages the patient with

increased donor site morbidity and operational time. The ease and low complication rate that accompany alloplastic injections render this technique favorable, yet it still requires constant maintenance for the patient. Decellularized dermal matrices are expensive and still result in an undesirable flattened skin tab, while cadaveric tissue may not be a patient's first choice when deciding which materials to use for their breast reconstruction process. A customizable TE approach that incorporates the uniqueness of each patient and presents an opportunity to regenerate part of the breast may help improve patient psychological health and may be the next worthy solution.

1.6 Dissertation Work Overview

A surgical procedure that necessitates repeated intervention due to projection loss is not appropriate for the psychological health needs of breast cancer survivors. The development of a customizable nipple-areola tissue engineered graft capable of retaining its shape and mechanical features once implanted could reduce the need for subsequent surgical interventions, result in a more well integrated, aesthetically pleasing nipple, and most importantly, prioritize and support the emotional health of the patient. Specifically, the aims of this work are as follows:

1) Develop a hybrid printing technique that capitalizes on the strengths of both natural and synthetic bioinks
    a. Design an extrudable synthetic bioink that displays soft tissue mechanical properties with minimal post-print swelling
    b. Define a shape analysis technique to accurately compare printed hybrid samples

2) Design and fabricate a nipple-areola scaffold that mimics the complex structure of the native nipple-areola complex
    a. Evaluate *in vitro* functionality of the scaffold
    b. Characterize the shape retention of the cell-laden nipple projection
3) Demonstrate positive implant integration in a rat subcutaneous model
    a. Characterize the foreign body response and neovascularization of the optimized hybrid nipple-areola scaffolds

Chapter 2: Recent Developments in Soft Tissue Engineering[1]

Soft tissue engineering is a promising TE field whose strategies can be applied to engineering a nipple-areola construct. In the background information presented below, we first investigate the clinical strategies used to treat soft tissue defects and the challenges that accompany them. Next, soft tissue engineering strategies are explored in terms of scaffold fabrication techniques and the materials generally used in each process. Last, we dive into the most attractive technique, additive manufacturing, and explore the advantages and disadvantages of extrusion-based 3D printing.

2.1 Challenges that Accompany Autologous Grafts and Soft Tissue Implants

Similar to nipple reconstructive cases, treatment methods for soft tissue defects in the clinic present a number of challenges and limitations. These defects may occur due to several causes, ranging from simple contour incongruencies due to congenital deformities to large volume tissue loss following deep burns, trauma, or tumor resection. The term 'soft tissue' can refer to both connective tissues (such as tendons, ligaments, skin, adipose, cartilage, and synovial membranes) and non-connective tissues (such as muscles, nerves, and blood vessels)[111]. Because soft tissue defects range in size, shape, and tissue composition, there is no single solution capable of reconstructing replacement tissue with identical volume and mechanical

[1] Adapted from: Van Belleghem SV, Mahadik B, Snodderly K, Fisher JP, "Overview of Tissue Engineering Concepts and Applications", Biomaterials Science, Fourth Edition: Elsevier, 2019

properties. Current clinical techniques fill most soft tissue voids with either natural materials, such as free adipose tissue grafts and autologous dermal fat flaps, or synthetic materials, such as commercially available silicone implants[112,113]. Unfortunately, all these strategies present significant setbacks. Though free adipose tissue can be resected safely with a minimally invasive procedure, the autologous fat transfer experiences significant volume augmentation due to the limited survival of mature adipocytes post liposuction trauma. Contour irregularity, lumpiness, and graft resorption make this grafting technique inefficient and unsuccessful[114]. Dermal flat flap harvest, a technique that completely resects large sections of skin and fat tissue in attempt to retain its vasculature and structure, is a technique limited by the donor site and can lead to site morbidity, pain, scarring, and often experience shrinkage and fibrosis post implantation[115–117]. Silicone implants have the advantage of permanently retaining mechanical properties; however, they do not integrate with the surrounding host tissue and are commonly associated with implant migration, rupture and/or breakdown, and fibrotic encapsulation from the immune system's foreign body response[118,119]. In some cases, the encapsulation causes a significant pain and an undesirable contortion of the implant, and further surgical intervention is needed to restore the area. The contortion of silicone implants used for breast reconstruction have been reported to cause spontaneous leakage of silicone gel, and these synthetic molecules can migrate into vital organs including the brain and spinal cord, the lymphatic stream, liver, and kidneys[120]. According to several authors, this 'bleeding' or silicone diffusion may be associated with systemic complications and symptoms related to various autoimmune diseases[121–123]. Although for different reasons, all of

the strategies mentioned above do not ensure long-term volume restoration and result in low patient satisfaction due to the absence of long-term graft retention and aesthetic restoration, necessitating a more robust strategy to repair soft tissue defects.

2.2 Common Scaffold Fabrication Methods Utilized in Soft Tissue Engineering

Soft tissue engineering has emerged as an alternative for tissue transplantation with the primary goal of providing a clinically relevant substitute. By recapitulating the normal tissue development process, soft tissue scaffolds and their subsequent implantation represent a strategy to restore, maintain, and improve tissue function. The scaffold provides the necessary environment and support for cells to attach, proliferate, and maintain their differentiated function and subsequent regeneration of new tissues. Ideally, a scaffold should have the following characteristics[124]: (1) 3D highly porous structure with an interconnected pore network to facilitate cell/tissue growth and diffusion of nutrients, metabolic waste, and paracrine factors; (2) biodegradable or bioresorbable features with controllable degradation and resorption rates to match cell/tissue growth *in vitro* and *in vivo*; (3) suitable surface chemistry for cell attachment, proliferation, and differentiation; (4) mechanical properties to match those of the tissues at the site of implantation; and (5) easy processability to form a variety of shapes and sizes.

Biomaterials are used to develop scaffolds and provide important biological signals for cells to organize and restore structure and function to damaged tissues. The bioactive matrix provided by these materials present well-defined biochemical (e.g.

growth factors and surface chemistry) and biophysical (e.g. fibrous structure, hydrophilicity, and stiffness) cues to effectively regulate cellular behaviors such as attachment, migration, proliferation, and differentiation [125]. Biomaterials can, at the same time, be used to supply nutrients, drugs, and bioactive factors that direct specific tissue growth. Accordingly, these materials should be non-toxic and ideally possess mechanical and engineering properties suitable for its intended application. The following sections describe some key developments regarding scaffold fabrication and the common materials used in soft tissue engineering.

2.2.1 Conventional Porogen Leaching

The formation of a porous structure is the main goal of scaffold fabrication. Most methods for fabricating porous scaffolds, including particulate leaching, freeze drying, gas infusion, and phase separation, rely on casting the scaffold material within molds and incorporating internal additives to create a heterogeneous distribution of pores. The porous nature of these structures can be developed by introducing solid particulates or gaseous microbubbles as the scaffold material solidifies; once removed, the end result is a delicate, interconnected network of pores sprinkled within the internal regions of the scaffold[126]. Although these techniques are relatively simple for developing a three-dimensional structure, they are limited by uncontrolled pore size and connectivity, poor mechanical strength, and residual solvent/porogens [127]. Hydrocarbon templating, a combinatorial process of polymer mixtures, compression, and vacuum treatment, is a fabrication method with enhanced control over scaffold thickness and pore structure[128]. Its use of organic solvents, however, is

a disadvantage for biological applications of the porous foam as this cytotoxic reagent is difficult to remove completely from the scaffold. Alginate, a polysaccharide derived from the cell wall of brown seaweed, is a widely utilized biomaterial used in this fabrication technique due to its biocompatibility, mild and physical gelation process, chemical and physical cross-linking abilities, non-thrombogenic nature, and the resemblance of its hydrogel matrix texture to that of the native extracellular matrix. In a study using conventional porogen leaching to mimic the heterogeneity of the native adipose tissue, a potential to achieve a foamy structure using this type of approach was demonstrated with alginate, but with concerns on the long-term maintenance of the scaffold geometric properties[129].

2.2.2 Hydrogel Casting

Various synthetic and natural polymers can be dissolved and chemically crosslinked in solution to form three-dimensional hydrogel networks. Poly(ethylene glycol)[130], poly(N-isopropylacrylamide)[131], poly(vinyl alcohol)[132], and poly(acrylates)[133] are synthetic examples of these materials, while gelatin[134], silk fibroin[135,136], fibrin[137–141], and hyaluronic acid[142,143] are those of natural materials. Hydrogels are commonly used in soft tissue engineering as accessible casting methods render physiologically relevant mechanical properties and hydrated gels capable of encapsulating cells or bioactive molecules[144,145]. Photopolymerizable functional groups are needed for the creation of these gels so that the matrix remains intact once the scaffold is submerged during *in vitro* culture. The specific monomer

of the hydrogel material determines its particular crosslinking capabilities; some are crosslinked using visible or ultraviolet light when certain crosslinking agents are present[146], while others may be crosslinked through heat, ionic, or covalent bonding. The mechanical properties, mass transport, and degradation characteristics are defined by both the polymer composition and crosslinking density and can be further fine-tuned to create hydrogels for a vast range of soft tissue applications[147]. Furthermore, hydrogels can be chemically modified to improve the adhesion and proliferation of cells within or directly on gel matrices through the inclusion of adhesion peptides. One major setback of most degradable hydrogel materials is their limited mechanical strength. Degradable hydrogels have a tendency to fracture when subjected to compressive loads due to their brittle and swollen nature, which can result in a structural collapse and ultimate scaffold failure[144]. This soft matrix is unsuitable for most soft tissue defects, as these areas of the body (such as breasts) do experience regular compressive forces.

2.2.3 Synthetic Fiber Electrospinning

Electrospinning synthetic polymers is a popular method used to generate a fibrous scaffold containing fibers ranging from several nanometers to several micrometers in diameter. The woven fiber matrix that results from this fabrication technique greatly mimics the extracellular matrix of collagen fibrils visualized in tendons and ligaments[148], a major tissue composition found in soft tissue engineering. Deposition speed and charge of the synthetic material can dictate the strand diameter (50 - 500 nm) and orientation of the fibers (aligned or random) [149]. These scaffolds

are advantageous due to their high surface-to-volume ratio and interconnected porous architecture, which can help cells easily penetrate to the internal regions of the scaffold. Saturated aliphatic polyesters, such as polylactide(PLA), polyglycolide(PGA), and poly(caprolactone) (PCL), are the most common used biodegradable synthetic polymers for electrospun scaffolds[150–152]. The chemical properties of these polymers allow hydrolytic degradation, where de-esterification occurs as the main chain ester bonds are exposed to water. The rate and extent of degradation depends on the polymer's molecular weight, structure, and composition. For example, PCL and PLA have been previously electrospun into aligned fibrous scaffolds that have been shown to promote neural differentiation of human MSCs and the elongation of the formed neurites when compared to conventional flat casting film culture practice[153154]. The setback of this fabrication technique is that it is difficult to control the distance between fibers, and the resulting scaffold is a dry, stiff matrix that greatly differs from the surrounding natural tissue.

2.2.4 Additive Manufacturing

3D printing is a modern fabrication method where digital data of a three-dimensional structure is converted into a physical object. The ability to scan existing host tissue via computed tomography (CAT) and replicate the exact dimensions of that target greatly appeals to soft tissue reconstruction, where there is a high instance of uniquely size defects resulting from either trauma or the resection of tumors and congenital deformities[155]. In contrast to traditional fabrication methods (involving molds or solvents), 3D printing can create complex structures from the bottom-up in a

layer-by-layer fashion. Generally, a structure is first visualized digitally with the help of computer-aided software (e.g. SolidWorks and CreoParametric) and later sliced into individual layers by the specific printer software providing a specific set of instructions that control printer movements and functionality. Three major approaches for 3D bioprinting soft tissues currently exist: inkjet printing, extrusion printing, and stereolithography. The chosen fabrication method will vary in terms of materials used, the construct design parameters, and the time needed for the creation of the desired part. Below is a brief description of each type printing method, as well as its positives and pitfalls.

Inkjet Printing. Much like how a traditional printer utilizes ink cartridges to deliver droplets to paper to create documents, inkjet bioprinters can deliver biomaterials and/or cells in controlled volumes. These printers have the finest resolution in bioink deposition (50 μm- 1 mm) and the highest printing speeds (15-25 kHz)[156]. Droplets are synthesized through either thermal or mechanical means, a mechanism that enables a high spatial resolution; however, the stresses produced through these means can perturb cells during the printing process. Instant heat exposure and shear stress can also induce cell damage. Since ink for this printer must be fluid so that individual droplets can form, this type of technology has one of the highest selection of materials available. However, the size of the printed object is significantly small, and the cell density of the bioink can be limited[157]. As such, inkjet printing is best for 2D soft tissues with relatively low cell density and complexity.

Stereolithography and Digital Light Projection. Stereolithography (SLA) and Digital light projection (DLP) are two forms of light-based additive manufacturing processes. In the SLA process, an ultraviolet laser located directly below the printing platform is instructed to focus at specific points in space to locally polymerize the biomaterial. A 3D object of any desired shape can be made by creating a specific light path for each 2D slice over the height of the printing volume[158,159]. The DLP process is similar to that of SLA, except the light source is projected as a 2D light mask across the resin bath. The advantage of SLA and DLP includes high accuracy and precision during the printing process. Since the optical point of the laser/projector can be finely controlled, the resulting resolution is significantly high and small geometric parts can be easily fabricated. However, there are several pitfalls with this fabrication technique. Both SLA and DLP printing processes have low material versatility. Photo-curable acrylate resins and epoxies, the original polymers that helped define these methods, continue to be the most common materials for this fabrication process. In addition, only one photopolymerizable material can be used during the printing process, as the print platform is completely submerged into a single polymer vat throughout the print, and un-crosslinked material pose a health hazard to users as it contains radical photoinitiators. Low cell viability is also common when hydrogel polymeric solutions are used as excessive exposure to UV/visible light during a lengthy print time tends to kill the cells seeded within the polymer vat.

Extrusion 3D Printing. Both Fused Filament Fabrication (FFF) and Pneumatic Deposition (PD) are examples of extrusion-based 3D printing. In both FFF and PD,

the printer head extrudes continuous filaments of shear-thinning, thixotropic material (either synthetic filaments or hydrogels containing biomacromolecules or cells) through a nozzle (under step motor driven mechanical forces or pneumatic pressure). Acellular scaffolds and cell-laden hydrogel constructs can be fabricated layer-by-layer as the print head moves in 2 dimensions (x and y) to deposit matrix in one horizontal plane at a time. Some advantages of FFF and PD include high material versatility, multi-material printing, and low cost when compared to other 3D printing methodologies. Examples of inks compatible with this deposition method include hydrolytic synthetic polymers, gelatin, fibrin, alginate, hyaluronic acid mixtures, and silicate nanoplatelet mixtures[160]. The combination of multiple materials via various extruders or printing cartridges allows for facile engineering of chemically and structurally complex tissues. Compared to resin-based methodologies such as SLA and DLP, material is better conserved during this fabrication technique as a polymer vat containing excess material is not necessary. Though extrusion printing is an efficient and low-cost method for fabricating cell encapsulated constructs, the printing resolution is limited by the print head's diameter and by the viscosity of the biomaterial[161]. Shear-thinning biomaterials, in regard to strain rate or temperature-dependent properties, are also limited as this fabrication process requires the material to maintain strand shape. Despite these limitations, this is our fabrication method of choice as previous work indicates that pneumatic driven extrusion 3D printing holds promise for the fabrication of soft tissue engineering constructs. In the following section we will dive deeper into some of the difficulties and considerations required when using 3D printing for soft tissue engineering applications.

2.3 Current Setbacks in Extrusion Printing for Soft Tissue Engineering

Though extrusion-based 3D printing is highly beneficial when fabricating TE scaffolds, there are material concerns when this technology is applied to soft tissue engineering. Bioink, the matrix material used for tissue printing, should provide suitable cues and signals for cellular function and tissue formation. Various naturally-derived extracellular matrix components, such as collagen/gelatin[162,163], alginate[164,165], fibrin[166], and hyaluronic acid[167], have been well investigated in terms of printability; yet, their application to soft tissue regeneration result in failure due these weak materials rapid remodeling *in vivo* and subsequent loss in structural features. Melt extrusion of synthetic polymers such as polycaprolactone[168], poly(D,L)-lactide[169], and copolymers such as poly(L-lactide-co-caprolactone)[170] have also been investigated, but their incorporation to soft tissue regeneration also renders unsuccessful due to similar hydrolytic degradability of these materials and the mismatch in mechanical properties between the stiff printed constructs and the native soft tissue.

In contrast to rigid melt-extruded polymers, synthetic hydrogels are three-dimensional, hydrophilic polymer networks that hold exciting promise in the material choice for soft tissue regeneration. Since the application of 3D printing technology to the bioengineering field has been recent, few papers report the invention of an extrudable synthetic hydrogel ink for pneumatic deposition printing practices. In fact, a mere handful of groups[171–174] have been able to produce extrudable hydrogels containing poly(ethylene) glycol (PEG) components despite this material's popular

use biomedical applications. Previously, PEG has been used in drug delivery[175,176], where the ability to swell can be utilized to deliver molecules of various sizes and chemical structure, biosensing[177], where degradation of copolymerized PEG with enzymatically degradable peptide linkages signals the presence of an antigen, and in tissue engineering[178], where casted hydrogels provide an environment for proliferating cells. In all of these cases, however, the PEG monomers were dissolved in an aqueous solution containing photoinitiators and further casted into a gel when exposed to UV light. These PEG solutions act as Newtonian fluids that are unable to hold strand shape and thus unable to be effectively printed via extrusion.

While PEG hydrogels are inert and exhibit low toxicity, they are not biodegradable[179]. This allows for these gels to retain permanent shape when implanted *in vivo*, but these constructs display poor host integration due to the synthetic material's lack in bioactive moieties. PEG chemistry can easily be tailored to allow for cell infiltration, such as copolymerization techniques of poly(alpha-hydroxy esters), poly(lactic acid), or peptides, yet adding these functionalities renders a similar solubilized fate as the other materials mentioned above. Therefore, the first goal of this work was to establish a hybrid printing technique that capitalizes on the strengths of both natural and synthetic hydrogels to create printed structures containing tunable mechanical, chemical, physical, and biological properties.

Chapter 3: Hybrid 3D Printing of Synthetic and Cell-Laden Bioinks for Shape Retaining Soft Tissue Grafts[2]

3.1 Introduction

Despite recent advances in clinical procedures, the repair of soft tissue remains a reconstructive challenge. Current technologies such as synthetic implants and dermal flap autografting result in inefficient shape retention and unpredictable aesthetic outcomes. Extrusion-based 3D printing offers an efficient tool for accurate fabrication of biomaterial scaffolds with tunable properties[180], and though this fabrication process is highly beneficial, there are similar material concerns when this technology is applied to soft tissue engineering. As discussed in the previous chapter, natural materials undergo rapid remodeling and collapse *in vivo*, while synthetic polymers lack surface ligands for cell attachment and have a mechanical mismatch with the native soft tissue. Although numerous advances in bioink formulations have been made, no ink is singularly capable of mimicking soft tissue with long-term shape and size retention, mechanical stability, and host integration.

To address these shortcomings, we have developed a dynamic hybrid printing approach that capitalizes on the strengths of both nondegradable and biodegradable

[2] Adapted from: Van Belleghem S, Torres Jr L, Santoro M, Mahadik B, Kofinas, P, and Fisher, JP, "Hybrid 3D Printing of Synthetic and Cell-Laden Bioinks for Shape Retaining Soft Tissue Grafts". *Adv Funct Mater*. 2019;30(3):1907145. doi:10.1002/adfm.201907145

hydrogels to create biomimetic constructs with long-term shape and volume retention (**Figure 3.1**). Our design incorporates two inks: a double network (DN) of poly(ethylene) glycol (PEG) covalently linked with naturally derived and physically crosslinked alginate, and a biodegradable cell-laden bioink of gelatin methacrylate (GelMA). The DN ink provides robust physical support necessary to retain long-term graft volume and architecture, while the degradable GelMA bioink provides the biological environment necessary to stimulate tissue regeneration (Figure 3.1A). This printing method results in the precise placement of hydrogel strands that functionally complement each other and enables for the construction of complex geometries (Figure 3.1B). With this 3D bioprinting strategy, complex geometries with robust internal structures can be easily modulated by varying the print ratio of non-degradable to sacrificial strands. Results display various swelling characteristics and mechanical properties can be obtained by tuning the print ratio of DN:GelMA inks. The versatility of this hybrid printing fabrication platform can inspire the design of future multi-material regenerative implants.

With the advancement of tissue engineering, numerous medical products and devices have been developed to address unmet clinical needs. Although preclinical research is important in developing new technologies, their application at the clinical stage must satisfy regulatory oversight at the government level. The application of these regulations is highly regimented and well established for drug therapies; however, it becomes more challenging for multicomponent tissue-engineering products and 3D printed products as the safety and efficacy of each component and process have to be

thoroughly examined[181]. And while many different materials have been assessed for 3D printing, due to the lack of systematic research on the printing procedures and methods for properly evaluating accuracy in part fabrication, the reported fabrication methods are highly specific and case-dependent. Our present study additionally develops an advanced evaluation process incorporating scanned point cloud entities of printed scaffolds and computational comparisons between scaffold surfaces to investigate the correlation between printing parameters and the resulting shape aesthetics of complex bioprinted scaffolds. This new shape analysis technique can expand the available toolbox for assessing scaffold aesthetic properties and serve as a potential systematic procedure for evaluating 3D printed regenerative implants.

3.2 Materials and Methods

Synthesis of 4-Arm PEG Norbornene

4-Arm PEG Norbornene was synthesized as previously reported.[182] Briefly, 5-norbornene 2-carboxylic acid was added at 10X access (basis: PEG hydroxyl groups), with 5X excess dicyclohexylcarbodiimide in dichloromethane, and the solution was stirred for 30 minutes at room temperature. Separately, 4-arm PEG (MW: 5 kDa, 10kDa, and 20kDa, JenKem) was dissolved in dichloromethane, with 5X pyridine and 0.5X 4-(dimethylamino)pyridine (DMAP) and then added to the DCC/norbornene solution. The reaction mixture was stirred overnight at room temperature under argon. The product was precipitated into ice-cold ethyl ether 3 times to rid the solution from the excess toxic reactants. The polymer was then left for 48 h in a vacuum desiccator and later stored at minus 20°C.

Double Network Ink

The double network ink was synthesized by first dissolving 5% (w/v) 4-arm PEG Norbornene and 5% (wv^{-1}) 4-arm PEG Thiol in deionized water. Lithium phenyl-2,4,6-trimethylbenzoylphosphinate (LAP, Sigma Aldrich) with a 0.2% w/v ratio and alginate powder (Sigma) with a w/v ratio varying from 1-5% (derived from brown algae, Sigma) was added and thoroughly mixed. The ideal amount of alginate used for thickening the PEG solution was then tested by systematically extruding the various formulations through the printer cartridge.

Swelling of DN Ink

For each ink formulation (5K, 10K, and 20K), solid discs with a 5 mm diameter and 2 mm thickness were casted using previously printed molds. Disc dimensions, wet/dry weight, and bright field images of each sample were taken before and after a 24 h incubation at 37°C. Percent increase measurements (in mass, thickness, and diameter) were calculated by dividing the difference of swollen vs. unswollen measurements by the original unswollen value. Mass swelling ratio was similarly calculated by dividing the difference of swollen vs. the lyophilized dry weight by the lyophilized dry weight value.

GelMA Bioink

Type A porcine skin gelatin (300 bloom; Sigma-Aldrich) was dissolved at 10% (w/v) into phosphate-buffered saline (PBS; Thermo Fisher Scientific) at 50°C for 20 min. Methacrylic anhydride (MA; Sigma-Aldrich) was added dropwise to the gelatin

solution under vigorous stirring for 1 h (0.6g MA per gram of gelatin). The mixture was diluted with PBS to stop the reaction and centrifuged at 2000g for 2 min. The supernatant was collected and dialyzed (10 kDa molecular weight cutoff; Thermo Fisher Scientific) to remove the excess salts and acids. The dialyzed GelMA was then lyophilized and stored at minus 80°C. For printing, lyophilized GelMA was dissolved at 7% (wv^{-1}) in phosphate buffered solution at 50°C for 20 mins. Irgacure 2959 (0.2% wv^{-1}, BASF) was added at 50°C for 15 min.

Hybrid Scaffold Fabrication

Complex architectures consisting of human nose, ear, and thyroid cartilage (adopted from 3D scans, GrabCAD) were printed in a 1-1 DN-GelMA pattern. All model scaffolds were sliced into layers with a slicing thickness equal to 80% (0.32 mm) of the needle size (0.4mm) before printing. Each printed layer was exposed to UV light (5 mW cm^{-2} intensity) for 5 s, and the final print was placed in a UV box (5 mW cm^{-2}) and exposed further for 6 min. For the remaining assays, 3D cylinder models with 5 mm diameter and 2 mm thickness were designed in SolidWorks (Waltham, MA). For the cytotoxicity assay (1-1 pattern), prints were immediately transferred to 6-well tissue culture plates and submerged in media, with media changes every 2 days for 2 weeks. Cylindrical scaffolds were printed with varying ratios of bioinks (DN:GelMA-1:0, 2:1, 1:1, 1:2, and 1:3) for mechanical testing. Half of the produced scaffolds were exposed to collagenase IV (500 Units mL^{-1}, Worthington Biochemical Corporation) to evaluate the DN's impact on the composite mechanical properties.

Mechanical Testing of Hybrid Scaffolds

Compression testing was performed on a Dynamic Mechanical Analyzer (DMA Q800, TA Instruments) with a strain sweep (0-15%) and load 0.01N at 1Hz frequency. Elastic modulus for each sample was calculated by determining the slope of the linear region of the stress-strain curve (strain region of 3-5%). Fracture strength was recorded (force at which the hydrogel plastically yields) as well as toughness (area under stress-strain curve).

Point Cloud Generation

The ROMER Absolute Arm (Hexagon) was used to generate point clouds containing high geometric detail of the scanned surface. Scaffolds were sprayed with water soluble paint prior to scanning for greater ease in detecting surfaces. The noses were sequentially scanned at multiple angles and the surfaces were selected using the software's editing brush tool. After the total region of interest was created, a volume was generated and exported as a stereolithography (STL) file.

Surface Alignment: STL files of the same sample (both pre and post digestion scans) were imported into the open-source software MeshLab (Visual Computing Lab- ISTI CNR). With this software, the alignment tool and its 'point-based alignment' were used by selecting four possible points along the base face of each model: the first at the center tip of the nose bridge, the second 1mm distance left from the central y axis, the third 1mm distance right from the central y axis, and the fourth at the bottom edge center of the scaffold. This provides an initial rough alignment, and the 'process' tool

was used for fine superimposition. This feature is an ICP (iterated closed point) algorithm capable of enhancing alignment by finding corresponding points on both models to allow for a refined superimposed reposition. Once both models are superimposed, visual comparison of the coincidence in anatomical structures is possible. This final alignment is frozen and exported as a new file, which will keep the achieved alignment intact once opened in the second open-source software CloudCompare.

Cloud Comparison

The two repositioned STL meshes for each pattern were uploaded into the CloudCompare software and point cloud comparison was performed by selecting the pre-digestion mesh as the reference and the postdigestion mesh as the compared object. A color map was generated, which calculated the distance of points in the compared cloud to the nearest point in the reference pre-digestion cloud. For the color maps, a yellow color signified coincident points, while an orange-red spectrum (positive deviation) or green-blue spectrum (negative deviation) indicated the lack of coincidence. A graph also provided the concentration of points analyzed by its distance. CloudCompare's Point Picking function allowed distances to be obtained along the length, width, and peak height of the scaffolds and the Fit Sphere function rendered dependable approximations in the total magnitude in radius of scaffold curvature (left nostril, right nostril, and nose tip). This allowed for distinct quantitative values to be compared among pattern types.

Statistical Analysis. Data was analyzed using single factor analysis of variance (ANOVA) followed by Tukey's Multiple Comparison Test assuming normal data distribution with a confidence of 95% ($p<0.05$).

3.3 Results and Discussion

3.3.1 Double Network Support Structure

To begin, 4-arm thiol-ene PEG hydrogels were chosen due to this system's predictable swelling characteristics, low toxicity, inertness, and resistance to common enzymes.[183] Because this solution exhibits low viscosity at low monomer concentrations, it cannot be loaded into a cartridge and printed alone; this solution is not self-supporting for layer-by-layer fabrication and must either be made very viscous by increasing PEG content or including a thickener. Therefore, alginate was chosen as a thickener for our PEG ink solution since it has been shown to be an effective agent in creating extrudable hydrogels and can provide the opportunity for a second physically crosslinked interpenetrating network when subjected to calcium ions.[184,185] We found that an alginate concentration of 4% (w/v) produced the most ideal filament when mixed with a 10% 4-arm PEG solution, and this composition was further investigated for its swelling, mechanical, cell viability, and shape retention properties.

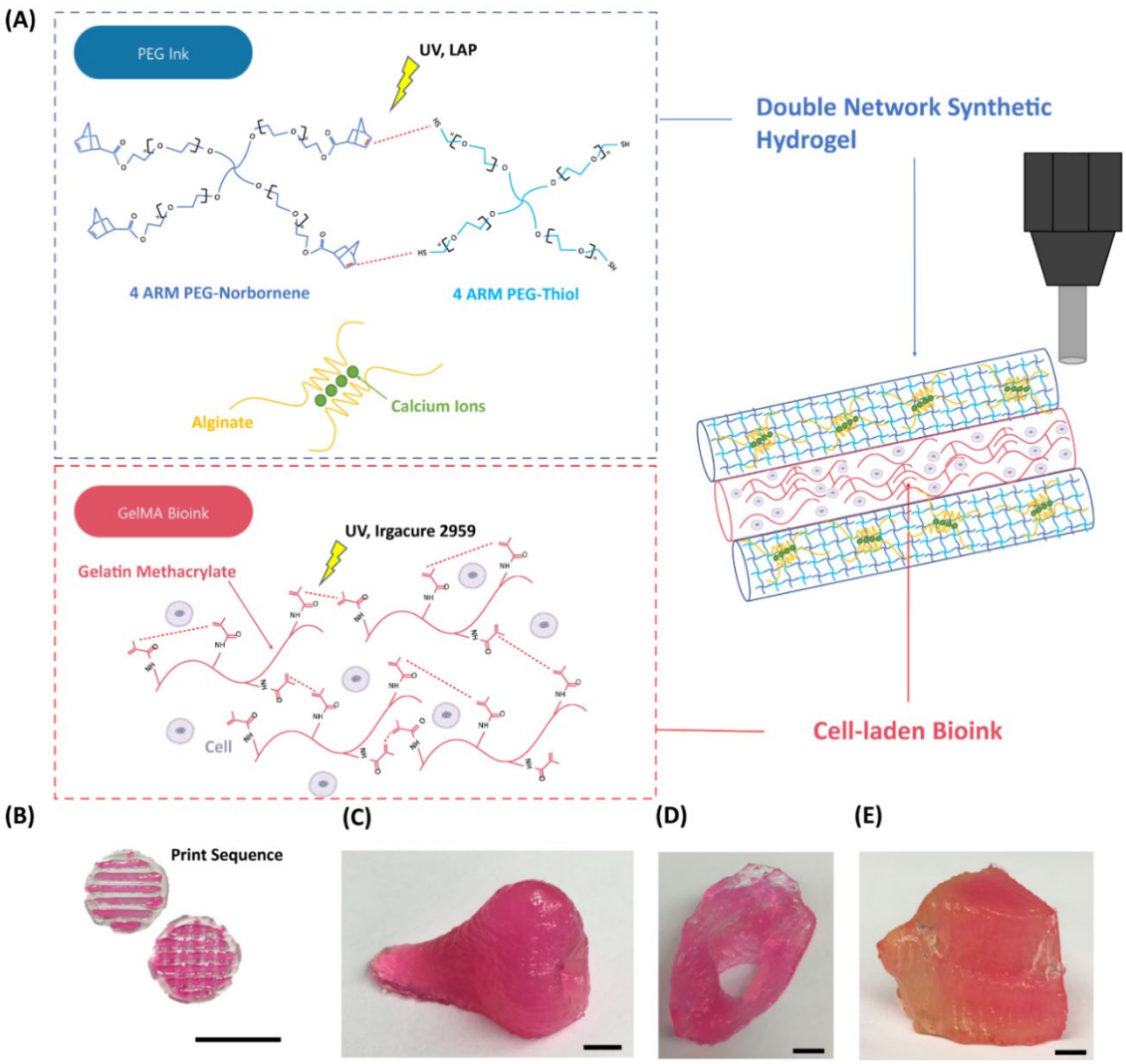

Figure 3.1: Description of printed inks and hybrid scaffold. A) 4-arm PEG monomers functionalized with norbornene and thiol end groups react when photoinitiator LAP is present within the solution, as alginate ionically crosslinks with itself with the presence of calcium ions; GelMA monomers mixed with cells and Irgacure 2959 results in a crosslinked cell-encapsulated bioink strand; B) visual representation of alternating PEG and GelMA inks in 1-1 pattern to create a hybrid scaffold. Complex architectures can be created using this printing technique, such as C) human nose, D) ear, and E) thyroid cartilage (commonly known as Adam's Apple). All scale bars represent 5 mm.

The thiol-ene chemistry provides the added advantages of high crosslinking speed when exposed to UV light, a key factor used in our printing process to intermittently crosslink layers, and its cytocompatability, as the crosslinking of step-growth thiol-norbornene hydrogels is not oxygen-inhibited.[182,186] The thiol-norbornene reaction not only can be initiated several orders of magnitude faster than the classic method of random chain-growth photopolymerization, but also results in a more uniformly crosslinked gel since each monomer with a defined functionality serves as a single crosslinking point.[187] The degree of network heterogeneity is also at a minimum when compared to random chain-growth polymerization, since chain-polymerized gels contain an unfixed number of arms per crosslinking point due to the reaction's random nature of radical propagation and termination.[188] Thus, the thiol-ene chemistry allows for a greater control when designing the swelling and mechanical properties of our ink. To test our material's swelling properties, PEG hydrogels composed of either 5k, 10k, or 20k Da monomers were first casted into discs to characterize the amount of swelling in excess water (**Figure 3.2**). Hydrogels composed of higher molecular weight monomer experience more swelling when mass was held constant as observed in previous studies. For example, previous literature has shown poly(ethylene) glycol hydrogels swell greatly under physiological conditions and often become undesirably weak or brittle after swelling, which limits their applications.[189] Mass swelling ratios are reported in 20–100 range, nearly tripling the hydrogel's originally casted size.[187,190] In our experiments, the smallest molecular weight monomer (5k) pure polymer network originally had the smallest swelling ratio of 14.8 ± 2.4. However, the addition of alginate to any ink formulation

for printing purposes inhibited perfect PEG crosslink formation, which ultimately caused the once favorable 5k swelling ratio to dramatically increase (Figure 3.2E). While the higher molecular weight inks can be printed, significant hydrogel swelling and scaffold disfigurement make these ink formulations suboptimal as an engineered soft tissue replacement. When the alginate thickener was ionically crosslinked with calcium ions (after photopolymerization of the thiol-ene network), the swelling was significantly reduced due to the restriction of the interpenetrating secondary polymeric network. Though double network chemistry is known to create extremely strong hydrogels able to withstand significant stress with minimal distortion, they have only been created with cytotoxic materials previously in literature (polyacrylamide).[191,192] Our choice in alginate as both the ink thickener and the secondary polymeric network is cell-friendly and has been dependably used for 3D printing practices by others.[184,185,193] Overall, alginate physical crosslinking prevented swelling by 32 ± 0.2% in the 5k ink, 53 ± 1% in the 10k ink, and 208 ± 0.1% in the 20k ink (Figure 2D). The 5k ink swelled the least when alginate ionic crosslinking was introduced (mass swelling ratio of 2.4 ± 0.1), with casted disc samples experiencing 5 ± 0.2% increase in diameter, 6 ± 3% in thickness, and 23 ± 1% in mass. The limited swelling of the 5k ink made it an ideal candidate for soft tissue printing, and therefore was further evaluated for cytotoxicity and mechanical properties when co-printed in various patterns with GelMA.

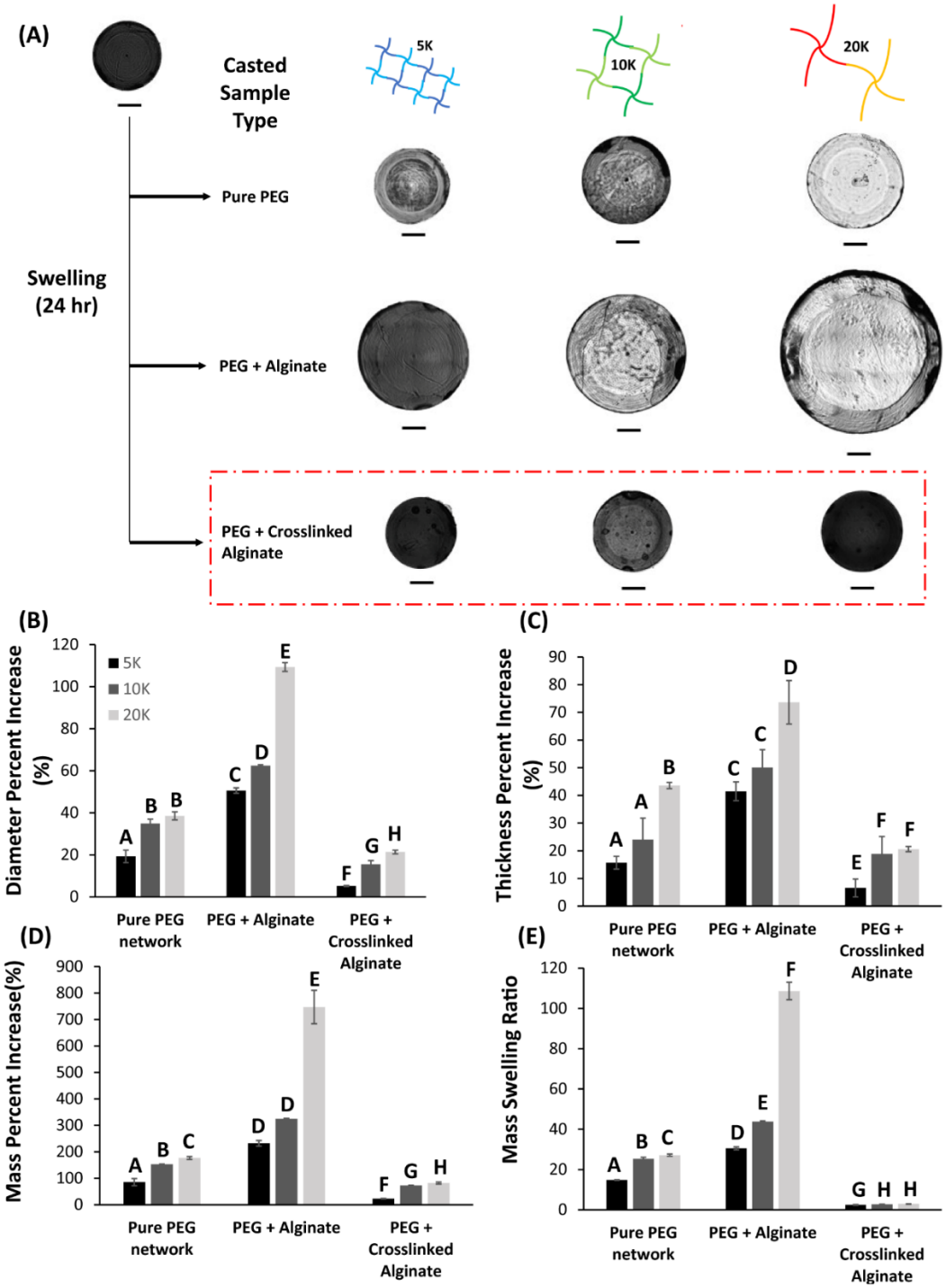

Figure 3.2: Swelling characteristics. A) Description of ink formulations with varying PEG molecular weight monomers where either i) a pure PEG crosslinked network, ii) added alginate for thickening purposes, and iii) a double network consisting of covalently crosslinked PEG and physically crosslinked alginate was formed. Brightfield images revealed that the interpenetrating networks resulted in the least visual swelling (red box). B) diameter percent increase, C) thickness percent increase, and D) mass percent increase E) mass swelling ratio were recorded. Discs

(synthesized with molecular PEG weight 5K, 10K, or 20K Da) processed under various conditions (Pure PEG and PEG + Alginate contained no calcium soak, PEG + Crosslinked Alginate with calcium soak). n=6 and mean ± standard deviation is depicted. Data was analyzed using single factor analysis of variance (ANOVA) followed by Tukey's Multiple Comparison Test assuming normal data distribution with a confidence of 95% ($p<0.05$).

3.3.2 Hybrid Printing

GelMA is chosen for its resemblance to native extracellular matrix, and offers significant advantages such as its ease in printability, UV photopolymerization, and natural cell binding motifs.[194–197] It is widely known as a tunable biomaterial whose composition (weight percentage) and crosslinking degree (UV exposure, photoinitiator concentration, and degree of methacrylation) can be customized to match its rate in degradation to the regenerated tissue it is replacing.[198,199] By strategically co-printing GelMA and the DN inks, our hybrid constructs can be tailored in both stiffness and degradation rate by varying the ratio of each ink in the print. Soft tissue engineering requires matching of mechanical properties to the native tissue, otherwise detrimental effects to the tissue aesthetics can occur. The compressive moduli, toughness, and fracture strength were characterized for various print patterns of DN ink and GelMA bioink (**Figure 3.3**). Patterns of DN-GelMA varied from 1:0 (no tissue regenerative capacity, control) down to 0:1 (completely degradable GelMA, control) (Figure 3.3A). Since the GelMA network can degrade by collagenase, a naturally occurring enzyme in the body, the long-term mechanical properties of the composite scaffold are mainly dictated by the presence of the DN ink's two tightly crosslinked, interpenetrating polymeric networks. Therefore, the aforementioned mechanical properties of the hydrogel were characterized before and

after exposure to collagenase IV (500 Units/mL) overnight. Under uniaxial compression, the composite hydrogels are elastic within 15% strain with moduli scaling a 4-fold variation in stiffness, dependent on DN ink presence- a range congruent with the stiffness values of soft tissue (e.g. skeletal muscle (500kPa) to adipose (10kPa) compressive moduli values, Figure 3.3B).[200–202] Decreasing the double network fraction from the highest 1:0 pattern to the lowest 1:3 DN-GelMA pattern manifested a 74.5% decline in modulus. Printing GelMA alone resulted in a significantly less stiff scaffold (36.8 ± 15.6 kPa), revealing that the coprint benefits from the incorporation of the DN ink for scaffold reinforcement. Scaffold toughness and fracture strength are critical mechanical properties that display the scaffold's ability to maintain shape while under compressive forces during tissue remodeling and implant healing. Both toughness and fracture strength remained high in all patterns before exposure to collagenase IV (1517.8-1836.3 kPa, 26.7-28.9 kPa respectively). Post-digestion analysis similarly revealed that toughness and fracture strength most closely resembled the dominant matrix of the hybrid's material makeup. Together, these results show that the hybrid printing strategy can be used to produce novel tissue constructs with controllable degradation rates, while simultaneously retaining the desired mechanical properties upon further *in vivo* incorporation.

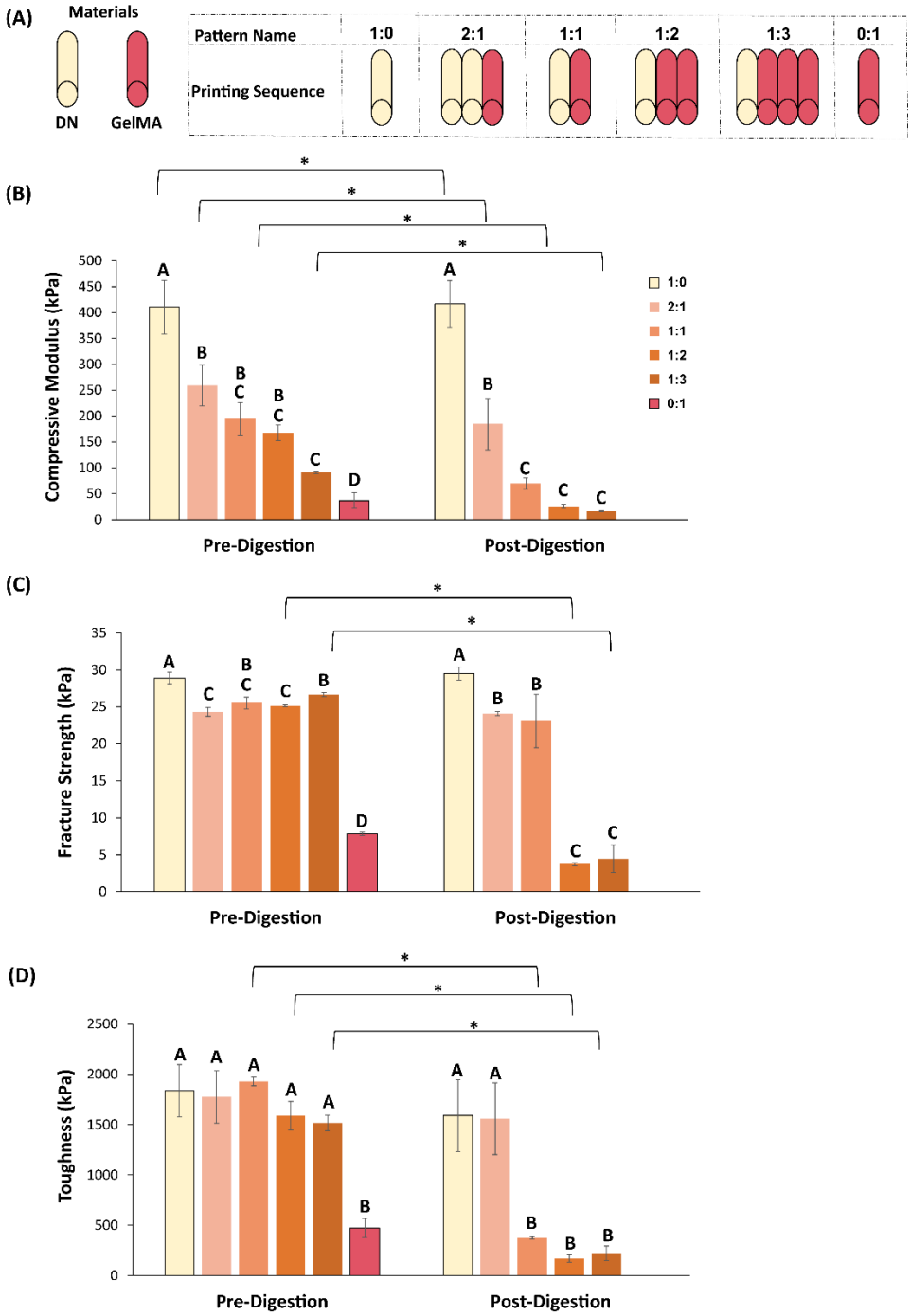

Figure 3.3: Mechanical testing of various print patterns. A) Visual description of the various print patterns used to fabricate hybrid scaffolds. Uniaxial compression testing was performed on hybrid disc scaffolds both before and after experiencing GelMA digestion via collagenase IV. Mechanical properties, such as B) compressive modulus, C) fracture strength, and D) toughness were characterized to ensure hybrid scaffolds exhibited similar properties to soft tissue. n=5 and mean ± standard deviation is depicted. Data was analyzed using single factor analysis of variance (ANOVA)

followed by Tukey's Multiple Comparison Test assuming normal data distribution with a confidence of 95% ($p<0.05$).

3.3.3 Scaffold Aesthetic Properties Mapped with CloudCompare

In addition to maintaining similar mechanical properties to native soft tissue, shape retention is of upmost importance to ensure long-term success of the soft tissue reconstruction. To this end, a model of an adult human nose was designed and scaled down to 1/3 of the average physiological size and printed with the hybrid inks (**Figure 3.4**). Again, the alternating patterns of DN ink to sacrificial GelMA bioink were used to print the complex nose shapes, and the scaffolds were 3D scanned with a Hexagon ROMER Absolute Arm both before and after digestion to determine variations in scaffold surface and shape. Iconic characteristics of the scaffold (i.e. width, length, height, and curvature, Figure 3.4B) were measured from each surface scan. Across all patterns, a high degree of shape retention was observed with the highest deviation of 14.9 ± 3.0% change in width, 13.0 ± 2.7% change in length, and 4.9 ± 3.3% change in height for the 1:3 pattern. Significant changes in scaffold curvature was only displayed in the 1:2 and 1:3 print patterns by 15.0 ± 4.8% and 23.3 ± 8.3% respectively when compared to pre-digestive values. As the GelMA content increased, the peak height of the scaffold decreased post digestion, which resulted in subsequent decreases in scaffold curvature and increases in scaffold width and length.

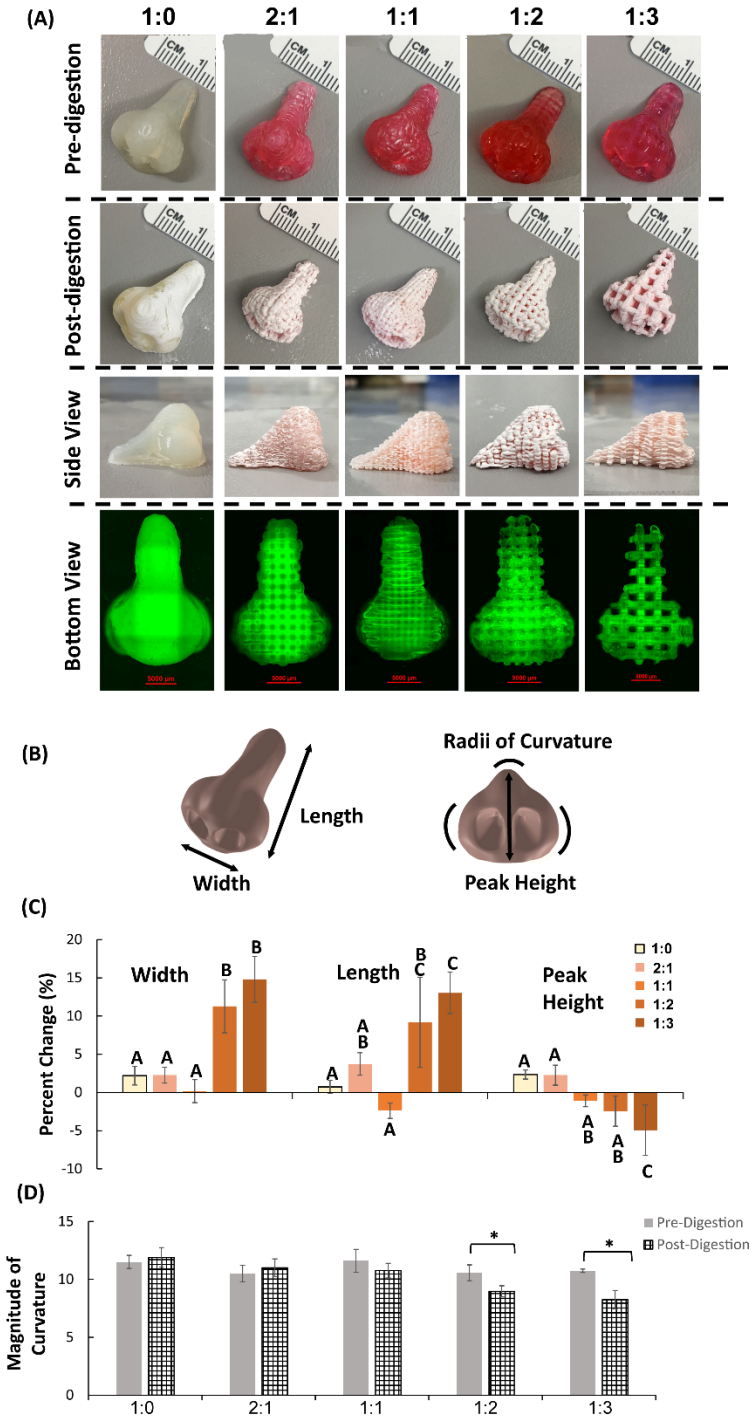

Figure 3.4: Complex scaffold shape retention. A) Noses were printed in various patterns of double network ink and GelMA and further subjected to collagenase IV digestion (Print patterns PEG:GelMA of 1:0, 2:1, 1:1, 1:2, and 1:3). B) Scaffold dimensions were recorded and compared to its original fabricated form, specifically C) width, length, and peak height. D) Magnitude of curvature was also calculated and recorded for each hybrid pattern. n=4 and mean ± standard deviation is depicted.

Data was analyzed using single factor analysis of variance (ANOVA) followed by Tukey's Multiple Comparison Test assuming normal data distribution with a confidence of 95% ($p<0.05$).

The development of this new printing technique also demands the development of a new approach to qualitatively assess scaffold shape maintenance. The application of finite element mesh analysis via a 3D evaluation software named CloudCompare allows both quantitative and qualitative characterization of shape deviations with such high detail that has not yet been visualized in the Tissue Engineering field. Thus, heat map analysis was performed where the surface mesh data sets were superimposed on each other for pairwise comparisons (MeshLab), and deviations between the pre- and post-digested scans were determined using CloudCompare (**Figure 3.5**). Detailed methods regarding analysis of the scaffold design using the CloudCompare software can be found in the Supplemental Methods section. This data holistically shows the DN ink's ability to dictate scaffold shape during degradative remodeling processes. Color maps illustrated a spectrum of yellow (indicating the standards of a perfect match), red and blue color (both indicating the lack of coincidence) depending on the DN-GelMA pattern used. The distribution of the points in relation to the distance from the referenced pre-digested surface can be visualized on the right side of these maps. Together, the color maps and graphic data displayed in Figure 3.5 show a gradient in shape maintenance depending on the pattern used during scaffold fabrication. In agreement with the above-mentioned results, the control pattern 1:0 DN-GelMA displayed the best ability to maintain the complex shape of the nose post exposure to collagenase IV, as this scaffold did not experience any degradation. This mirrors the mechanical results previously shown in

Figure 3.3, as an increase in modulus is predicted to be from this pattern's slight swelling. Patterns 2:1 and 1:1 similarly swelled; this is hypothesized to have occurred once the constricting GelMA strands dissolved post collagenase IV digestion and PEG strands were able to relax and swell. Pattern 1:2 displayed adequate ability in preserving the nose shape when compared to its original printed structure, with <1 mm deviation. Lastly, pattern 1:3 showed the least in ability to maintain shape, equivalent to 2mm deviation from its original shape.

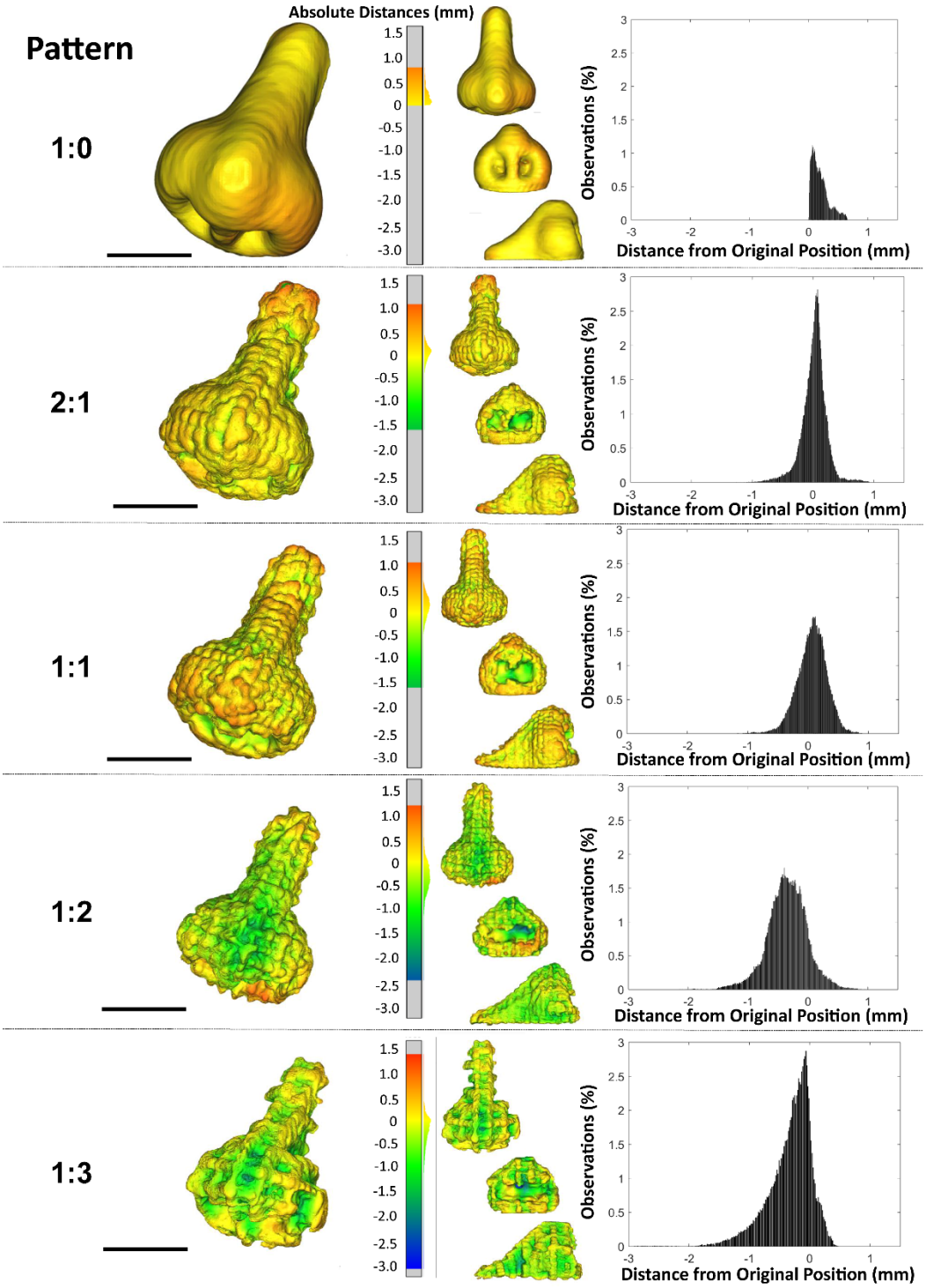

Figure 3.5: Color maps displaying point cloud comparisons. Hybrid nose prints were 3D scanned with a Hexagon Romer Absolute Arm both before and after GelMA digestion, such that finite element meshes could be produced and compared. Color maps display deviations of the digested scaffold to its original form, where red/orange designate positive deviations (expansion) and green/blue designate negative deviations (shrinkage). Histograms displayed on the right graphically show the

percentage of mesh points that deviated from their initial positions. Scale bar displays 8 mm.

Taken together, these results indicate that the double network hydrogel can have a gradient effect on dictating scaffold shape during degradative remodeling processes, allowing the ability to tailor each fabricated scaffold to its intended application. However, overall scaffold shape is maintained for all patterns examined. Consequently, an effective degree of the non-degradable DN ink can be chosen to tailor the desired mechanical properties of the scaffold, such as delicate fat adipose tissues, or stiffer muscular tissues, with promising long-term results.

3.5 Conclusion

We have developed a 3D printing strategy for soft tissue engineering which involves a hybrid scaffold composed of sacrificial layers that allows for tissue integration and a skeletal network that maintains mechanical and shape integrity. The novelty of this paper lies in the versatile and cell-friendly 3D printing platform that we have devised, and the revolutionary application of mesh analysis for assessing scaffold aesthetic properties for soft tissue engineering. We have successfully applied these strategies to commonly-used hydrogels such as GelMA, PEG-based, and alginate materials utilizing a process of multi-material printing that can be readily accessed by the 3D printing and biomedical community. DN-GelMA printing patterns used to fabricate complex scaffolds highly dictate both the composite's mechanical properties and ability to maintain shape post degradation processes. Cytotoxicity characterization of the hybrid print revealed high proliferation and cell spreading after multiple weeks of *in vitro* culture. Our key innovation is producing a

biomimetic hydrogel graft consisting of both degradable and non-degradable parts that harmoniously coexist to promote tissue integration while maintaining its original printed structure.

To our best knowledge, there are no previous reports on the creation of volume-stable, mechanically relevant, biocompatible soft tissue grafts fabricated with neither single nor multi-material printing. Overall, a modular and biocompatible ink formulation was developed that can be used to fill soft tissue defects and integrate with the surrounding environment while providing long term mechanical integrity and shape retention.

Chapter 4: Orchestrated Structural and Bioactive Matrices for Engineering a Nipple-Areola Construct

4.1 Introduction

As discussed in Chapter 2, soft tissue engineering fabrication and culture strategies represent a promising and underexplored avenue for nipple reconstruction. Both nipple and soft tissue types characteristically exhibit delicate tactile properties and defined aesthetic features. Current SFS techniques to restore the nipple are inadequate, as these procedures are associated with high rates of infection, multidirectional scarring, and severe nipple flattening[43,203]. More importantly, this clinical practice is insufficient for the psychological health needs of breast cancer survivors as it necessitates repeated intervention due to projection loss. Accordingly, nipple reconstruction remains as an unresolved clinical challenge and can benefit from a reimagined, tissue regenerative approach.

One of the challenges that accompanies the reconstruction of this tissue type is accurately capturing the relevant size and tactile properties of the nipple. Various attempts to enhance nipple projection have been previously documented in literature, such as autologous fat[84,203], cartilage[80,103,204,205], bone[92], contralateral nipple[86,206], rolled dermal grafts[38,207], and synthetic silicone implants[96], but these methods have not been regularly adopted in clinical reconstructive practice due to negative patient feedback. Although the insertion of additional material to the dermal flap does

enhance the projection for extended periods of time, dissatisfaction remains among patients due to the stiff sensation caused by the foreign material. Autologous fat and cartilage grafting report complications of infection, seroma, and fat necrosis, while allogeneic and synthetic materials have similar complications along with additional risks of exposure (implant perforation through the skin) and over projection. Multidirectional scarring is also an end result in these procedures, as complicated dermal flaps are still necessary to suture the addition in place. A method that produces a more natural stiffness, regular projection, and minimal scarring would increase patient satisfaction.

Our present study seeks to develop a tissue engineered dermal scaffold that promotes the formation of a lasting nipple-areola complex for mastectomy patients. Previous work on a dual hybrid printing technique of synthetic and cell laden bioinks has offered a conceptual method to fabricate shape-retaining soft tissue scaffolds with robust mechanical properties. Our current study incorporates entangled methylcellulose (MC) and PEG networks as the synthetic component of the scaffold to provide strength and resistance to projection degradation, while GelMA seeded with primary human dermal fibroblasts acts as the natural component to aid in dermal regrowth. To this end, our first objective was to fine-tune the MC-PEG bioink to obtain a hybrid scaffold that mirrors the mechanical properties of nipple tissue. Our second objective was to evaluate the fibroblastic contraction experienced during an extended period of *in vitro* culture and to investigate which printing parameters result in an unchanged nipple projection. Overall, our results showcase the *in vitro* capacity

of our hybrid 3D printed scaffolds to provide accurate physical cues for nipple-areola reconstruction and inspires potential for *in vivo* implantation.

4.2 Materials and Methods

MC-PEG Double Network Ink

Our previous double network ink was modified with the substitution of alginate with methylcellulose. It was synthesized by first dissolving 15% (w/v) methylcellulose dehydrated powder with 10% (w/v) four-arm PEG thiol and 10% (w/v) four-arm PEG norbornene in deionized water. Lithium phenyl-2,4,6- trimethylbenzoylphophinate (LAP, Sigma-Aldrich) with a 0.2% (w/v) ratio was added and thoroughly mixed under 80°C. The ideal amount of methylcellulose was tested with systematic extrusion through a printer cartridge, and further evaluated in its swelling properties.

GelMA Bioink

Similarly, as before, GelMA was synthesized via dropwise addition of methacrylic anhydride (MA; Sigma-Aldrich) to a Type A porcine skin gelatin solution dissolved at 10% (w/v) in phosphate-buffered solution (PBS: Thermo Fisher Scientific). The mixture was diluted with PBS to stop the reaction and centrifuged at 2000g for 2 min. The supernatant was collected and dialyzed (10 kDa molecular weight cutoff; Thermo Fisher Scientific) to remove the excess salts and acids. The dialyzed GelMA was then lyophilized and stored in -80°C. For printing, lyophilized GelMA was dissolved at 7% (w/v) in fibroblast media at 50°C for 10 mins. LAP imitator was added to the

GelMA solution at a concentration of 0.1% (w/v) at 50°C for 15 min, and later sterifiltered with a 0.4μm filter. Primary adult, normal human dermal fibroblasts (Passage 3, Lonza) were then added at a concentration of $2x10^6$ cells/mL (for cell viability assay) or $10x10^6$ cells/mL (for the shape retention assay) and were homogenously mixed throughout the solution. The prepolymer solution was then loaded into a sterile syringe barrel and allowed to equilibrate for 30 min at 23°C.

Hybrid Scaffold Fabrication

Physiologically relevant human-shaped nipple areola constructs were printed with various print patterns (as explained in Chapter 3, PEG:GelMA- 1:0, 1:1, 1:2, 1:3, 0:1). All model scaffolds were sliced into layers with a slicing thickness equal to 80% (0.32 mm) of the needle size (0.4 mm) before printing). Each printed layer was exposed to UV light (5 mW/cm^2) for 5 s, and the final print was placed in a UV box (5 mW/cm^2) and exposed for 3 more min. For the both the cell viability and shape retention assays, the hybrid nipple-areola prints were immediately transferred into 6-well tissue culture plates and were fully submerged in media, with media changes every 2 d for 2/3 weeks. For mechanical testing, half of the produced scaffolds were exposed to collagenase IV (500 Units/mL, Worthington Biochemical Corporation) to evaluate the synthetic material impact on the composite mechanical properties.

Mechanical Testing

Compression testing was performed on a Dynamic Mechanical Analyzer (DMA Q800, TA Instruments) with a strain sweep (0-15%) and a load of 0.01N at 1Hz

frequency. Elastic modulus for each sample was calculated by determining the slope of the linear region of the stress-strain curve (strain region 3-5%). These compressive moduli were compared against fresh pig nipple teat (Tissue Source, Lafayette) for a close *in vivo* representation of nipple mechanical properties.

Cell Culture

Primary Adult, Normal Human Dermal Fibroblasts (Lonza) were cultured as per the manufacturer's specifications with Dermal Fibroblast Growth Medium and Growth Factor BulletKit (Lonza). Prior to printing, cells were passaged using tissue culture plates and Trypsin/EDTA, with media changes every 2 days. Cells were then lifted, spun down (500g for 5 min) to create a pellet, and resuspended in GelMA ink.

Cell Viability Assay

Cell viability was assessed using a Live/Dead assay (Invitrogen) following the manufacturer's protocol. Briefly, 3D printed hybrid nipple-areola constructs (35 mm diameter, 8 mm projection height) were incubated with 4µM calcein AM and 2µM ethidium homodimer for 1 h at multiple timepoints (Day 0, Day 14). Fluorescent images (n=3 per sample) were taken using a fluorescence microscope (Nikon) and processed using Nikon's NIS Elements AR Software. Cell viability was determined from the ratio of the number of live cells to the total number of cells.

Point Cloud Generation

The ROMER Absolute Arm (Hexagon) was used to generate point clouds containing

high geometric detail of the nipple-areola surfaces. Scaffolds were sprayed with water soluble paint prior to scanning for greater ease in detecting surfaces. The nipple-areola scaffolds were sequentially scanned at multiple angles and the surfaces were selected using the software's editing brush tool. After the total region of interest was created, a volume was generated and exported as a stereolithography (STL) file.

Surface Alignment

To maintain sterile *in vitro* culture conditions for the contracted nipple scaffolds, we could not spray/scan the same scaffold twice. Therefore, we could not compare the same scaffold from before/after contraction to visualize the exact scaffold deformation. STL files of all unique samples were imported into the open-source software MeshLab (Visual Computing Lab- ISTI CNR) for an averaged comparison among projection contraction amongst hybrid scaffold type. Propagation of error was necessary in the quantitative cloud comparisons, which is further discussed in the next methods section. With MeshLab software, the alignment tools ('point-based alignment' and 'process tool alignment') were used by selecting four possible points along the base areola for each hybrid model.

Cloud Comparison

The two repositioned STL meshes for each pattern were uploaded into the CloudCompare software and point cloud comparison was performed by selecting the precontracted nipple projection as the reference and the contracted nipple projection as the compared object. A color map was generated, which calculated the distance of

points in the compared cloud to the nearest point in the reference precontracted cloud. The color map colors were further modified in this chapter to better visualize the contraction of the nipple scaffold. White color signified coincident points, while a red spectrum (positive deviation) or blue spectrum (negative deviation) indicated a lack of coincidence. The accompanying histogram to the right of the colormaps provide the concentration of points analyzed by its distance. CloudCompare's Point Picking function allowed distances to be obtained along the diameter of the nipple projection, projection height, and the projection's radius of curvature. The Fit Sphere function rendered dependable approximations in curvature of the nipple projection.

Since each scaffold could not be directly compared, the error to obtain percent difference mean values must be propagated. To propagate the error, we derive the formula from the definition of percent difference:

$$Percent\ Difference = \frac{\Delta V}{V_1} * 100 = \frac{V_2 - V_1}{V_1} * 100 \quad (1)$$

Both the numerator and denominator of the above equation contain its own uncertainties (V_2-V_1) and (V_2). Equation 3 shows the uncertainty for the numerator, while Equation 6 incorporates this uncertainty into the final value of the propagated error:

$$\Delta V = V_2 - V_1 \pm \delta\Delta V \quad (2)$$

$$\delta\Delta V = \sqrt{\delta V_1^2 + \delta V_2^2} \quad (3)$$

Full derivation:

$$N = \frac{\Delta V}{V_1} \pm \delta N \tag{4}$$

$$\frac{\delta N}{N} = \sqrt{(\frac{\delta \Delta V}{\Delta V})^2 + (\frac{\delta V_1}{V_1})^2} \tag{5}$$

$$\delta N = N * \sqrt{(\frac{\delta \Delta V}{\Delta V})^2 + (\frac{\delta V_1}{V_1})^2} \tag{6}$$

Statistical Analysis

Data were analyzed using single factor analysis of variance (ANOVA) followed by Tukey's Multiple Comparison Test assuming normal data distribution with a confidence of 95% ($p < 0.05$).

4.3 Results and Discussion

4.3.1 Synthetic Ink Modification for *In Vivo* Application

It is of upmost importance that the materials comprising the nipple-areola scaffold are both biologically compatible and mechanically stable in order to produce a graft suitable for future *in vivo* implantation. In our previous work, the synthetic material was defined as a double network of ionically crosslinked alginate and covalently crosslinked poly(ethylene) glycol. Although alginate has been used in previous implantation studies, this composition is not the most suitable choice for our application, as the alginate network requires a constant replenishment of calcium ions to maintain its ionic interactions. Without these ions, the alginate chains slowly leach out of the gel and subsequently create large voids in the polymer network, which

results in significant swelling of the scaffold (can be visualized in Chapter 3 Figure 3.2). To combat this limitation, we modified the synthetic ink by substituting methylcellulose (for alginate) as the second self-interacting, interpenetrated network with poly(ethylene) glycol. Methylcellulose (MC), a water-soluble derivative of the polysaccharide cellulose, has been FDA-approved for use in medicinal capsules and tablet coatings as clinical studies have proven the material to be non-allergenic, non-toxic, and biocompatible[208]. This polymer contains highly methylated glucose zones that hydrophobically interact to create a 'turbid strong gel', and the gelation of this material is solidified through exposures of specific temperatures[209,210]. In literature, MC has previously been shown to exhibit stable hydrophobic chain interactions throughout a large range of pH (3-11)[211] and resist enzyme degradation[212], two critical properties that are necessary for our synthetic material to maintain the scaffold's projection as the biodegradable components of the graft are reconstituted by infiltrating inflammatory host cells. Since the material and biological properties of MC greatly align with those envisioned for our scaffold, the first objective of this work was to optimize MC concentration to produce a bioink with reproducible swelling and extrusion properties.

Because of its unique thermal gelation, methylcellulose is a prime candidate for pressure-driven extrusion printing. We created 3 concentrations of methylcellulose (10 w/v%, 15 w/v%, and 20 w/v%) homogenously mixed with a 20% PEG solution and evaluated each in terms of its printability and swelling post 24-hour incubation in PBS (pH 7) at 37°C . The bioink containing 15 w/v% methylcellulose exhibited the

most consistent strand diameter and demonstrated a minimal degree of swelling (16.2 ± 1.3%) and was therefore used for the remainder of the experiments. The high polymer weight percentage (MC and PEG content collectively) in these hydrogels allows for a greater degree of crosslinking, as both hydrophobic MC interactions and covalent PEG bonds are present, and results in a more densely packed polymer network. Once incorporated in a hybrid print, this helps minimize the swelling of the scaffold and ultimately aids in the maintenance of the nipple geometry (**Figure 4.1**).

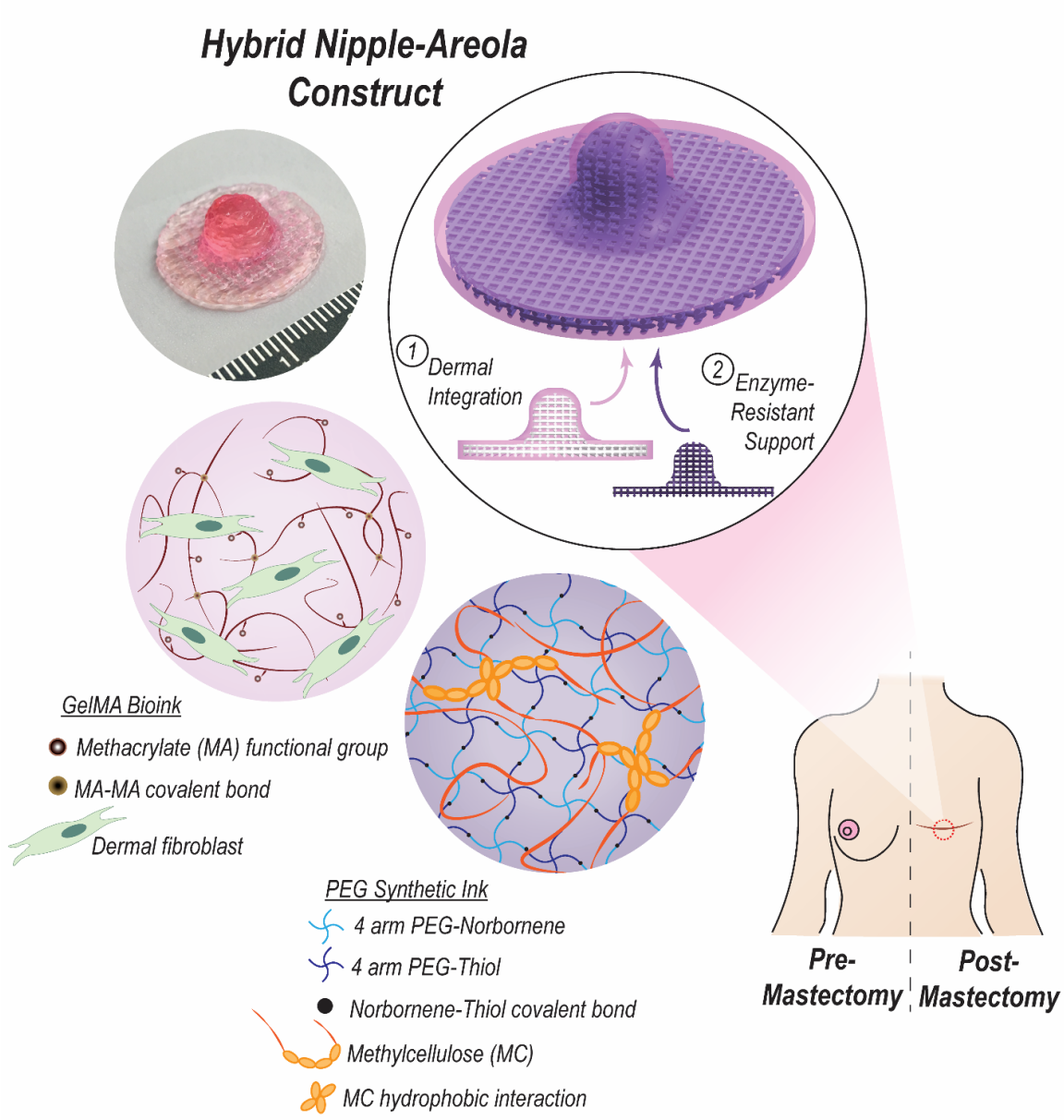

Figure 4.1: Components of the Hybrid Nipple-Areola Implant. Two bioinks (GelMA and MC-PEG) are co-printed in various patterns to create a hybrid regenerative scaffold. The GelMA bioink is composed of gelatin methacrylate polymers that can be crosslinked via UV light exposure when photoinitiator LAP is present. Fibroblasts can be encapsulated within the GelMA bioink and serve as a biodegradable region for host dermal integration. The MC-PEG synthetic ink is a double polymer network composed of methylcellulose autonomously interacting with its hydrophobic groups and poly(ethylene) glycol covalently crosslinked upon UV exposure.

4.3.2 *In Vitro* Nipple Implant Functionality

Physiologically relevant nipple-areola scaffolds were fabricated with alternating MC-PEG and GelMA bioinks in various print patterns (similar to the methods described in Chapter 3). According to published reports on the morphological characteristics and size of the human nipple-areola complex, a human nipple projection varies in 6-10 mm in height, 8-13 mm in projection diameter, and 30-40 mm in areola diameter[79]. Our grafts matched this population size with an average projection height of 8.2 ± 0.65 mm, 9.3 ± 0.43 mm projection diameter, and areola diameter of 29.2 ± 0.36 mm (**Figure 4.2**). By strategically altering the print patterns of the two bioinks, various hybrid compositions were analyzed in terms of internal cell viability and mechanical properties. It was equally imperative that we fabricated a graft that 1) provided adequate diffusion to support cellular proliferation and 2) exhibited a stiffness that mirrors the natural value of nipple tissue to account for patient preference.

We first investigated the cell viability in response to the print pattern used to fabricate the hybrid scaffold, since the MC-PEG dense polymer network may affect the internal diffusion of media. Across print patterns 1:2 and 1:3, the primary adult human dermal fibroblasts (2 million cells/mL concentration) displayed a high and acceptable range of viability throughout the entire scaffold, where the quantitative results ranged from 78.12 ± 13.06% and 85.25 ± 6.58% for day 1 and 78.35 ± 9.59% and 74.98 ± 9.52% for day 14 respectively. Pattern 1:1 is the only hybrid that shows a significant decrease in cell viability, with an initial value of 81.42 ± 12.64% on day

1 that decreases to 57.37 ± 6.67% by day 14. This may signify that a balance is needed between the synthetic and biodegradable components in the scaffold's design to obtain a matrix with favorable diffusivity properties that can support high cell viability throughout the graft. Images taken at higher magnification (20X) revealed that the living fibroblasts (positive Calcein AM stain) displayed a healthy morphology throughout all hybrid compositions. Day 1 images portrayed cells with a rounded morphology, which is expected due to the cells' recent encapsulation in GelMA and pressure experienced during the printing process. By day 14, however, the average cell spreading area gradually increased. These results indicate that 1:2 and 1:3 hybrid scaffold compositions support sufficient media diffusion, as no significant difference in cell viability is noted throughout the 2-week *in vitro* culture.

The compressive modulus of hybrid nipple-areola scaffolds was determined to demonstrate that the stiffness of the projection can mimic those values experienced *in vivo*. The achievable range of modulus for the hybrid scaffold is bound by the modulus of the two single component hydrogels: MC-PEG at 152.20 ± 4.07 kPa and GelMA at 60.73 ± 7.40 kPa (Figure 4.2D). No significant difference in stiffness was observed between the hybrid prints, and all values aligned with the stiffness of pig teat tissue (our closest *in vivo* prediction) within one order of magnitude. To visualize the influence of the internal PEG structure on scaffold stiffness, we digested the GelMA strands by incubating the scaffolds in a collagenase solution for 24 hours at 37°C and reassessed the mechanical properties of the scaffolds. In this scenario, we observed that the print pattern had a gradient effect on scaffold stiffness. For

example, the 1:1 pattern (50.40 ± 5.75 kPa) is significantly stiffer than both the 1:2 sample (13.27 ± 4.78 kPa) and the 1:3 sample (11.63 ± 5.16 kPa). Other groups have reported that implants composed of degradable materials have the tendency to collapse once implanted *in vivo*, as the biodegradable materials experience rapid degradation during the triggered innate immune response[199,213]. This indicates that the inclusion of MC-PEG in the hybrid scaffold may improve the incorporation of the graft by increasing structural integrity of the implant. To further investigate the nipple projection's structural integrity, analysis in the shape retention of the hybrid scaffolds was performed in the next cell study.

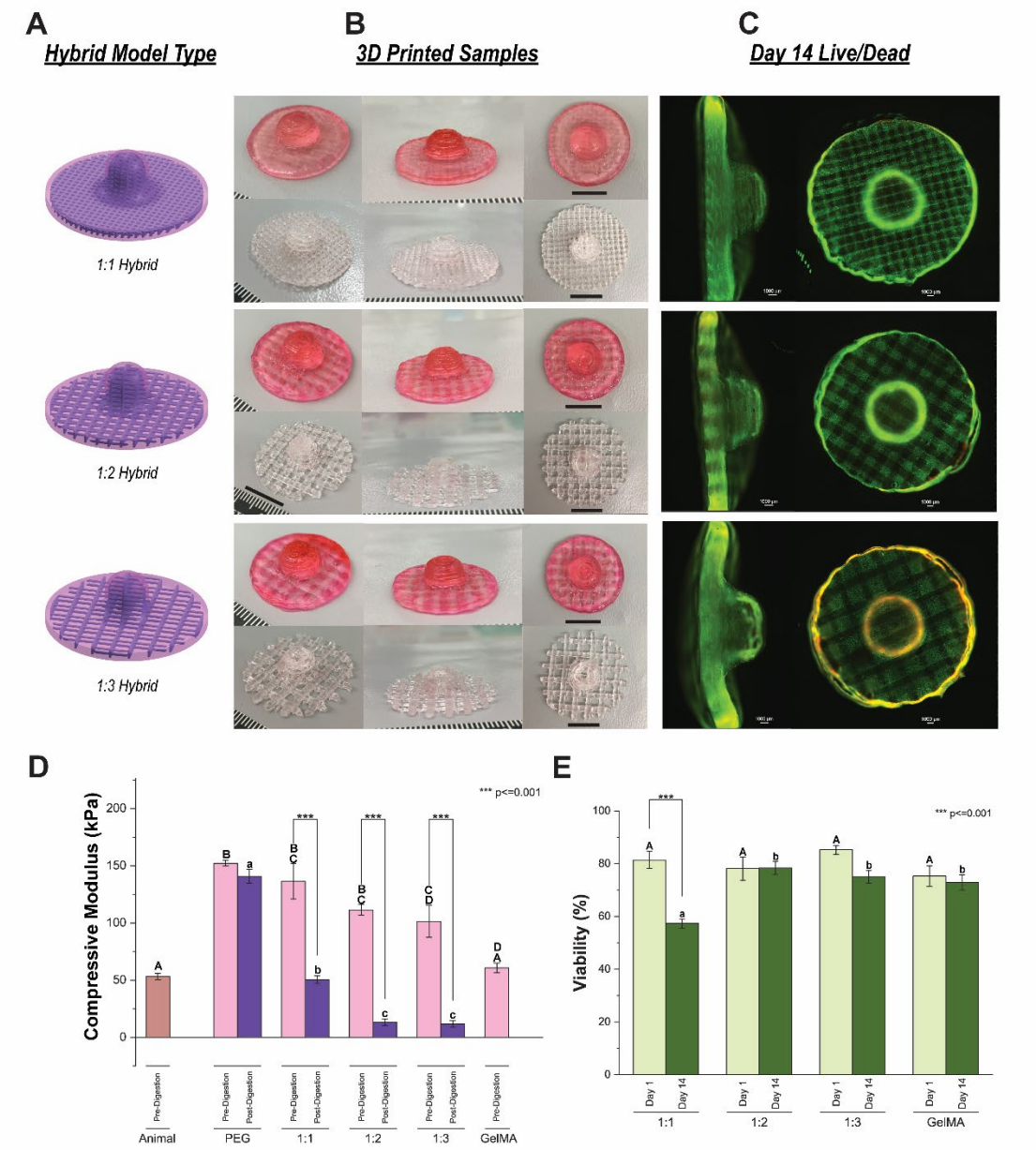

Figure 4.2: *In Vitro* Implant Functionality. Hybrid nipple-areola scaffolds were 3D printed using the Envisiontec Bioplotter. **A**. CAD designs of each hybrid print, displaying the deposition of GelMA (pink) and PEG (purple) bioinks. **B**. Representative images of each hybrid print, both before and after collagenase digestion, scale bar 10 mm. **C**. Cell viability visualized via Live/Dead (Calcein AM green, live cells; Ethidium Homodimer red, dead cells). **D**. Uniaxial compression testing was performed on hybrid scaffolds both before and after experiencing collagenase digestion with respective compressive modulus recorded (n=3, $p<0.001$). **E**. Fluorescent images (n'=5, over n=3 biological samples) were taken using a fluorescent microscope (Nikon) and processed using a configured MATLAB code. Cell viability was determined from the ratio of the number of live cells to the total number of cells. Data was analyzed using single factor analysis of variance

(ANOVA) followed by Tukey's Multiple Comparison Test assuming normal data distribution with a confidence of 99.9% ($p<0.001$).

4.3.3 Nipple Projection Shape Retention

Nipple flattening is the most notable pitfall of SFS reconstruction as its inevitable occurrence causes detrimental effects to the psychological health of the patient (**Figure 4.3**). In order to improve upon these clinical outcomes, our hybrid implant must be able to maintain projection while subjected to the highest level of cellular contractile forces. To test this phenomenon *in vitro*, a high concentration of primary dermal human fibroblasts (10 million cells/mL) was encapsulated in GelMA bioink and printed with MC-PEG into nipple projection scaffolds with various print patterns (mimicking Chapter 3- PEG control, 1:1, 1:2, 1:3, GelMA control). The areola was excluded from the scaffold design to help minimize experimental costs and print time. After 3 weeks of submerged culture, the scaffolds were 3D scanned with a Hexagon ROMER Absolute Arm, and their surfaces were compared to freshly printed nipple projection scaffolds (to maintain sterile culture conditions) via point cloud comparisons through CloudCompare. We have previously documented a shape assessment technique that utilizes the 3D evaluation software named CloudCompare to perform finite element mesh analysis for both quantitative and qualitative characterizations[214]. For these color maps, regions that display a white color signified coincident points, while a red spectrum (positive deviation) or blue spectrum (negative deviation) indicated a lack of coincidence (Figure 4.3B). The color maps mirrored our previous results found in the compressive testing mentioned above, where the print patterns containing higher MC-PEG content had a greater retention of nipple shape than those with higher GelMA content. Patterns 1:0 and 1:1 exhibited

minimal scaffold swelling and shrinkage, while pattern 1:2 moderate shrinkage of <0.5 mm, and patterns 1:3 and 0:1 displayed the highest shrinkage of <1.2 mm. There appears to be uniform contraction across the projection diameter, as seen by the consistent blue hue displayed in maps 1:3 and 0:1. Although the hybrid patterns 1:2 and 1:3 experienced significant lateral contraction, they still were able to retain their recognizable and pronounced nipple projection.

Point clouds were also compared quantitatively amongst all pattern types (**Figure 4.4**B-D). CloudCompare's Point Picking function allowed distances to be obtained along the nipple projection height and diameter, and the Fit Sphere function rendered dependable approximations in the radius of nipple projection curvature. The error of all quantitative results was propagated since each scaffolded was treated under sterile conditions (further description in methods). Across all patterns, a high degree of shape retention was observed with the highest deviation of -11.31 ± 3.42% change in projection diameter, -10.29 ± 3.72% change in projection height, and -9.33 ± 1.69% change in radius of curvature for the 1:3 hybrid scaffold. The CloudCompare color maps and quantitative comparisons of scaffold measurements between print pattern suggest that the internal MC-PEG structure can aid in the shape retention of the scaffold's nipple projection. Its presence helps prevent both lateral and vertical contraction of the nipple, and thus aids in retaining curvature of the scaffold geometry. Without this synthetic component, the projection decreases in radius, height, and curvature, as displayed in the 0:1 GelMA control. Overall, the hybrid scaffolds demonstrate promising results in biocompatibility, mechanical properties,

and shape retention and may serve as an effective strategy for the reconstruction of nipple-areola constructs.

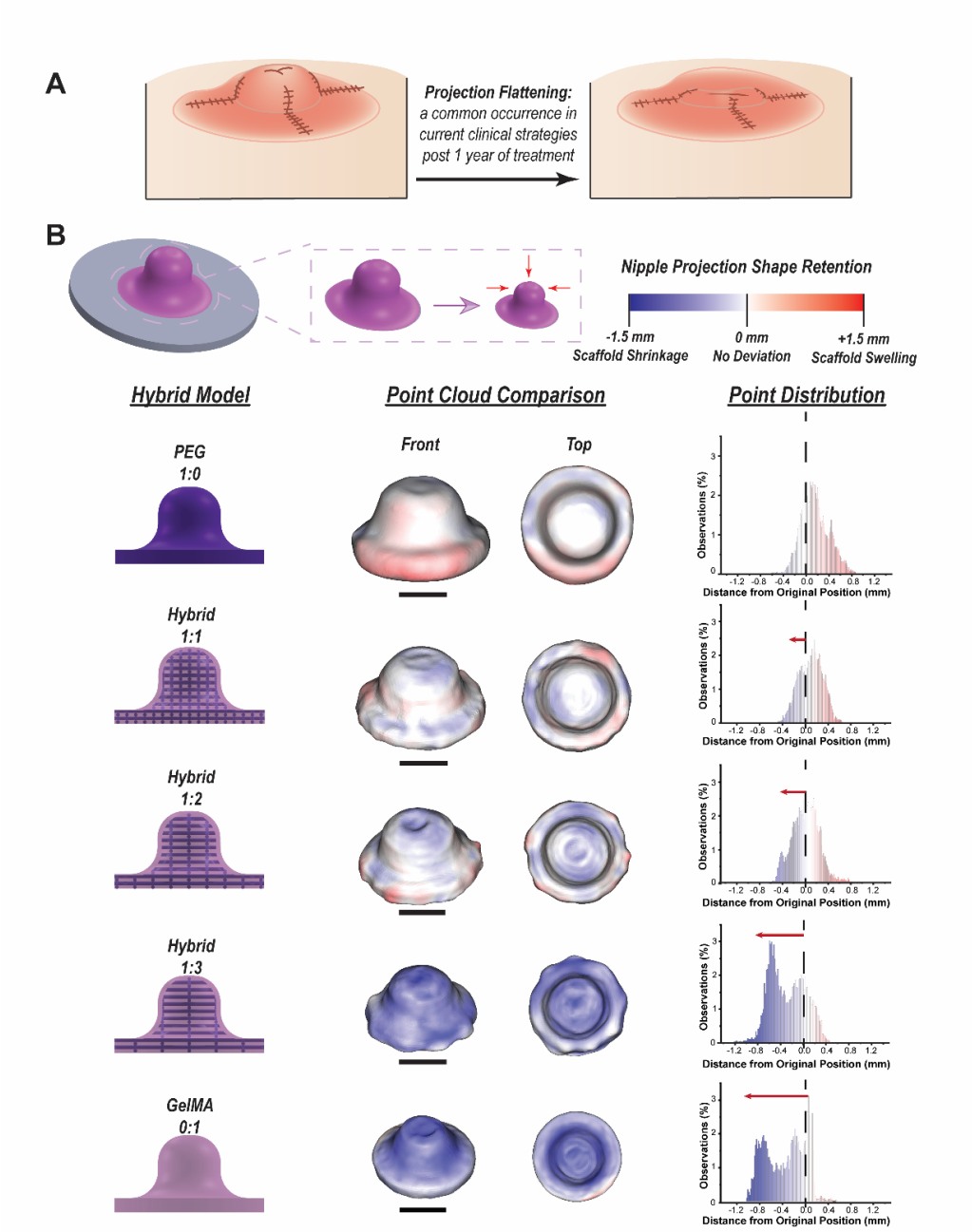

Figure 4.3: Nipple Projection Shape Retention while Subjected to Fibroblast Contraction. **A**. Projection flattening is a common occurrence in clinical nipple reconstruction while skin flap suturing techniques are used. **B**. Hybrid scaffolds with nipple geometry were printed with a high concentration of primary human dermal fibroblasts (10 million cells/mL) and cultured for 3 weeks *in vitro* under submerged conditions. The scaffolds were then 3D scanned, and their respective point clouds were compared. Color maps (center) display deviations of the contracted scaffold to its original form. Histograms (left) graphically display the percentage of points that deviated from their initial positions. Scale bar displays 5mm.

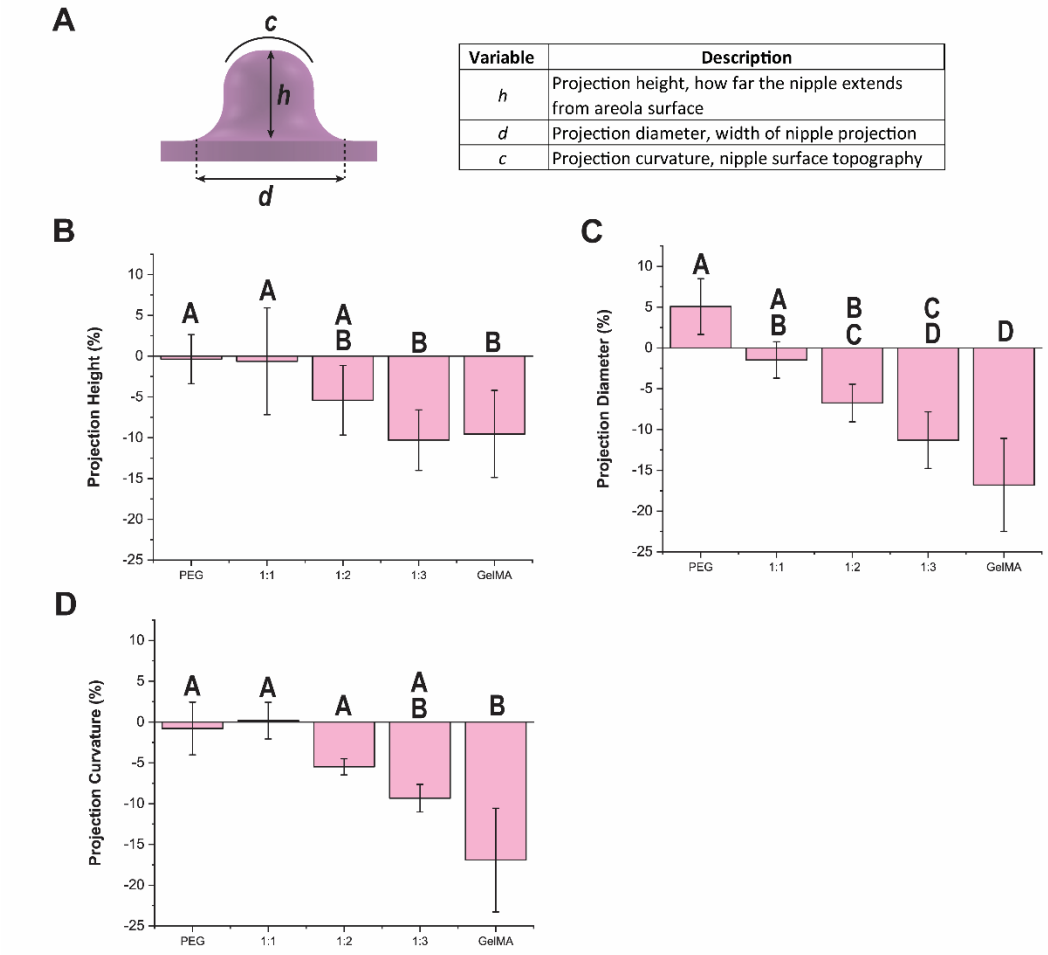

Figure 4.4: Quantitative Comparisons Between Hybrid Scaffold Type. **A**. Scaffold dimensions were recorded and compared to its original fabricated form, specifically **B** projection height, **C** projection diameter, and **D** projection curvature. Percent differences display a gradual decrease in scaffold shape, as the scaffolds experienced contraction over the 3-week *in vitro* culture. n=3 and mean ± propagated error depicted. Data was analyzed using single factor analysis of variance (ANOVA) followed by Tukey's Multiple Comparison Test assuming normal data distribution with a confidence of 95% ($p<0.05$).

4.4 Conclusion

In this work, a robust platform that generated physiologically relevant nipple-areola complex was presented. We successfully incorporated an enzyme and pH resistant polymer, methylcellulose, into an extrudable synthetic ink and fabricated a hybrid nipple tissue scaffold with promising results for future *in vivo* implantation. Through fibroblast cell patterning, we found the incorporation of the MC-PEG material helped helps prevent both lateral and vertical contraction of the nipple, and thus aids in retaining curvature of the scaffold geometry. Cell viability characterization also revealed sufficient dermal cell health after multiple weeks of *in vitro* culture. Our versatile approach can generate customized, acellular nipple-areola regenerative grafts that can be seamlessly incorporated into today's breast reconstruction practices.

Chapter 5: Foreign Body Response to Hybrid Prints in a Rat Subcutaneous Model

5.1 Introduction

While *in vitro* development of tissues is the starting point of a tissue-engineered product, an appropriate *in vivo* model is crucial to validate the tissues' subsequent function. There exist many medical, legal, and ethical considerations when new biomedical products come to fruition, and thus intense preclinical investigations are necessary before the product is available to the masses. Several factors need to be assessed in macroscale once the product is introduced to the host, for example, the role of angiogenesis in a newly created tissue, complex host immune reactions to the graft that could ignite inflammation and/or rejection, as well as functional considerations, such as innervation, rheological graft properties, or the effects of surgical interventions[215]. The complexity of these factors makes it impossible to effectively and holistically evaluate the product *in vitro* and thus it is critical to analyze the outcomes of multiple animal *in vivo* studies to properly predict its success upon human implantation.

For an effective soft tissue engineering strategy, successful integration between the tissue-engineered construct and the surrounding natural environment is of paramount importance. A poorly integrated scaffold often leads to impaired functionality within a few months[216]. True integration can be achieved by designing smart templates made from biomaterials that provide cues to promote host cell migration and

functional tissue connections. Scaffold porosity, pore network architecture, and surface roughness can drastically affect the diffusion of nutrients and cellular migration within the tissue-engineered construct[217]. Ideally, scaffold physical cues should be engineered to mimic the mechanical properties with its surrounding environment without inhibiting necessary host cell infiltration.

Additionally, the host immune response is a factor that greatly influences tissue regeneration. The immune reaction to an implant begins with an acute response to the injury and an innate recognition of foreign materials; this reaction continues with a subsequent chronic immune response when there is an influx of macrophages and the development of an avascular fibrous capsule. In addition, polymorphonuclear neutrophils infiltrate the wound and release reactive oxygen species that not only clear cellular debris but can also result in rapid degradation of the biomaterial scaffold[218]. Monocytes and fibroblasts that are recruited to the injury site also release inflammatory cytokines, which can cause secondary damage to the surrounding tissue[219]. If the reaction is significant, it can lead to total rejection of the implant.

As discussed in Chapter 1, tissue engineering strategies actively pursued to reconstruct the nipple-areola include the implantation of autologous tissues (fat, cartilage, and bone), decellularized rolled dermal grafts, and silicone implants. However, besides the clear mechanical mismatch between these materials and nipple tissue, extensive surgical complications such as autologous tissue necrosis, donor site morbidity, and implant migration/rupture accompany these strategies. Biologically

active, acellular scaffolds remain an attractive alternative to these current strategies as it involves *in situ* tissue regeneration; by providing an instructive biomaterial matrix, the scaffold helps guide cell migration and informs the regeneration process. To enhance nipple reconstruction, an acellular 3D printed scaffold whose matrix recruits host dermal cells and relies on the body's innate regenerative ability could be used to better reproduce a well-integrated and stable nipple projection.

To expand upon on the concepts and findings from Chapter 4, this study was designed to determine whether the optimized hybrid 3D printed nipple-areola scaffolds could properly integrate with host tissue in an *in vivo* model. A subcutaneous rat model was chosen as it is a well-documented model for the evaluation of biomaterial implants[220–222]. The hybrid scaffolds were fabricated with alternating patterns of MC-PEG and GelMA bioinks (similar to the methods of Chapters 3 and 4), implanted into the dorsal subcutaneous regions in Lewis rats, and further retrieved after 4 weeks. Histological analysis was performed on the resected tissue to assess the severity of the hosts' foreign body response to the hybrid materials and to identify any possible vascularization surrounding the implant. To properly evaluate the histological responses, five blind scorers utilized a modified ISO 10993-6 Standard to assess the cellular and tissue characteristics both in and around the implant. In most cases, a mild local foreign body reaction was observed consisting of a minimal layer of multinucleated giant-like cells and a moderate infiltration of polymorphonuclear neutrophilic-like granulocytes at the implant interface, surrounded by a mild connective tissue capsule. The success of this animal trial

suggests that these hybrid nipple-areola scaffolds can provide a promising solution to nipple reconstruction.

5.2 Methods and Materials

Experimental Design

We obtained permission from our animal ethics committee to perform the experimental protocol as follows. The main goal of our study was to evaluate the cellular and tissue responses to novel hybrid biomaterial implants. All of the recorded metrics could indicate the functionality of the material for a nipple-areola specific tissue engineered scaffold. Hybrid nipple prints with a projection diameter of 9.0mm, projection height 8.0mm, and areola diameter 20.0mm were implanted under the superficial cervical fascia in 10 Lewis strain female rats. The in vivo analysis is critical due to the situational degradation expected from these scaffolds. As the biodegradable materials of the scaffolds degrade, we are interested in investigating the cell and surrounding matrix and the remaining synthetic material presence.

Scaffold Fabrication

3D models of nipple-areola constructs were first designed in SolidWorks (Waltham, MA). The two bionks used during fabrication are 1) 7% (w/v) gelatin methacrylate solution dissolved in phosphate buffered solution and 2) an aqueous solution containing 15% (w/v) autoclaved methylcellulose, 0.2% (w/v) LAP photoinitiator, 10% (w/v) four-arm PEG norbornene, and 10% (w/v) four-arm PEG thiol. All bioinks are sterilized prior to printing via 0.4 μm sterifilter and were fabricated in a

sterile tissue culture hood and treated with ethylene oxide for surface sterilization prior to implantation. Scaffolds are programmed to be printed with inner patterns (similar to those described in Chapter 3 previously: PEG Control 1:0, hybrid 1:1, hybrid 1:2, hybrid 1:3, GelMA control 0:1) under controlled conditions, including temperature, pressure, print speed, fiber spacing, and needle size.

Animal Surgery

Adult female Lewis rats (200g) were sedated for surgery in an induction chamber under 5% isoflurane and 2 L/min oxygen. Anesthetic was maintained with 2% isoflurane and 2 L/min oxygen through a nose cone for the duration of the procedure. Breathing rate was monitored, and the rats were placed on a water recirculating heating pad and distant heat lamp. For the dorsal implantation, the fur was clipped with electric shears. The exposed skin and surgical site were prepared with alternating iodophor antiseptic solution and 70% alcohol washes for 3 cycles, and further covered with sterile drapes. Using strict aseptic techniques, a 20 mm midline incision was created over the spine at the scapular level. The incision was deepened with blunt dissection, which allowed for the creation of a subcutaneous pocket. A second, shallow incision was made on the superficial cervical fascia- the primary subcutaneous connective tissue that lies between the dermis of the rat's skin and the deep dorsal fascia. The scaffolds were then placed within this pocket, and tacking sutures using 4-0 C-14 reverse cutting resorbable sutures closed the fascial pocket. This helped stabilize the nipple implant in position to ultimately enhance host cell migration into the scaffold. The first incision was further closed by subcuticular

suturing along the midline incision lines, using the same resorbable suture mentioned above. Wound sites were further cleaned with saline, and the animals were transferred to a recover cage (2 animals per cage) warmed with a heating lamp. General health and wound checkup were performed daily for 2 weeks, followed by weekly checkups until the end of the study (4 weeks). All animals exhibited exceptional pain recovery, active behavior, and healthy weight, and no implant exposure occurred.

Histological Analysis

The rats were euthanized 30 days after the implantation with 10% CO_2 chamber for 10 minutes. The animals were shaved and a dorsal midline incision was made. At this time, it was recorded that 2 of the 10 rats contained palpable exodus present under the wound. Both the scaffold implant and the surrounding subdermal pocket tissue were explanted and further fixed with a 4% paraformaldehyde solution for 12 hours at room temperature. After this fixation, the tissues were soaked in solutions containing a gradual increased concentration of sucrose (10% - 30% w/v) and embedded in OCT gel for cryosectioning.

Sample sections underwent Hematoxylin-Eosin (H&E) and Masson's trichrome staining per manufacturer's protocol. Histopathological features were scored in a blind fashion according to a semi-quantitative scoring system suggested in Annex E of International Standards of Organization (ISO 10993-6-2016, which takes into consideration the extent of fibrosis and capsule formation, the extent and nature of the

inflammatory reaction, and the presence of vascularization. Five blind scorers evaluated a total of 150 images with a modified ISO10994-6 protocol to tailor to the available microscope 20X capability.

The extent of fibrosis and neovascularization was further analyzed using a histomorphometric approach. The fibrotic capsule thickness was determined using the 'Freehand' tool in Image J to manually select the fibrotic tissue layer. The Measurements tool allowed 3 measurements to be obtained across the thickness of the fibrotic capsule. The measurement protocol foresaw taking 18 individual thickness measurements per implant analyzed. The independent measurements were then averaged to obtain the mean fibrotic capsule thickness. Neovascularization was also quantified per 20X images by counting the number of blood vessels present in each image. All the images were captured using 10X and 20X magnification by light microscopy (Nikon).

Statistical Analysis

The quantitative image results (Figures 5.3 and 5.5) were analyzed using a two-group Paired Comparison plot followed by Tukey's Multiple Comparison Test assuming normal data distribution with a confidence of 95% ($p<0.05$).

5.3 Results and Discussion

5.3.1 *In Vivo* Application of Hybrid 3D Printed Scaffolds

Proceeding sterile fabrication, five of each hybrid nipple-areola scaffold type were randomly implanted in the dorsal subcutaneous regions of Lewis rats (3 scaffolds per animal) to assess the local biological response to these hybrid materials (**Figure 5.1**A). The Lewis strain, an inbred type, was particularly used to minimize the differences in the initial subcutaneous tissue inflammation grade between each animal. All animals exhibited an exceptional pain recovery, active behavior, and healthy weight throughout the 4-week study, yet two of the ten animals displayed signs of local infection at the incision site with palpable exodus present. Since it is important to only report results from animals without wound complications, the results from one scaffold of each type was eliminated. Thus, a total of 20 scaffolds were processed, cryosectioned, and histologically stained with Hematoxylin & Eosin (H&E) and Masson's Trichrome (MT). Using a modified scoring system following the Standard ISO 10993-6: Biological Evaluation of Medical Devices - Tests for Local Effects After Implantation, the following criteria were considered for a semi-quantitative analysis of the tissue surrounding the implant: inflammatory infiltrate, phagocytosis, degradation of the implant, fatty infiltrate, neovascularization, and capsule characterization. Slight modifications were made to the ISO10994-6 to tailor the analysis to our nipple-areola scaffold and these changes are highlighted in **Table 5.1** below.

Inflammatory Infiltrate	
Presence of inflammatory cells not being macrophages/histiocytes, near implant mainly lymphocytes, plasma cells, and/or polymorphonuclear granulocytes	
Score	**Description**
0	No infiltrate present
1	Sparse inflammatory response, one or more small conglomerates of cells present, or a few single cells present
2	Mild inflammatory response, several small conglomerates of cells present, or single cells regularly present
3	Moderate inflammatory response, several large conglomerates of cells present
4	Dense inflammatory response, large confluent areas with inflammatory cells present

Phagocytosis	
Presence of macrophages and/or foreign body giant cells engulfing implant or cellular debris	
Score	**Description**
0	No phagocytotic cells present
1	Sparse phagocytosis, some cells present with phagocytized material
2	Mild phagocytosis, several cells and/or groups of cells with phagocytosis
3	Moderate phagocytosis, several groups of cells with phagocytosis and/or zone of phagocytic cells around implant
4	Dense phagocytosis, all material phagocytized either as large fragments or as small parts in individual macrophages

Necrosis	
Presence of cell death zones caused by tissue autolysis	
Score	**Description**
0	No necrosis present
1	Sparse necrosis, one or more small areas of increased cytoplasmic binding of eosinophilic dye
2	Mild necrosis, several small conglomerate areas of cell death
3	Moderate necrosis, several large conglomerate areas of cell death
4	Dense necrosis, large confluent areas of cell death

Neovascularization	
Microscopic blood vessels formed during the healing process of granulated tissue	
Score	**Description**
0	No neovascularization present
1	Mild neovascularization, some small capillaries present
2	Moderate neovascularization, larger artery(ies) or groups of capillaries present
3	Dense neovascularization, both larger arteries and accompanying small capillaries present

Capsule Characterization	
Fibrotic capsule developed during innate foreign body immune response	
Score	**Description**
0	No capsule present
1	Mild capsule of macrophages adjacent to implant and some (a few) fibrous cell layers
2	Moderate capsule composed of macrophages adjacent to implant and multiple/several layers of fibrous tissue (fibroblasts)
3	Dense capsule composed of three major sections: macrophages adjacent to implant, fibrous tissue and phagocytosing macrophages outside fibrous tissue

Fatty Infiltrate	
Presence of adipose tissue above/within the implant	
Score	**Description**
0	No adipose tissue present
1	Minimal amount of fat cells present in the area
2	Several layers of adipocytes present near the implant
3	Elongated and broad accumulation of adipocyte cells about the implant site
4	Extensive fat completely surrounding the implant

Degradation of Implant	
Fragmentation of implant *in situ*	
Score	**Description**
0	No visible degradation present
1	Sparse degradation of implant, some minor dissolution on edges, cracks in implant and/or small fragment present,
2	Mild degradation of implant with cracks in implant and/or some fragments, minor cellular infiltration
3	Moderate degradation of implant with presence of several fragments, clear cellular infiltration into the implant
4	Abundant degradation of implant with almost complete fragmentation

Table 5.1 Modifications to the ISO 10993-6 Standard. The cellular and tissue evaluation proposed by the *International Organization for Standardization* calls for the cell count of several inflammatory cells in each evaluated image (high powered 400X). Since the lowest magnification we were able to obtain was 20X, we tailored the analysis by redefining each score value, mimicking the terminology used in the ISO and included an additional section 'Degradation of Implant' to better describe how the host tissue is integrating with the degradable components of the hybrid scaffolds.

Five blind scorers evaluated a total of 120 H&E images, of which 6 images corresponded to the center section of each hybrid scaffold. For each sample, three of these images described the tissue response located at the implant-subcutaneous space interface, while the other three images described the tissue response at the implant-fascia interface (Figure 5.1B). Taken together, these six images per implant holistically represent the foreign body and vascular responses induced by the host. Figures 5.2 through 5.4 graphically depict the score averages in every evaluation per scaffold type, where each color (red, yellow, green, blue, and purple) represents the results from a single blind scorer and each violin curve (gray or pink) represents the

peak population incidence of each interface. Since an even spread can be seen between averaged score value and color, there was a clear agreement amongst the results and the methodology of scoring can be viewed as consistent. In general, there appeared to be a lower immune response from the underlying fascial tissues compared to those analyzed in the upper subcutaneous interface. This may be due to the imbalanced, yet natural, cellular presence in the matrix of each neighboring tissue type; the fascia is predominantly composed of extracellular matrix (tightly wound collagen and elastin fibrils) with little vasculature and few cellular constituents of mainly fibroblasts[223], while the subcutaneous pocket experiences a high influx of immune cells as it directly contacts the rat's skin. To serve its function as a protective barrier, the epidermis is highly composed of immune cells, such as Langerhans cells, neutrophils, mast cells, and dendritic cells, that defend against microbial pathogens, physical, or chemical threats to the host[224]. Therefore, the subcutaneous interface is more likely to experience a heightened foreign body response and thus receive higher scores due to the increased immune cell migration rate from the epidermal layer. Specific differences between fascial and subcutaneous scores are further discussed in the next section.

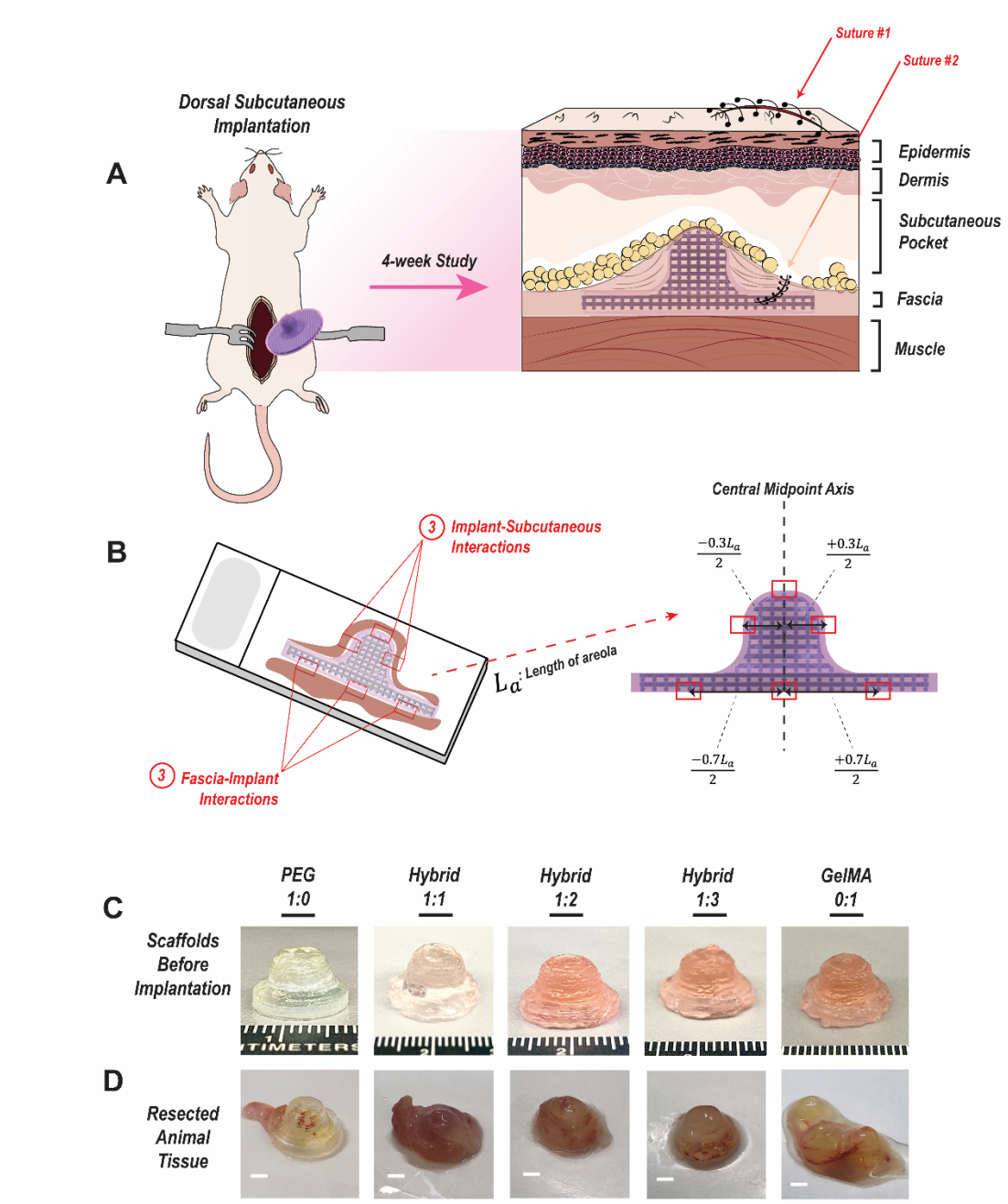

Figure 5.1 Animal Surgery and Method for Capturing Images. **A**. Three hybrid scaffolds were subcutaneously implanted in the dorsal lumbar region of each rat. Two incisions were made, the first was the initial 20 mm dorsal midline incision over the thoracolumbar area, and the second was through the superficial cervical fascia (a thin layer of subcutaneous connective tissue). This allowed the implant to be stabilized, as tacking sutures resisted significant movement of the implant. **B**. Six images were taken for each central section in every resected implant. We defined the location of each image by the length of the scaffold's areola to normalize this process and ensure that each implant interaction was holistically represented. C.

Representative images taken before implantation and D. after resection, where all samples appear to have maintained a nipple projection with minimal fibrotic capsule development. Scale bars represent 3 mm.

5.3.2 Cellular Characteristics of Surrounding Host Tissue

The score results recorded a range of mild to moderate cellular infiltration that was dependent on the implanted hybrid scaffold type. Inflammatory infiltrate referred to the cells that appeared to be either lymphocyte, plasma, or polymorphonuclear granulocyte-like in appearance, which were generally cells exhibiting a single and rounded and/or lobed nucleus with little cytoplasm. Phagocytosis referred to the macrophage-like cells, such as those with multiple nuclei (multinucleated giant cells) and a large cytoplasm loaded with particular debris. The infiltration of both cell groups was primarily observed in the implant-subcutaneous interface, as visualized by the higher peaks of the gray violin curves (**Figure 5.2**A and B). The presence of lymphocytes and polymorphonuclear neutrophilic granulocytes is frequently associated with the early acute inflammatory response to the surgical procedure, and unfortunately their role in the local reaction to the implant is not known[213]. However, they may be important for the ensuing macrophage response. The primary function of these macrophages is the phagocytosis and clearance of the degradable parts of the implant, which is reflected in the high macrophage presence in hybrid scaffolds 1:1, 1:2, 1:3, and GelMA controls. For non-degrading implants, such as the PEG control, phagocytosis is not possible and the implant becomes encapsulated, which is also reflected in both the H&E images shown in Figure 5.2 and the pink and gray violin curves in Figure 5.2D. Overall, across all hybrid scaffold types, phagocytosis remained the dominant characteristic of

the cellular response. Some groups have reported that the dominance in macrophage cell type is indicative of a chronic inflammatory response[225,226]; however, in biodegradable regenerative scaffolds this represents a positive result, as the macrophages play a critical role in the maintenance and resolution of inflammation[227] while the natural materials hydrolyze as host cells infiltrate the scaffold. The initial chronic inflammation can be most likely associated with the general wound healing process. Thus, their dominating presence ultimately exemplifies healing tissue.

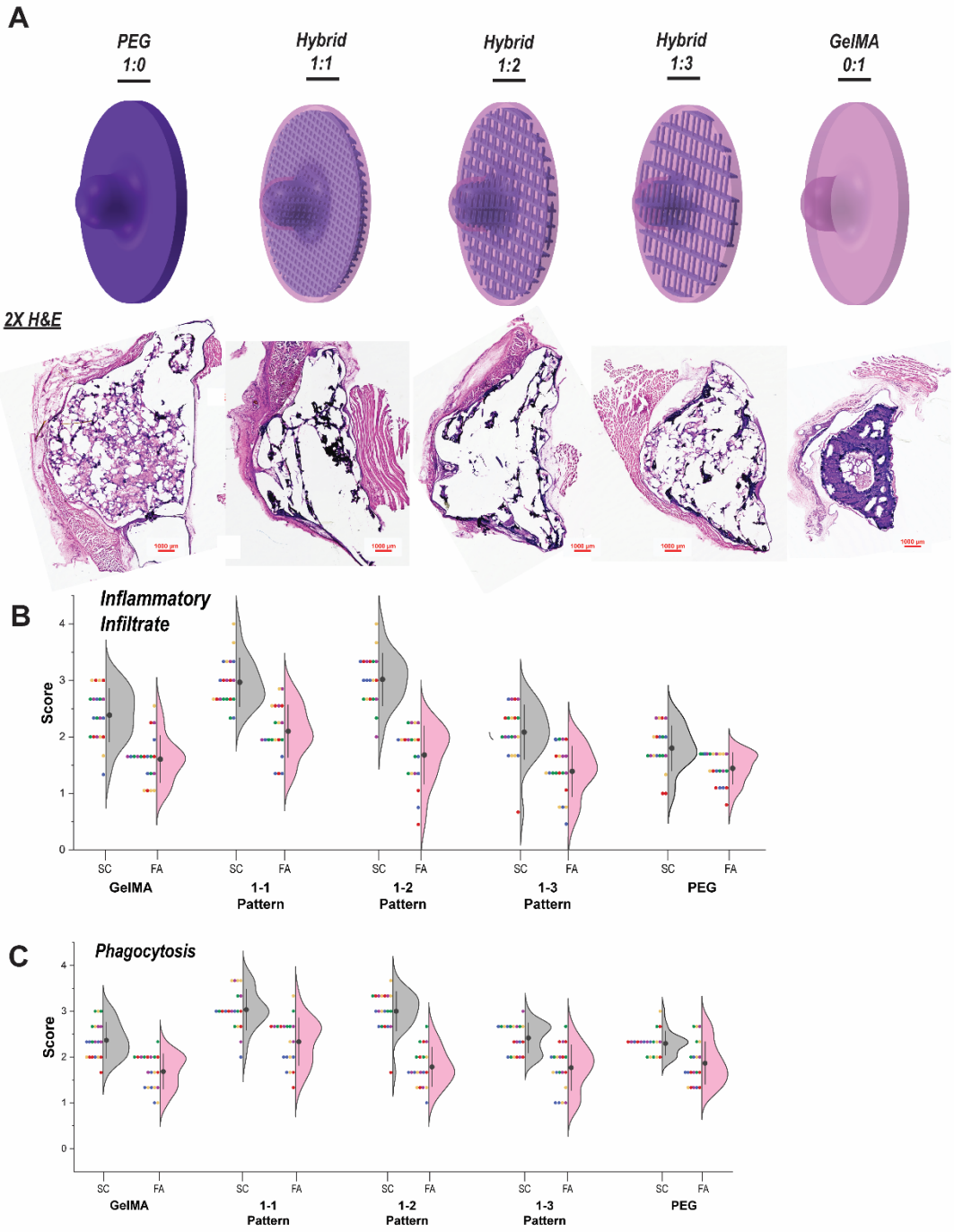
A
PEG
1:0
Hybrid
1:1
Hybrid
1:2
Hybrid
1:3
GelMA
0:1
2X H&E
B
Inflammatory
Infiltrate
Score
SC
FA
GelMA
1-1
Pattern
1-2
Pattern
1-3
Pattern
PEG
C
Phagocytosis

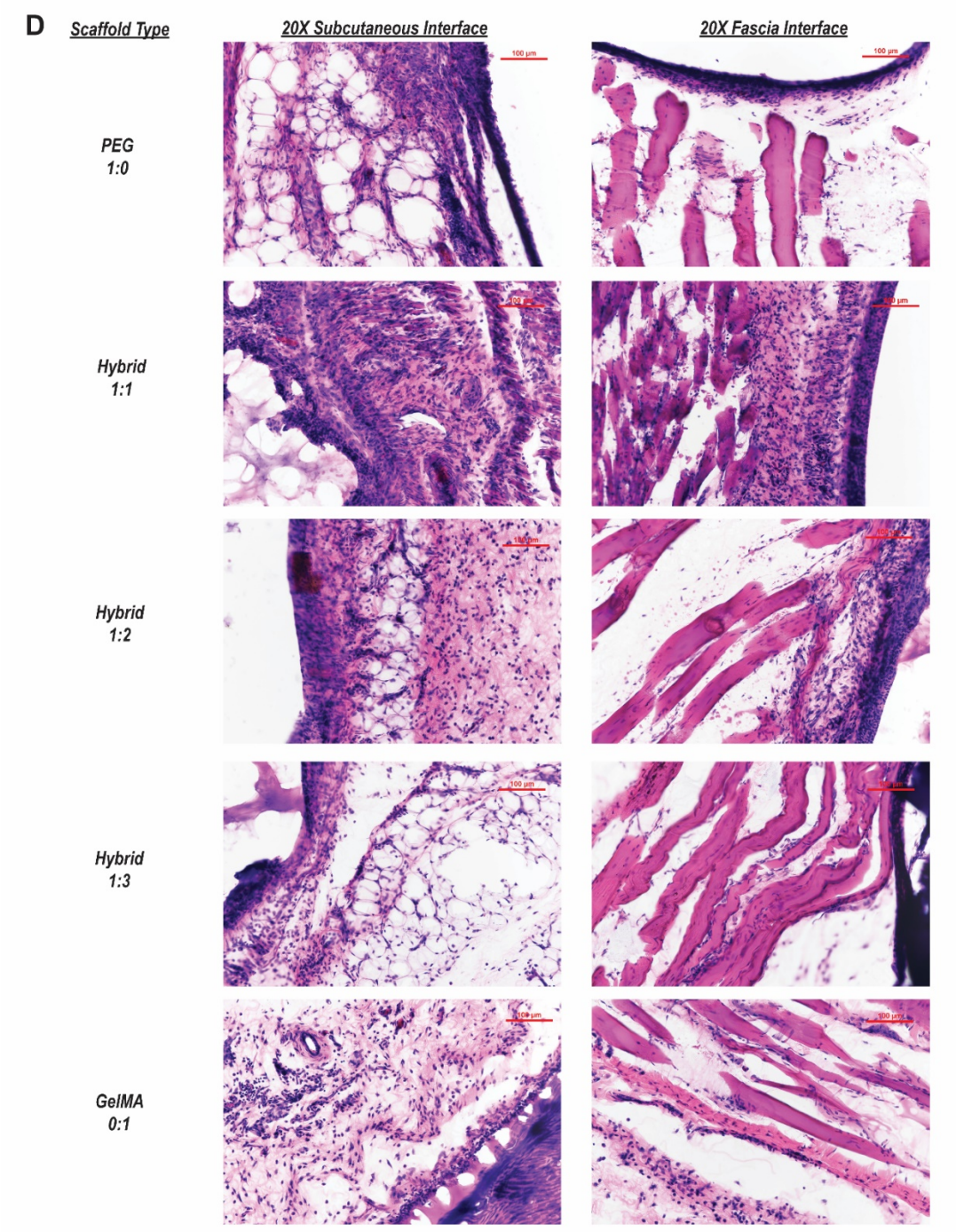

Figure 5.2 Cellular Characteristics. **A**. Representative H&E 2X images pertaining to each scaffold type display a prominent nipple projection. **B**. Semiquantitative scoring evaluations for inflammatory infiltrate (pertaining to lymphocytes, plasma cells, and polymorphonuclear granulocytes) were evaluated by five blind scorers. On the left, colored dots (red, yellow, green, blue, and purple) represent the average score results in every scaffold type evaluation. On the right, a violin curve (type: kernel density estimation) portrays the probability density function of the averaged scores and represents the peak population incidence of each interface (SC refers to the implant-

subcutaneous interface, while FA refers to the fascia-implant interface). Results show a lower inflammation of immune cells in FA than in SC interfaces, with minimal-moderate infiltrate present **C**. Phagocytosis refers to the presence of macrophages, and the results depicted here show a dominating macrophage presence over other inflammatory infiltrate. **D**. Representative H&E 20X images that portrayed the cellular characteristics in and around the scaffolds. Scale bars represent 100 μm.

5.3.3 Tissue Characteristics of Surrounding Host Tissue

As the cellular characteristic scores of the host response point towards the signs of a healthy recovery, the tissue characteristics of the surrounding host tissue also reveal a general acceptance of the implant. Intuitively, the implants containing the most GelMA experienced the highest degradation; score trends depict the GelMA control exhibited the most degradation, followed by the 1:3 pattern, 1:1 and 1:2 patterns with fairly equal amounts of degradation, and finally the PEG control exhibiting the least amount (**Figure 5.3**A). There appears to be a striking contrast in score trends between the subcutaneous and fascia interface within the GelMA implant test group, where the fascia-implant interface displayed a higher amount of degradation. One possible explanation for this finding would be that the fascia interface experiences a higher shear load along its boundary as the animal moves/walks, and this contraction of underlying muscle may cause mechanical friction that enhances the degradation rate of the implant. Degradation is favorable in regard to our implant, as its hybrid material makeup is designed to promote integration with the surrounding host tissue and thus lead to an interlocked placement for a stable nipple projection.

Additionally, neovascularization was recorded (Figure 5.3B) and is another positive trait that signifies the formation of granulation tissue. Granulation tissue is a young connective tissue that grows from the base of a wound and contains proliferative fibroblasts, delicate capillaries, and infiltrated inflammatory cells in a loose cellular matrix[228]. Its presence resembles a positive result, as its formation means that both inflammatory responses (acute and chronic) have subsided, and new, healthy tissue is beginning to form. Neovascularization is present in all the implant types tested, with GelMA controls, 1:1, and 1:2 scaffolds exhibiting the highest number of capillaries present. These results were later validated with quantitative measurements taken from the H&E images, by which the number of blood vessels within each image was recorded (Figure 5.3C).

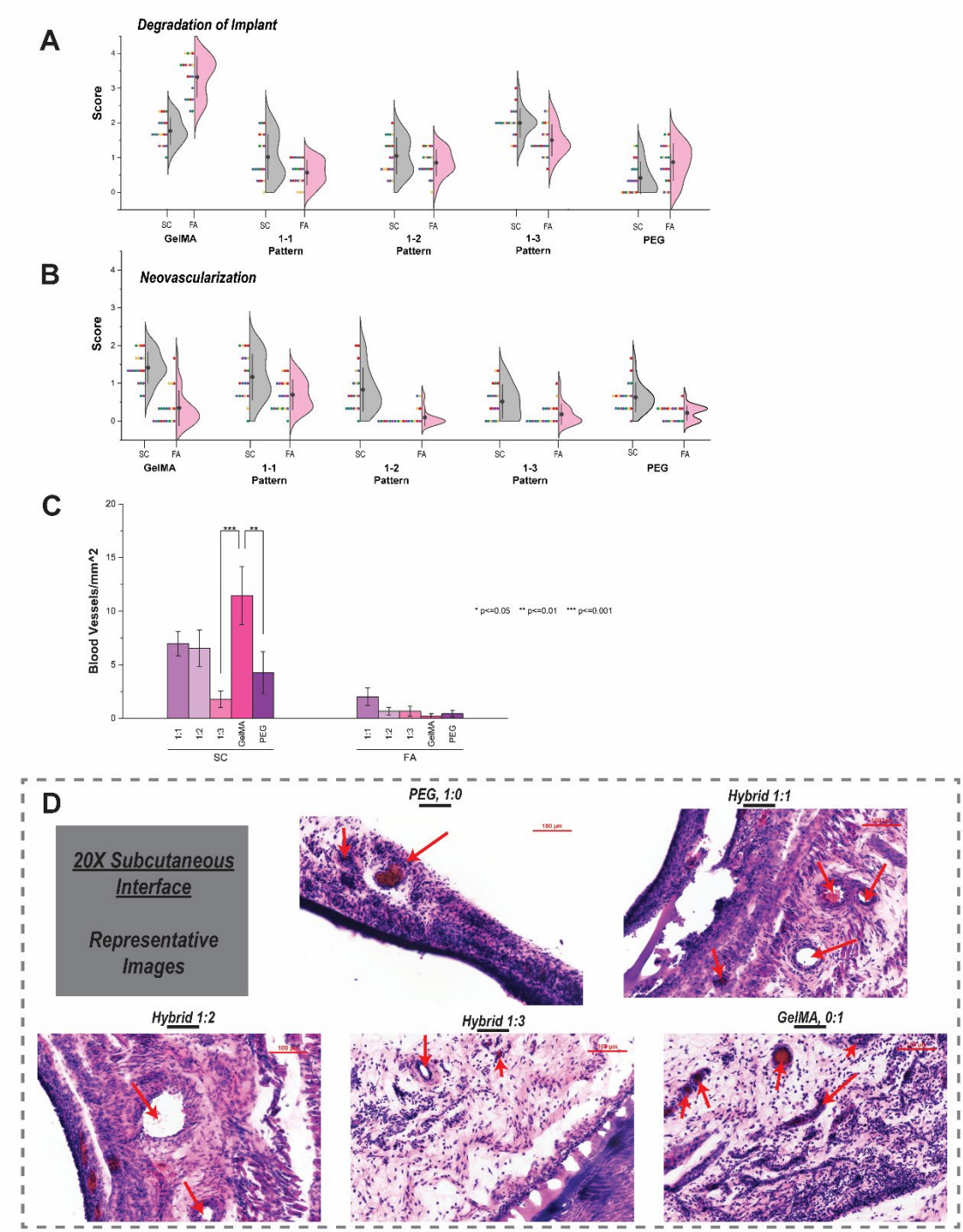

Figure 5.3: Tissue Characteristics 1, Degradation of Implant and Neovascularization of Surrounding Tissue. **A**. Degradation of the biodegradable GelMA is expected in patterns containing the highest amount of this biomaterial (i.e. 1:3 and GelMA 0:1 control), and the average score results reflect this prediction. A striking contrast exists between FA and SC interfaces, which may be due to the increased shear stress induced by the contraction of underlying fascial muscles. **B**. Neovascularization is present in all scaffold types tested, signifying that granulation

tissue is beginning to form. **C**. Blood vessels were counted in each 20X (n'=6 with n=4 biological samples) image and recorded to validate our previous blind score results. These quantitative image results display mean ± standard deviation and were analyzed using a two-group Paired Comparison plot followed by Tukey's Multiple Comparison Test assuming normal data distribution with a confidence of 95% (p<0.05). **D**. Representative H&E 20X images that display evidence of neovascularization in every scaffold type, where a red arrow points to the location of blood vessels and/or capillaries present at the tissue interface. Scale bars represent 100 μm.

Adipocyte proliferation is often stimulated as granulation tissue forms[229], which aligns with the variable amount of fatty infiltrate that was recorded among the hybrid implant types (**Figure 5.4**A). Large adipose vacuoles were visualized along the subcutaneous interface in hybrid patterns 1:1, 1:2, and 1:3. Remarkably, the PEG controls also experienced a mild infiltration of adipose tissue. This fatty infiltrate may have stemmed from the migration and proliferation of adipocytes derived from the hypodermis of the rat skin, and its presence could ultimately be beneficial in the implant's ability to match the natural tactile properties of nipple tissue.

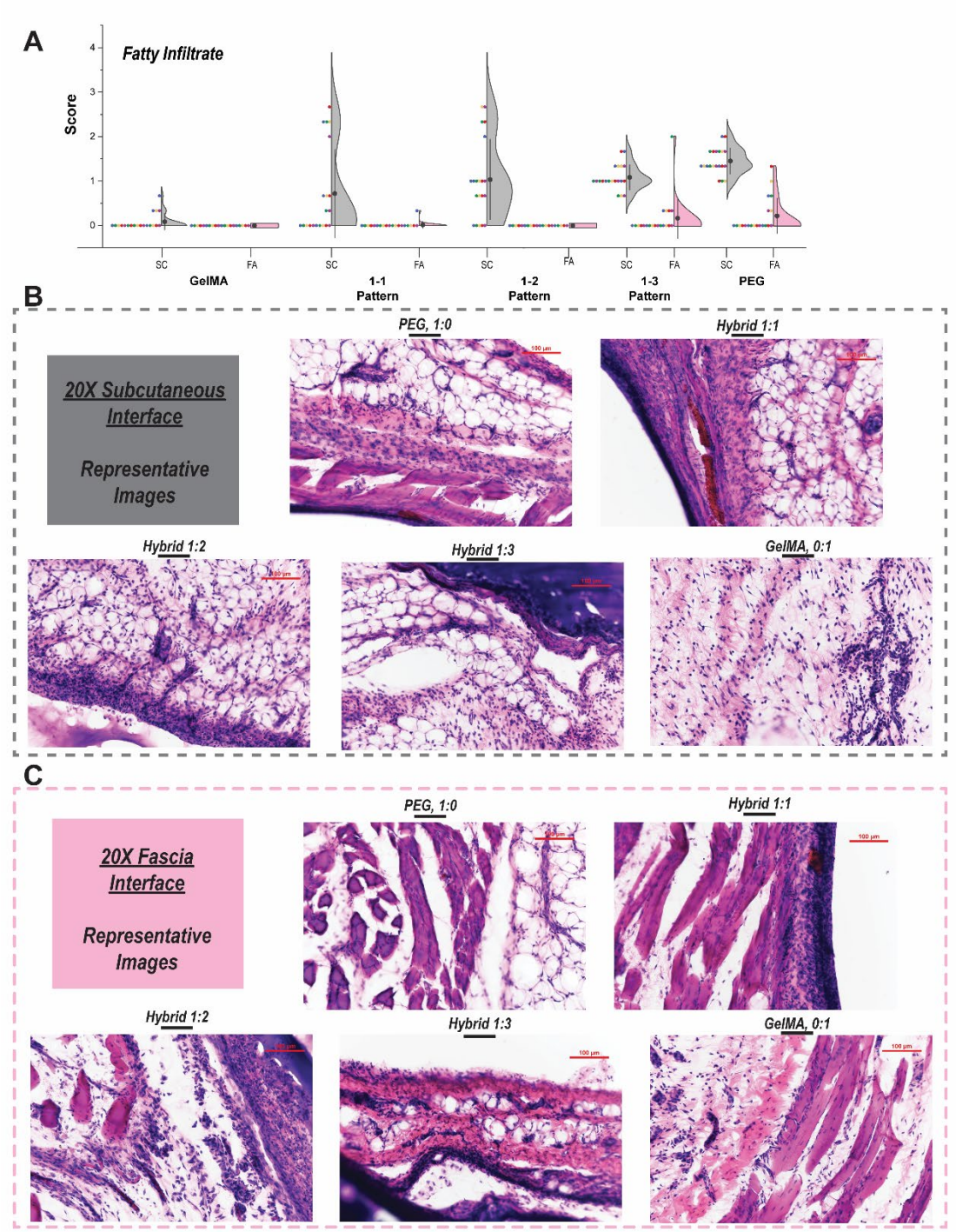

Figure 5.4: Tissue Characteristics 2, Presence of Fatty Infiltrate. A. The subcutaneous interface experiences a proliferation of adipose tissue, which can be visualized by the high peaks of the gray violin curves. Large adipose vacuoles can be visualized in representative H&E images depicted in **B** (images taken at the implant-subcutaneous interface) and **C** (images taken at the fascia-implant interface). Scale bars represent 100 µm.

The last and most promising recorded tissue characterization was the minimal capsule thickness surrounding each implant. Capsular contracture is a very common, painful, and detrimental complication that accompanies many soft tissue implants[230], especially those used in breast reconstruction. In fact, the overall incidence of capsular contracture of silicone breast implants is reported as high as 37% and increases up to 100% in studies with patients receiving post-mastectomy radiation therapy (PMRT)[231], requiring a further surgical procedure (capsulotomy or capsulectomy). Even with current design strategies of textured surface topologies[232], advanced surgical techniques, and supplemental steroids and antibiotics[233], capsular contraction still remains a significant threat to the patient's health. Our hybrid scaffolds exhibited an average fibrotic capsule score in a mild – moderate range in severity. As before, the implant-subcutaneous interface experienced a higher inflammation and thus foreign capsule response around the implant than the fascia-implant interface due to the migration of epidermal immune cells. Scaffolds with the highest GelMA component (1:3 hybrid, GelMA control) and PEG controls displayed trends in a mild fibrotic capsule formation (**Figure 5.5**). Hybrid scaffolds 1:1 and 1:2 appeared to have a more moderate capsule, where several layers of fibrous tissue were present. To validate the semiquantitative scoring results, sample sections were stained with MT and subsequent quantification of the fibrotic capsule was measured. The mean thickness of the capsules was larger at the subcutaneous interface (1:1 recorded the thickest measurement of 378.87 ± 108.45 micros) than the fascial interface (1:2 recorded the thickest measurement at 244.08 ± 35.63 microns), mirrored the semiquantitative scoring results (Figure 5.5A). The collagen fibers and

fibroblast layer were drastically reduced in the PEG control group (199.79 ± 94.63 μm at SC surface and 39.16 ± 8.97 μm at the FA interface) when compared to the 1:1 and 1:2 hybrid scaffolds. Outstandingly, the 1:3 hybrid scaffold experienced a minimal capsule encapsulation of 250.43 ± 62.74 μm at the SC interface and 128.89 ± 61.49 μm at the FA interface. Other groups have recorded fibrotic capsules up to 3 mm in thickness when synthetic materials have been implanted subcutaneously in a rat model[121]. This rigorous semiquantitative study confirms the effectiveness of these hybrid materials in subsiding significant acute and chronic inflammations and thus reducing the extent of the foreign body reaction.

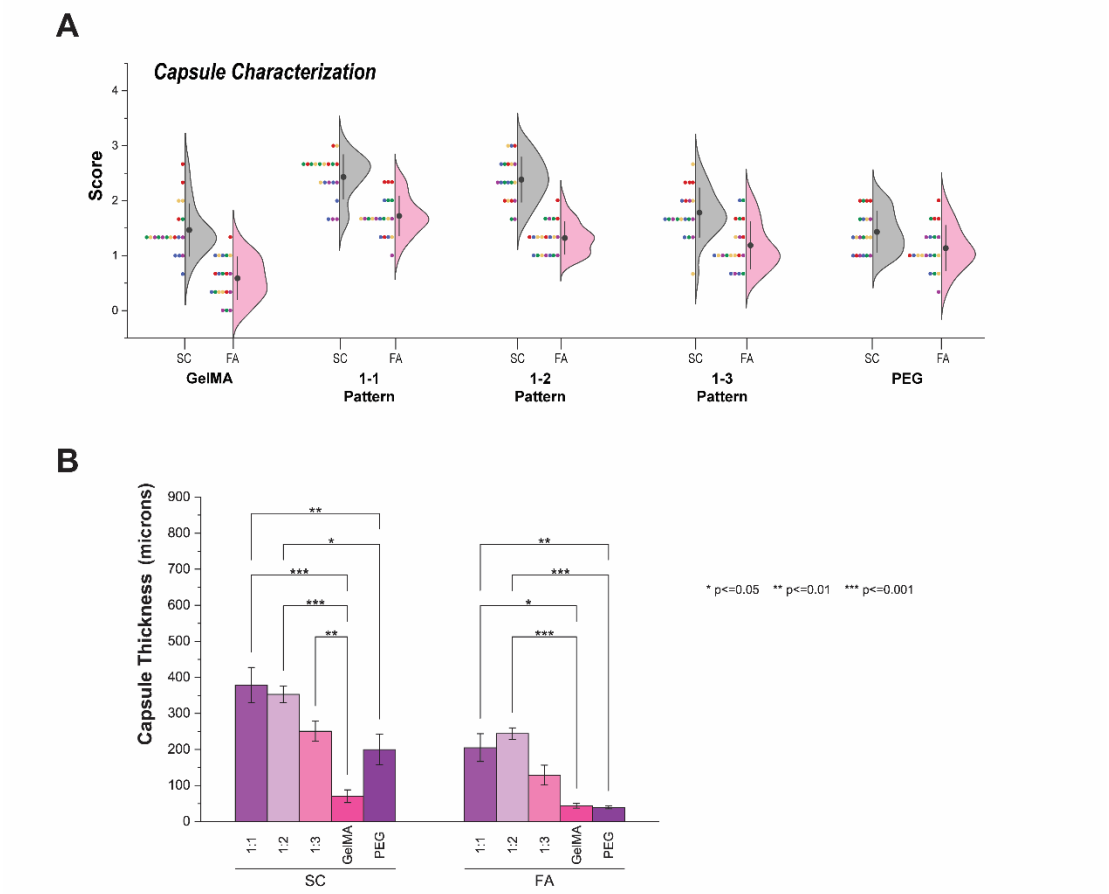

Figure 5.5: Tissue Characteristics 3, Capsule Characterization. A. With all foreign objects introduced to the body, a fibrotic capsule forms at the boundary of the implant and is composed of giant nucleated macrophage cells and surrounding fibroblasts. Scoring results show that the capsule exists in a mild-moderate thickness. This was further quantified in **B**, where each image was evaluated at 3 separate points (n'=6, n=3). These quantitative image results display mean ± standard deviation and were analyzed using a two-group Paired Comparison plot followed by Tukey's Multiple Comparison Test assuming normal data distribution with a confidence of 95% (p<0.05). **C**. Representative Masson Trichrome images for capsule quantitative assessment can be seen on the next page. Scale bars represent 100 µm.

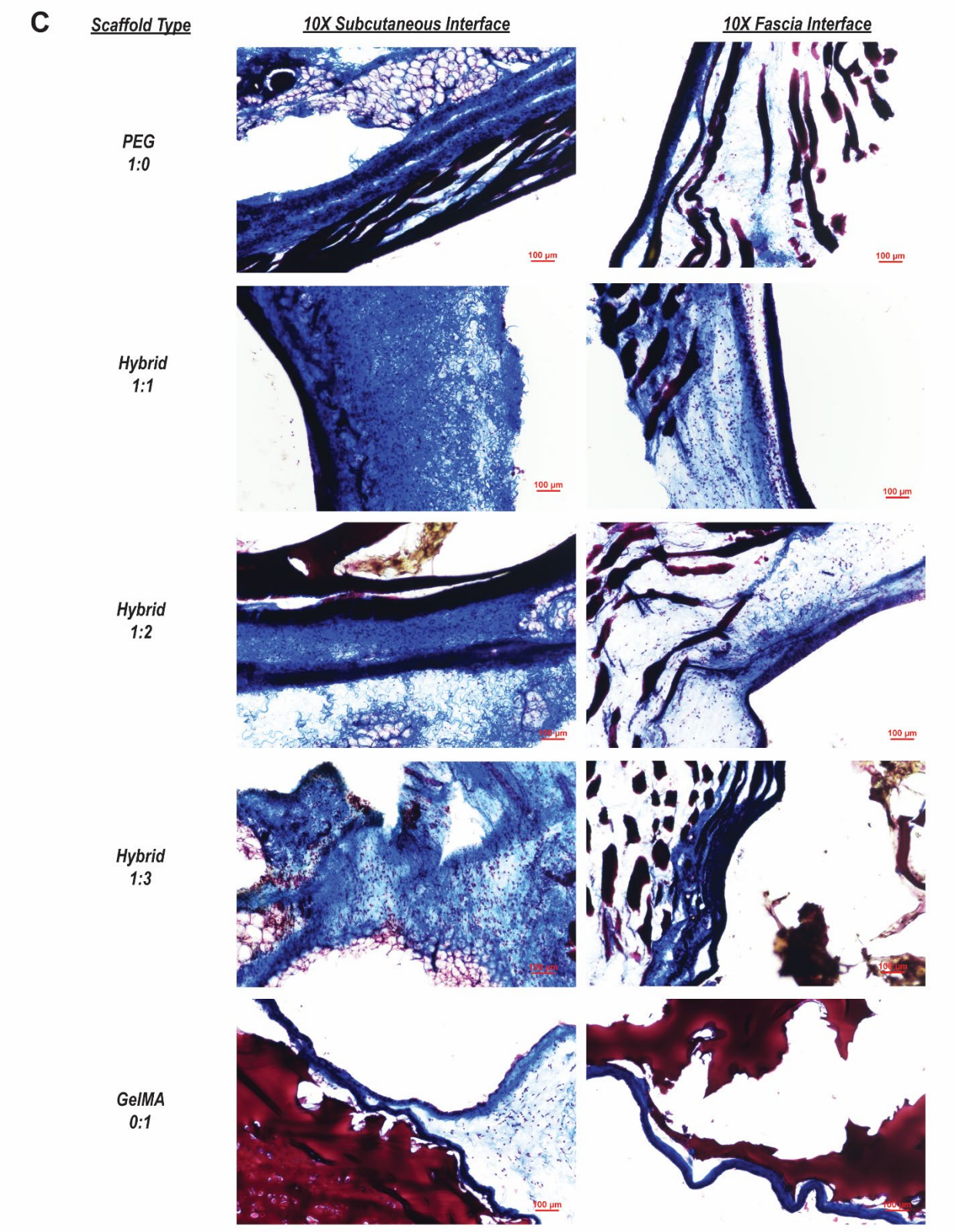
C
Scaffold Type
10X Subcutaneous Interface
10X Fascia Interface
PEG
1:0
Hybrid
1:1
Hybrid
1:2
Hybrid
1:3
GelMA
0:1
100 µm

5.5 Conclusion

Taken together, these results suggest that a hybrid nipple-areola acellular scaffold has great potential in reconstructing the nipple. The inflammatory reaction was mainly characterized by the presence of macrophages, with moderate neovascularization, variable amounts of fatty infiltration, high degradation, and minimal fibrotic capsule thickness. Given that the foreign body response is a multifactorial event cascade, and that we have only examined the process after 4 weeks, further studies are needed to evaluate the long-term success of the implant. In addition, our sterilization practice requires improvement, as there were wound-healing defects present at two incision sites. Strategies can be taken to prevent bacterial infection and to modulate implant rejection, such as anti-inflammatory cytokine release from the scaffold and immune cell recruitment and transplantation[219].

Chapter 6: Summary and Future Directions

6.1 Summary

In this dissertation, we combined the essence of conventional tissue engineering with a modern 3D printing platform to completely reimagine effective strategies for nipple reconstruction. As many groups have previously shown, the nipple-areola complex constitutes an important landmark on the breast and its loss due to breast cancer treatment can have devastating psychological effects on the patient. By replacing standard SFS techniques with a tissue engineered nipple-areola graft, the resulting nipple is designed to exhibit less flattening, provide an opportunity to regenerate part of the breast, and result in an appearance that more closely mimics the previous natural tissue. Extrusion 3D printing is an excellent fabrication technique to create custom shaped nipple-areola grafts per any breast size, as it has become an advantageous method that can incorporate digital information from CT scans directly into the final product.

The first objective of this work was to develop a hybrid printing platform that incorporated the strengths of natural and synthetic materials for the fabrication of soft tissue constructs. In Chapter 3, we developed a synthetic double-network ink composed of covalently crosslinked poly(ethylene glycol) and ionically crosslinked alginate capable of withstanding high compressive forces (>30kPa fracture strength, >1800 kPa toughness) with little adverse swelling effects. By coupling this ink with a

biodegradable gelatin methacrylate bioink in various print patterns, we were able to produce hybrid soft tissue constructs with moduli scaling a fourfold variation in stiffness – a range congruent to the stiffness values found in various compositions of soft tissue (skeletal muscle, 500 kPa, to adipose tissue, 10 kPa, compressive moduli values). Additionally, we defined a new shape analysis technique utilizing CloudCompare software to further assess the aesthetic properties of the printed scaffolds. With point cloud comparisons and quantitative measurements, a gradient in shape maintenance was found that was dependent on the print pattern used during scaffold fabrication. The conclusion of this aim resulted in the production of a biomimetic hydrogel graft consisting of both degradable and nondegradable parts that seamlessly coexist to promote tissue integration while maintaining its original printed structure.

In Chapter 4, we further tailored this hybrid printing strategy specifically to nipple tissue engineering. Methylcellulose was substituted for alginate, as its hydrophobic interactions produced a stable double network hydrogel more appropriate for *in vivo* implantation. We then demonstrated successful fabrication of physiologically sized nipple-areola constructs and found the mechanical properties of these hybrid scaffolds mirrored those of natural nipple tissue. Once the design of the bioprinted nipple was established, we wanted to determine the effect of the hybrid print pattern on internal cell viability and shape maintenance when human dermal fibroblasts were encapsulated in the GelMA bioink. When implanted *in vivo*, commercial products (such as AlloDerm) that are thick in size have been shown to fail because of

inadequate diffusion between the wound bed and autograft[38,93,94]. Additionally, dermal fibroblasts have been recorded to displace significant contractile forces on their substrate, and this behavior has resulted in the warping of many documented skin grafts[36,170]. We found that the majority of the tested print patterns produced a composite matrix that provided adequate diffusion to support cellular proliferation and exhibited minimal projection deformation when subjected to the highest level of cellular contractile forces. These results showcased the *in vitro* capacity of our hybrid scaffolds to provide accurate physical cues for nipple-areola reconstruction.

Our final investigation in Chapter 5 was focused on the integration of these hybrid prints with host tissue in a rat subcutaneous model. Five blind scorers evaluated the histological responses by utilizing a modified ISO 10993-6 Standard, meticulously assessing the cellular and tissue characteristics both in and around the implant. In most cases, a mild local foreign body reaction was observed, with minimal encapsulation and a moderate infiltration of inflammatory cells. The apparent formation of granulation tissue signified that both inflammatory responses (acute and chronic) had subsided in most implant types, and a new connective matrix with proliferative fibroblasts and delicate capillaries was beginning to form. Histomorphometric analysis also revealed moderate vascularization around the implant (5-10 blood vessels/mm^2) and an average 200-400μm in capsule thickness. These results are encouraging, as comparable studies have recorded an average thickness of 3 mm with limited presence of neovascularization.

In conclusion, the success of our *in vitro* and *in vivo* trials suggest that these hybrid nipple-areola complex scaffolds can provide a promising solution to nipple reconstruction. The acellular 3D printed scaffold contains a complementary matrix that can both recruit host dermal cells and withstand contractile forces, which can be used to better reproduce a well-integrated and stable nipple projection. The ability to scan the existing breast of the patient via computed tomography (CAT) and replicate the exact dimensions of that nipple-areola complex greatly appeals to nipple tissue reconstruction. In contrast to traditional fabrication methods (involving molds or solvents), 3D printing can easily create these unique grafts by incorporating their complex structure from the bottom-up in a layer-by-layer fashion. The customization and the regenerative potential of this strategy also prioritizes the emotional health of the mastectomy patient, enabling this implant to be viewed as a more appropriate nipple reconstruction technique for breast cancer survivors.

6.2 Future Directions

Even with the excitement and early success of this work, there are many hurdles to be addressed before this tissue engineering strategy reaches its eventual goal to aid thousands of breast cancer survivors. In addition to efficacy, scale-up potential, reliability, established regulatory routes, and societal acceptance issues, there are many technical challenges to overcome. Some of the major challenges are discussed in the next subsections.

6.2.1 Vascularization

Vascularization, the formation and growth of blood vessels, is a major engineering hurdle to overcome when creating artificial tissues, particularly large-scale 3D tissues. The internal formation of blood vessels is critical for the function and survival of cells because this integrated network provides effective transport of oxygen, nutrients, and removal of cell-secreted waste. Some groups have reported that it is particularly important for cells to be located within 250 μm of an oxygen source to thrive and function[234]. Therefore, to effectively develop a viable nipple projection, we must encourage the formation of vasculature with either physical or biochemical cues throughout the center of the implant. In preliminary studies, we have printed Pluronic (a sacrificial sucrose ink) that can further be washed away to produce intricate lumen strands with predefined structures (Figure 6.1). Human umbilical vein endothelial cells (HUVECs) can be directly introduced into these open channels to create progenitor vessels that can be further matured in a bioreactor. For an acellular approach, angiogenic factors, such as fibroblast growth factors (FGF) and vascular endothelial growth factors (VEGF) can be incorporated into the bioinks to stimulate host endothelial cell migration into these open vessels. Further studies would be needed to investigate how this internal printed architecture can integrate to

the host vasculature

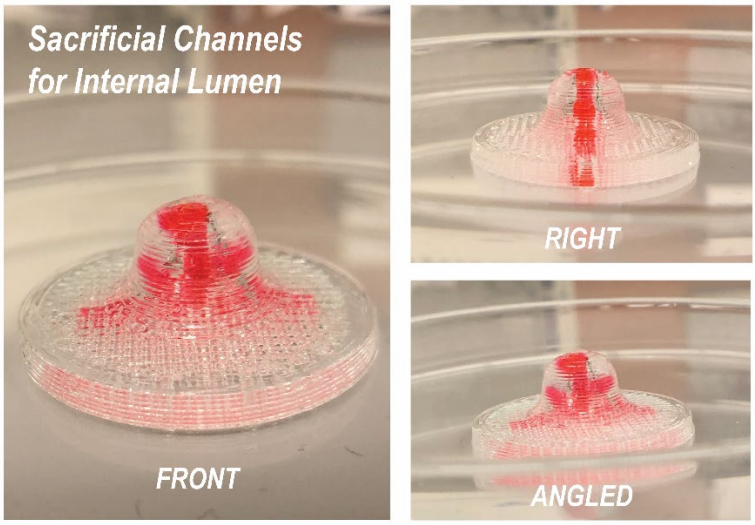

Figure 6.1: Sacrificial lumen-like channels to guide vascularization of nipple projection

6.2.2 Nipple-Areola Skin Graft

The vision for this implant is a viable nipple-areola skin graft, derived from the patient's skin cells, that can be directly sutured onto the breast to disrupt the central mastectomy scar prominence. The addition of dermal fibroblasts to the GelMA bioink and a topical application of epidermal keratinocytes could produce a viable skin substitute if matured prior to implantation. Due to the height of the 3D printed nipple projection (8mm), it could be difficult to cultivate *in vitro* due to a lack of diffusion within its elevated shape (>250 μm from the nearest nutrient source). To address this hurdle, we suggest that a bioreactor culture system is necessary to appropriately mature these grafts. Currently, we have made great progress towards this goal; we have developed an inverted bioreactor capable of effectively hydrating the dermal compartment of the graft with gravity-driven media diffusion while simultaneously exposing the outer epidermal cell layer to air (Figure 6.2). Air

exposure has been shown to be critical in the proper stratification of keratinocytes to produce an epidermal barrier[36], therefore submerging the grafts in media (per typical skin graft culture) would have negative impacts on the maturation of the nipple-areola skin graft. Preliminary studies have shown promising keratinocyte monolayer formation with positive cytokeratin 10 staining along with a viable nipple projection containing dermal fibroblasts, yet further studies are needed to visualize skin graft health over extended periods of *in vitro* culture.

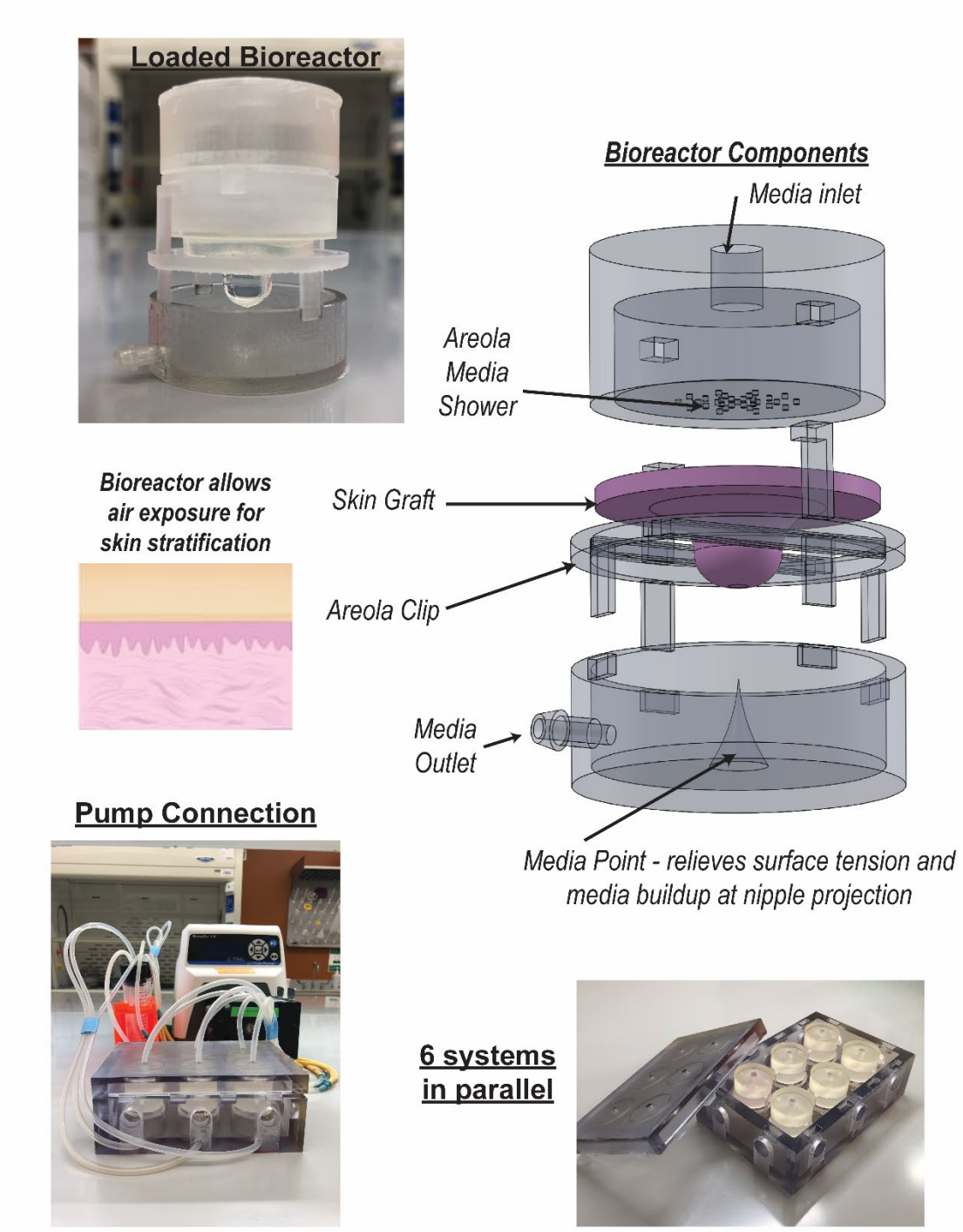

Figure 6.2: Inverted Bioreactor for Nipple-Areola Skin Graft

6.2.3 4D Bioprinting

One major drawback of 3D printing is that both the initial and final states of the fabricated object remain static. An inanimate, 3D printed nipple projection does not mimic the movements of the natural tissue; normally, smooth muscle erector pili cells line the base of the projection and can contract or elongate depending on the stimuli, resulting in a gradual projection or retraction of the nipple. Plastic surgeons have reported that some women prefer a nipple-areola tattoo over the SFS procedure because they dislike the constant 'stimulated' state of the reconstructed nipple[235,236]. Therefore, the incorporation of a 4th dimensional printing technique, where the 3D object is capable of changing its shape or functionality in respect to time, can enhance the design to be more dynamic with the host tissue. Existing 4D printed objects are mainly inspired by botanical systems (curling of tendrils, leaves, and flowers), primarily rely on physical stimuli, and are fabricated with temperature, pH, water, electric, magnetic, light, or acoustic-responsive materials[237–239]. However, I believe the most compelling potential of 4D printing will be the controlled movement of scaffold structures induced by stimulated cells (chemically, driven by ions or growth factors) to reshape or transform the state of the tissue scaffold. Below are snapshots of an animation that models a dynamic contraction/projection of a nipple, where a boundary contractile force is applied to the projection's base. This force is theoretically induced by matured smooth muscle cells that have been encapsulated (and printed) in the GelMA compartments of the scaffold (light pink regions). By creatively designing the synthetic backbone architecture (dark purple regions), we can create an implant that can be ionically triggered to project the nipple to a 'stimulated'

state. The development of a 4th dimensional printing technique that adds a responsive functionality to the printed nipple-areola skin graft can further enhance the implant's design and be one incredible scientific invention!

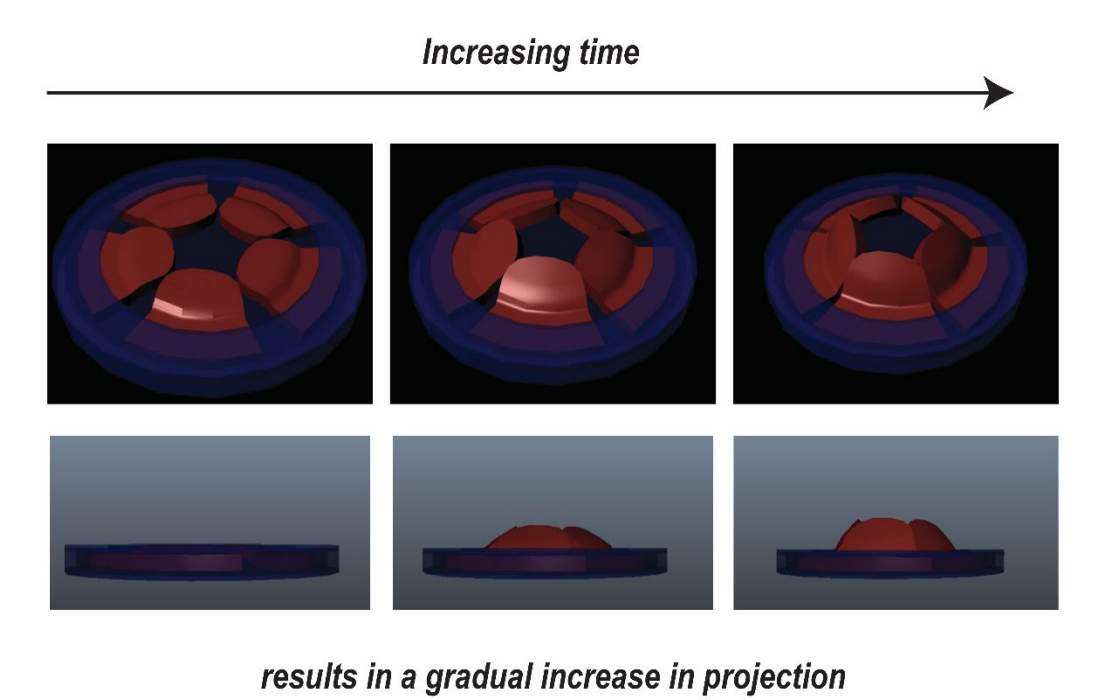

Figure 6.3: 4D Printing Application to the Nipple-Areola Scaffold

Bibliography

1. Siegel RL, Miller KD, Jemal A. Cancer statistics, 2020. *CA Cancer J Clin*. 2020;70(1):7-30. doi:10.3322/caac.21590

2. Weigelt B, Peterse JL, van't Veer LJ. Breast cancer metastasis: markers and models. *Nat Rev Cancer*. 2005;5(8):591-602. doi:10.1038/nrc1670

3. DeSantis CE, Ma J, Gaudet MM, et al. Breast cancer statistics, 2019. *CA Cancer J Clin*. 2019;69(6):438-451. doi:10.3322/caac.21583

4. Chew HK. Adjuvant therapy for breast cancer. *West J Med*. 2001;174(4):284-287.

5. Kayl AE, Meyers CA. Side-effects of chemotherapy and quality of life in ovarian and breast cancer patients. *Curr Opin Obstet Gynecol*. 2006;18(1):24–28. doi:10.1097/01.gco.0000192996.20040.24

6. Stavrou D, Weissman O, Polyniki A, et al. Quality of Life After Breast Cancer Surgery With or Without Reconstruction. *Eplasty*. 2009;9. Accessed October 4, 2020. https://www.ncbi.nlm.nih.gov/pmc/articles/PMC2691644/

7. Longman AJ, Braden CJ, Mishel MH. Side effects burden in women with breast cancer. *Cancer Pract*. 1996;4(5):274-280.

8. Palmer BV, Walsh GA, McKinna JA, Greening WP. Adjuvant chemotherapy for breast cancer: side effects and quality of life. *Br Med J*. 1980;281(6255):1594-1597. doi:10.1136/bmj.281.6255.1594

9. Shapiro CL, Recht A. Side Effects of Adjuvant Treatment of Breast Cancer. *N Engl J Med*. 2001;344(26):1997-2008. doi:10.1056/NEJM200106283442607

10. Street W. Breast Cancer Facts & Figures 2019-2020. :44.

11. Jonczyk MM, Jean J, Graham R, Chatterjee A. Surgical trends in breast cancer: a rise in novel operative treatment options over a 12 year analysis. *Breast Cancer Res Treat*. 2019;173(2):267-274. doi:10.1007/s10549-018-5018-1

12. Worni M, Akushevich I, Greenup R, et al. Trends in Treatment Patterns and Outcomes for Ductal Carcinoma in Situ. *JNCI J Natl Cancer Inst*. 2015;107(12). doi:10.1093/jnci/djv263

13. Sisti A, Grimaldi L, Tassinari J, et al. Nipple-areola complex reconstruction techniques: A literature review. *Eur J Surg Oncol EJSO*. 2016;42(4):441-465. doi:10.1016/j.ejso.2016.01.003

14. Kaidar-Person O, Kühn T, Poortmans P. Should we worry about residual disease after mastectomy? *Lancet Oncol*. 2020;21(8):1011-1013. doi:10.1016/S1470-2045(20)30331-4

15. Papassotiropoulos B, Güth U, Chiesa F, et al. Prospective Evaluation of Residual Breast Tissue After Skin- or Nipple-Sparing Mastectomy: Results of the SKINI-Trial. *Ann Surg Oncol*. 2019;26(5):1254-1262. doi:10.1245/s10434-019-07259-1

16. Cense HA, Rutgers EJTh, Lopes Cardozo M, Van Lanschot JJB. Nipple-sparing mastectomy in breast cancer: a viable option? *Eur J Surg Oncol EJSO*. 2001;27(6):521-526. doi:10.1053/ejso.2001.1130

17. Andersen JA, Pallesen RM. Spread to the nipple and areola in carcinoma of the breast. *Ann Surg*. 1979;189(3):367-372.

18. Quinn RH, Barlow JF. Involvement of the Nipple and Areola by Carcinoma of the Breast. *Arch Surg*. 1981;116(9):1139-1140. doi:10.1001/archsurg.1981.01380210023004

19. Tuttle TM, Habermann EB, Grund EH, Morris TJ, Virnig BA. Increasing Use of Contralateral Prophylactic Mastectomy for Breast Cancer Patients: A Trend Toward More Aggressive Surgical Treatment. *J Clin Oncol*. 2007;25(33):5203-5209. doi:10.1200/JCO.2007.12.3141

20. Wong SM, Freedman RA, Sagara Y, Aydogan F, Barry WT, Golshan M. Growing Use of Contralateral Prophylactic Mastectomy Despite no Improvement in Long-term Survival for Invasive Breast Cancer. *Ann Surg*. 2017;265(3):581-589. doi:10.1097/SLA.0000000000001698

21. Nash R, Goodman M, Lin CC, et al. State Variation in the Receipt of a Contralateral Prophylactic Mastectomy Among Women Who Received a Diagnosis of Invasive Unilateral Early-Stage Breast Cancer in the United States, 2004-2012. *JAMA Surg*. 2017;152(7):648. doi:10.1001/jamasurg.2017.0115

22. Collins LG, Nash R, Round T, Newman B. Perceptions of upper-body problems during recovery from breast cancer treatment. *Support Care Cancer*. 2004;12(2):106-113. doi:10.1007/s00520-003-0554-5

23. Courneya KS, Katzmarzyk PT, Bacon E. Physical activity and obesity in Canadian cancer survivors. *Cancer*. 2008;112(11):2475-2482. doi:10.1002/cncr.23455

24. Berger AM, Gerber LH, Mayer DK. Cancer-related fatigue. *Cancer*. 2012;118(S8):2261-2269. doi:10.1002/cncr.27475

25. Goodwin PJ, Ennis M, Pritchard KI, Trudeau M, Hood N. Risk of Menopause During the First Year After Breast Cancer Diagnosis. *J Clin Oncol*. 1999;17(8):2365-2365.

26. Wei D, Liu X-Y, Chen Y-Y, Zhou X, Hu H-P. Effectiveness of Physical, Psychological, Social, and Spiritual Intervention in Breast Cancer Survivors: An Integrative Review. *Asia-Pac J Oncol Nurs*. 2016;3(3):226-232. doi:10.4103/2347-5625.189813

27. Ho S-Y, Rohan KJ, Parent J, Tager FA, McKinley PS. A Longitudinal Study of Depression, Fatigue, and Sleep Disturbances as a Symptom Cluster in Women With Breast Cancer. *J Pain Symptom Manage*. 2015;49(4):707-715. doi:10.1016/j.jpainsymman.2014.09.009

28. Koopman C, Nouriani B, Erickson V, et al. Sleep Disturbances in Women With Metastatic Breast Cancer. *Breast J*. 2002;8(6):362-370. doi:10.1046/j.1524-4741.2002.08606.x

29. Kim M-S, Kim SY, Kim J-H, Park B, Choi HG. Depression in breast cancer patients who have undergone mastectomy: A national cohort study. *PLoS ONE*. 2017;12(4). doi:10.1371/journal.pone.0175395

30. Liao M-N, Chen P-L, Chen M-F, Chen S-C. Effect of supportive care on the anxiety of women with suspected breast cancer. *J Adv Nurs*. 2010;66(1):49-59. doi:10.1111/j.1365-2648.2009.05139.x

31. Cruickshank S, Kennedy C, Lockhart K, Dosser I, Dallas L. Specialist breast care nurses for supportive care of women with breast cancer. *Cochrane Database Syst Rev*. 2008;(1). doi:10.1002/14651858.CD005634.pub2

32. Jagsi R, Jiang J, Momoh AO, et al. Trends and Variation in Use of Breast Reconstruction in Patients With Breast Cancer Undergoing Mastectomy in the United States. *J Clin Oncol*. 2014;32(9):919-926. doi:10.1200/JCO.2013.52.2284

33. Harcourt D, Russell C, Hughes J, White P, Nduka C, Smith R. Patient satisfaction in relation to nipple reconstruction: The importance of information provision. *J Plast Reconstr Aesthet Surg*. 2011;64(4):494-499. doi:10.1016/j.bjps.2010.06.008

34. Nimboriboonporn A, Chuthapisith S. Nipple-areola complex reconstruction. *Gland Surg*. 2014;3(1):35-42. doi:10.3978/j.issn.2227-684X.2014.02.06

35. Pizzonia G, Sasso A, Rossello C. Alternative technique for nipple-areola complex reconstruction with poor skin condition. *ANZ J Surg*. 2017;87(10):E121-E124. doi:10.1111/ans.13176

36. Martin P. Wound Healing--Aiming for Perfect Skin Regeneration. *Science*. 1997;276(5309):75-81. doi:10.1126/science.276.5309.75

37. Zhong SP, Zhang YZ, Lim CT. Tissue scaffolds for skin wound healing and dermal reconstruction. *WIREs Nanomedicine Nanobiotechnology*. 2010;2(5):510-525. doi:10.1002/wnan.100

38. Garramone CE, Lam B. Use of AlloDerm in Primary Nipple Reconstruction to Improve Long-Term Nipple Projection. *Plast Reconstr Surg*. 2007;119(6):1663–1668. doi:10.1097/01.prs.0000258831.38615.80

39. Shestak KC, Gabriel A, Landecker A, Peters S, Shestak A, Kim J. Assessment of Long-Term Nipple Projection: A Comparison of Three Techniques. *Plast Reconstr Surg*. 2002;110(3):780–786. doi:10.1097/01.PRS.0000019716.27638.0D

40. Ss K, Gp R, Mj M, et al. Comparison of nipple projection with the modified double-opposing tab and star flaps. *Plast Reconstr Surg*. 1997;99(6):1602-1605. doi:10.1097/00006534-199705000-00020

41. Caterson SA, Singh M, Talbot SG, Eriksson E. Reconstruction of Areolar Projection Using a Purse-String Suture Technique. *Plast Reconstr Surg Glob Open*. 2015;3(7). doi:10.1097/GOX.0000000000000431

42. Hong KY, Kim Y-E, Minn KW, Jin US. Immediate Nipple Reconstruction During Implant-Based Breast Reconstruction. *Aesthetic Plast Surg*. 2017;41(4):793-799. doi:10.1007/s00266-017-0804-4

43. Cronin ED, Humphreys DH, Ruiz-Razura A. Nipple Reconstruction: The S Flap. *Plast Reconstr Surg*. 1988;81(5):783–787.

44. Narra K, Diaz LM, Papay FA. A New Approach to Nipple Reconstruction: The Modified S-Flap. *Plast Reconstr Surg*. 2008;122(2):89e. doi:10.1097/PRS.0b013e31817d65a1

45. Kim JH, Ahn HC. A Revision Restoring Projection after Nipple Reconstruction by Burying Four Triangular Dermal Flaps. *Arch Plast Surg*. 2016;43(4):339-343. doi:10.5999/aps.2016.43.4.339

46. Riccio CA, Zeiderman MR, Chowdhry S, Wilhelmi BJ. Review of Nipple Reconstruction Techniques and Introduction of V to Y Technique in a Bilateral Wise Pattern Mastectomy or Reduction Mammaplasty. *Eplasty*. 2015;15. Accessed October 3, 2020. https://www.ncbi.nlm.nih.gov/pmc/articles/PMC4392890/

47. Berson MI. Construction of pseudoareola. *Surgery*. 1946;20(6):808.

48. De Cholnoky T. Breast reconstruction after radical mastectomy: formation of missing nipple by everted navel. *Plast Reconstr Surg*. 1966;38(6):577-580. doi:10.1097/00006534-196638060-00016

49. DiPirro ME. Reconstruction of the nipple and areola after a burn. Case report. *Plast Reconstr Surg*. 1970;46(3):299-300. doi:10.1097/00006534-197009000-00018

50. Muruci A, Dantas JJ, Noguerira LR. Reconstruction of the nipple-areola complex. *Plast Reconstr Surg*. 1978;61(4):558-560. doi:10.1097/00006534-197804000-00010

51. Barton FE. Latissimus dermal-epidermal nipple reconstruction. *Plast Reconstr Surg*. 1982;70(2):234-237. doi:10.1097/00006534-198208000-00024

52. Little JW, Munasifi T, McCulloch DT. One-stage reconstruction of a projecting nipple: the quadrapod flap. *Plast Reconstr Surg*. 1983;71(1):126-133. doi:10.1097/00006534-198301000-00029

53. Silversmith PE. Nipple reconstruction by quadrapod flaps. *Plast Reconstr Surg*. 1983;72(3):422. doi:10.1097/00006534-198309000-00043

54. Hartrampf CR, Culbertson JH. A dermal-fat flap for nipple reconstruction. *Plast Reconstr Surg*. 1984;73(6):982-986. doi:10.1097/00006534-198406000-00027

55. Kon M. Latissimus dorsi three-flap nipple reconstruction. *Aesthetic Plast Surg*. 1984;8(4):243-245. doi:10.1007/BF01570711

56. Chang WH. Nipple reconstruction with a T flap. *Plast Reconstr Surg*. 1984;73(1):140-143. doi:10.1097/00006534-198401000-00035

57. Cohen IK, Ward JA, Chandrasekhar B. The pinwheel flap nipple and barrier areola graft reconstruction. *Plast Reconstr Surg*. 1986;77(6):995-999. doi:10.1097/00006534-198606000-00025

58. Zhong T, Antony A, Cordeiro P. Surgical outcomes and nipple projection using the modified skate flap for nipple-areolar reconstruction in a series of 422 implant reconstructions. *Ann Plast Surg*. 2009;62(5):591-595. doi:10.1097/SAP.0b013e31819fb1c9

59. Kroll SS, Hamilton S. Nipple reconstruction with the double-opposing-tab flap. *Plast Reconstr Surg*. 1989;84(3):520-525. doi:10.1097/00006534-198909000-00026

60. Ishii N, Ando J, Harao M, Takemae M, Kishi K. Influence of Flap Thickness on Nipple Projection After Nipple Reconstruction Using a Modified Star Flap. *Aesthetic Plast Surg*. 2018;42(4):964-970. doi:10.1007/s00266-018-1145-7

61. Brackley PTH, Iqbal A. Enhancing your C-V flap nipple reconstruction. *J Plast Reconstr Aesthetic Surg JPRAS*. 2009;62(1):128-130. doi:10.1016/j.bjps.2008.06.031

62. Teimourian B, Duda G. The propeller flap: a one-stage procedure for nipple-areola reconstruction. *Aesthetic Plast Surg*. 1994;18(1):81-84. doi:10.1007/BF00444253

63. Eng JS. Bell flap nipple reconstruction--a new wrinkle. *Ann Plast Surg*. 1996;36(5):485-488. doi:10.1097/00000637-199605000-00009

64. Thomas SV, Gellis MB, Pool R. Nipple reconstruction with a new local tissue flap. *Plast Reconstr Surg*. 1996;97(5):1053-1056. doi:10.1097/00006534-199604001-00027

65. Rubino C, Dessy LA, Posadinu A. A modified technique for nipple reconstruction: the "arrow flap." *Br J Plast Surg*. 2003;56(3):247-251. doi:10.1016/s0007-1226(03)00094-8

66. Gamboa-Bobadilla GM. Nipple reconstruction: the top hat technique. *Ann Plast Surg*. 2005;54(3):243-246.

67. Germanò D, De Biasio F, Piedimonte A, Parodi PC. Nipple reconstruction using the fleur-de-lis flap technique. *Aesthetic Plast Surg*. 2006;30(4):399-402. doi:10.1007/s00266-005-0199-5

68. Hammond DC, Khuthaila D, Kim J. The skate flap purse-string technique for nipple-areola complex reconstruction. *Plast Reconstr Surg*. 2007;120(2):399-406. doi:10.1097/01.prs.0000267337.08565.b3

69. Farace F, Bulla A, Puddu A, Rubino C. The arrow flap for nipple reconstruction: long term results. *J Plast Reconstr Aesthetic Surg JPRAS*. 2010;63(10):e756-757. doi:10.1016/j.bjps.2010.05.038

70. Van Laeken N, Genoway K. Nipple reconstruction using a two-step purse-string suture technique. *Can J Plast Surg J Can Chir Plast*. 2011;19(2):56-59.

71. Jamnadas-Khoda B, Thomas R, Heppell S. The "cigar roll" flap for nipple areola complex reconstruction: a novel technique. *J Plast Reconstr Aesthetic Surg JPRAS*. 2011;64(8):e218-220. doi:10.1016/j.bjps.2011.03.012

72. Karabagli Y, Kose AA, Mangir S, Cetin C. e-Flap nipple reconstruction in amputation mammaplasty. *Aesthetic Plast Surg*. 2012;36(5):1140-1143. doi:10.1007/s00266-012-9955-5

73. Elizabeth Clark S, Turton E. The CC-V Flap: A Novel Technique for Augmenting a C-V Nipple Reconstruction Using a Free Dermal Graft. *World J Plast Surg*. 2014;3(1):8-12.

74. Butz DR, Kim EK, Song DH. C-Y Trilobed Flap for Improved Nipple-Areola Complex Reconstruction. *Plast Reconstr Surg*. 2015;136(2):234-237. doi:10.1097/PRS.0000000000001408

75. Nano MT, Gill PG, Kollias J, Bochner MA, Malycha P, Winefield HR. Psychological impact and cosmetic outcome of surgical breast cancer strategies. *ANZ J Surg*. 2005;75(11):940-947. doi:10.1111/j.1445-2197.2005.03517.x

76. Lohsiriwat V, Petit J. Nipple Sparing Mastectomy: from prophylactic to therapeutic standard. *Gland Surg*. 2012;1(2):75-79. doi:10.3978/j.issn.2227-684X.2012.06.02

77. Al-Ghazal SK, Fallowfield L, Blamey RW. Comparison of psychological aspects and patient satisfaction following breast conserving surgery, simple mastectomy and breast reconstruction. *Eur J Cancer*. 2000;36(15):1938-1943. doi:10.1016/S0959-8049(00)00197-0

78. Didier F, Arnaboldi S, Gandini S, et al. Why do women accept to undergo a nipple sparing mastectomy or to reconstruct the nipple areola complex when nipple sparing mastectomy is not possible? *Breast Cancer Res Treat*. 2012;(132):1177-1184.

79. Stone K, Wheeler A. A Review of Anatomy, Physiology, and Benign Pathology of the Nipple. *Ann Surg Oncol*. 2015;22(10):3236-3240. doi:10.1245/s10434-015-4760-4

80. Heitland A, Markowicz M, Koellensperger E, Allen R, Pallua N. Long-term nipple shrinkage following augmentation by an autologous rib cartilage transplant in free DIEP-flaps. *J Plast Reconstr Aesthet Surg*. 2006;59(10):1063-1067. doi:10.1016/j.bjps.2005.02.021

81. Norton S, Akhavani MA, Kang N. The 'Hamburger' technique for harvesting cartilage grafts in nipple reconstruction. *J Plast Reconstr Aesthet Surg*. 2007;60(8):957-959. doi:10.1016/j.bjps.2005.11.047

82. collis N, Garrido A, Le Roux F. Maintenance of nipple projection using auricular cartilage. *Plastic and Reconstructive Surgery*. 2000;105(6):2276-2277.

83. Guerra A, Khoobehi K, Metzinger S, Allen R. New technique for nipple areola reconstruction: Arrow flap and rib cartilage graft for long-lasting nipple projection. *Annals of Plastic Surgery*. 2003;50(1):31-37.

84. Bernard RW, Beran SJ. Autologous Fat Graft in Nipple Reconstruction. *Plast Reconstr Surg*. 2003;112(4):964–968. doi:10.1097/01.PRS.0000076245.12249.BE

85. Yanaga H. Nipple-Areola Reconstruction with a Dermal-Fat Flap:: Technical Improvement from Rolled Auricular Cartilage to Artificial Bone. *Plast Reconstr Surg*. 2003;112(7):1863–1869. doi:10.1097/01.PRS.0000091243.42112.32

86. Zenn MR, Garofalo JA. Unilateral Nipple Reconstruction with Nipple Sharing: Time for a Second Look. *Plast Reconstr Surg*. 2009;123(6):1648–1653. doi:10.1097/PRS.0b013e3181a3f2f9

87. Adams WM. Free transplantation of the nipples and areolae. *Surgery*. 1944;15(1):186-195. doi:10.5555/uri:pii:S0039606044900589

88. Millard RD. NIPPLE AND AREOLA RECONSTRUCTION BY SPLIT-SKIN GRAFT FROM THE NORMAL SIDE. *Plastic and Reconstructive Surgery*. 1972;50(4):350-353.

89. Nipple contouring with hyaluronics postmastectomy. - Abstract - Europe PMC. Accessed October 5, 2020. https://europepmc-org.proxy-um.researchport.umd.edu/article/med/17966181

90. Panettiere P, Marchetti L, Accorsi D. Filler injection enhances the projection of the reconstructed nipple: An original easy technique. *Aesth Plast Surg*. 2005;29:287-294. doi:10.1007/s00266-004-0145-y

91. Holbrook A, Lee S, Soo MS. Mammographic appearance of calcium hydroxylapatite (RadiesseTM) injected into the breast for nipple reconstruction. *The Breast Journal*. 2012;19(1):104-113. doi:10.1111/tbj.12068

92. Evans KK, Rasko Y, Lenert J, Olding M. The Use of Calcium Hydroxylapatite for Nipple Projection After Failed Nipple-Areolar Reconstruction: Early Results. *Ann Plast Surg*. 2005;55(1):25–29. doi:10.1097/01.sap.0000168370.81333.97

93. Nahabedian MY. Secondary Nipple Reconstruction Using Local Flaps and AlloDerm. *Plast Reconstr Surg*. 2005;115(7):2056–2061. doi:10.1097/01.PRS.0000164490.99581.F9

94. Jansen LA, Macadam SA. The Use of AlloDerm in Postmastectomy Alloplastic Breast Reconstruction: Part II. A Cost Analysis. *Plast Reconstr Surg*. 2011;127(6):2245–2254. doi:10.1097/PRS.0b013e3182131c6b

95. Pashos NC, Scarritt ME, Eagle ZR, Gimble JM, Chaffin AE, Bunnell BA. Characterization of an Acellular Scaffold for a Tissue Engineering Approach to the Nipple-Areolar Complex Reconstruction. *Cells Tissues Organs*. 2017;203(3):183-193. doi:10.1159/000455070

96. Jankau J, Jaśkiewicz J, Ankiewicz A. A new method for using a silicone rod for permanent nipple projection after breast reconstruction procedures. *The Breast*. 2011;20(2):124-128. doi:10.1016/j.breast.2010.10.001

97. Handel N. Long-Term Safety and Efficacy of Polyurethane Foam-Covered Breast Implants. *Aesthet Surg J*. 2006;26(3):265-274. doi:10.1016/j.asj.2006.04.001

98. Ullmann Y, Peled IJ, Laufer D, Blumenfeld I. Nipple-areola reconstruction with a custom-made silicone ectoprosthesis. *Ann Plast Surg*. 1992;28(5):485-487. doi:10.1097/00000637-199205000-00015

99. Clarkson DJ, Smith PM, Thorpe RJ, Daly JC. The use of custom-made external nipple-areolar prostheses following breast cancer reconstruction. *J Plast Reconstr Aesthetic Surg JPRAS*. 2011;64(4):e103-105. doi:10.1016/j.bjps.2010.12.016

100. Sainsbury R, Walker VA, Smith PM. An improved nipple prosthesis. *Ann R Coll Surg Engl*. 1991;73(2):67-69.

101. Roberts AC, Coleman DJ, Sharpe DT. Custom-made nipple-areola prostheses in breast reconstruction. *Br J Plast Surg*. 1988;41(6):586-587. doi:10.1016/0007-1226(88)90165-8

102. Farhadi J, Maksvytyte GK, Schaefer DJ, Pierer G, Scheufler O. Reconstruction of the nipple-areola complex: an update. *J Plast Reconstr Aesthet Surg*. 2006;59(1):40-53. doi:10.1016/j.bjps.2005.08.006

103. Brent B, Bostwick JI. NIPPLE-AREOLA RECONSTRUCTION WITH AURICULAR TISSUES. *Plast Reconstr Surg*. 1977;60(3):353–361.

104. Sˇmahel J. Experimental implantation of adipose tissue fragments. *Br J Plast Surg*. 1989;42(2):207-211. doi:10.1016/0007-1226(89)90205-1

105. Oliver JD, Beal C, Hu MS, Sinno S, Hammoudeh ZS. Allogeneic and Alloplastic Augmentation Grafts in Nipple–Areola Complex Reconstruction: A Systematic Review and Pooled Outcomes Analysis of Complications and Aesthetic Outcomes. *Aesthetic Plast Surg*. 2020;44(2):308-314. doi:10.1007/s00266-019-01539-7

106. Nishiyama T, Nakajima T, Yoshimura Y, Nakanishi Y. Utilising solid models for preoperative shaping of HAP-TCP ceramic bone substitute: application for craniomaxillofacial surgery. *Eur J Plast Surg*. 1994;17(4):173-177. doi:10.1007/BF00188555

107. Wong RK, Wichterman L, Parson SD. Skin Sparing Nipple Reconstruction With Polytetrafluoroethylene Implant. *Ann Plast Surg*. 2008;61(3):256–258. doi:10.1097/SAP.0b013e31815d5bfa

108. BioAesthetics Surpasses Series A Goal Further Advancing the Nipple-Areolar Complex Graft to Clinical Use. Published October 1, 2020. Accessed October 5, 2020. https://www.businesswire.com/news/home/20201001006110/en/BioAesthetics-Surpasses-Series-A-Goal-Further-Advancing-the-Nipple-Areolar-Complex-Graft-to-Clinical-Use

109. Choe Jong M., Bell Thomas. Genetic material is present in cadaveric dermis and cadaveric fascia lata. *J Urol*. 2001;166(1):122-124. doi:10.1016/S0022-5347(05)66090-9

110. Derwin KA, Baker AR, Spragg RK, Leigh DR, Iannotti JP. Commercial Extracellular Matrix Scaffolds for Rotator Cuff Tendon Repair: Biomechanical, Biochemical, and Cellular Properties. *JBJS*. 2006;88(12):2665–2672. doi:10.2106/JBJS.E.01307

111. Humphrey J.D. Review Paper: Continuum biomechanics of soft biological tissues. *Proc R Soc Lond Ser Math Phys Eng Sci*. 2003;459(2029):3-46. doi:10.1098/rspa.2002.1060

112. Eto H, Kato H, Suga H, et al. The Fate of Adipocytes after Nonvascularized Fat Grafting: Evidence of Early Death and Replacement of Adipocytes. *Plast Reconstr Surg*. 2012;129(5):1081-1092. doi:10.1097/PRS.0b013e31824a2b19

113. Van Nieuwenhove I, Tytgat L, Ryx M, et al. Soft tissue fillers for adipose tissue regeneration: From hydrogel development toward clinical applications. *Acta Biomater*. 2017;63:37-49. doi:10.1016/j.actbio.2017.09.026

114. Monfort A, Izeta A. Strategies for Human Adipose Tissue Repair and Regeneration. *J Cosmet Dermatol Sci Appl*. 2012;2(2):93-107. doi:10.4236/jcdsa.2012.222021

115. Mahoney CM, Imbarlina C, Yates CC, Marra KG. Current Therapeutic Strategies for Adipose Tissue Defects/Repair Using Engineered Biomaterials and Biomolecule Formulations. *Front Pharmacol*. 2018;9:507. doi:10.3389/fphar.2018.00507

116. Upadhyaya SN, Bernard SL, Grobmyer SR, Yanda C, Tu C, Valente SA. Outcomes of Autologous Fat Grafting in Mastectomy Patients Following Breast Reconstruction. *Ann Surg Oncol*. 2018;25(10):3052-3056. doi:10.1245/s10434-018-6597-0

117. Bashir M, Sohail M, Bashir A, et al. Outcome of Conventional Adipose Tissue Grafting for Contour Deformities of Face and Role of Ex Vivo Expanded Adipose Tissue-Derived Stem Cells in Treatment of Such Deformities. *J Craniofac Surg*. 2018;29(5):1143-1147. doi:10.1097/SCS.0000000000004367

118. Lin DJ, Wong TT, Ciavarra GA, Kazam JK. Adventures and Misadventures in Plastic Surgery and Soft-Tissue Implants. *RadioGraphics*. 2017;37(7):2145-2163. doi:10.1148/rg.2017170090

119. Ramsubeik K, Tolaymat O, Kaeley G. Silicone-Induced Foreign Body Reaction: An Unusual Differential Diagnosis of Posterolateral Hip Pain. *Case Rep Med*. 2018;2018:1-3. doi:10.1155/2018/1802794

120. Rita M K, Ger JM P. Explantation of Silicone Breast Implants Ameliorates Gel Bleed Related Health Complaints in Women with Breast Implant Illness. *Clin Med Rev Case Rep*. 2020;7(3). doi:10.23937/2378-3656/1410301

121. Eltze E, Bettendorf O, Rody A, et al. Influence of local complications on capsule formation around model implants in a rat model. *J Biomed Mater Res A*. 2003;64A(1):12-19. doi:10.1002/jbm.a.10342

122. Fenske NA, Vasey FB. Silicone-Associated Connective-Tissue Disease: The Debate Rages. *Arch Dermatol*. 1993;129(1):97-98. doi:10.1001/archderm.1993.01680220109024

123. Bar-Meir E, Eherenfeld M, Shoenfeld Y. ReviewSilicone Gel Breast Implants and Connective Tissue Disease—A Comprehensive Review. *Autoimmunity*. 2003;36(4):193-197. doi:10.1080/08916931000148818

124. O'Brien FJ. Biomaterials & scaffolds for tissue engineering. *Mater Today*. 2011;14(3):88-95. doi:10.1016/S1369-7021(11)70058-X

125. Doyle AD, Carvajal N, Jin A, Matsumoto K, Yamada KM. Local 3D matrix microenvironment regulates cell migration through spatiotemporal dynamics of contractility-dependent adhesions. *Nat Commun*. 2015;6(1):8720. doi:10.1038/ncomms9720

126. Janik H, Marzec M. A review: Fabrication of porous polyurethane scaffolds. *Mater Sci Eng C*. 2015;48:586-591. doi:10.1016/j.msec.2014.12.037

127. Yang S, Leong K-F, Du Z, Chua C-K. The Design of Scaffolds for Use in Tissue Engineering. Part I. Traditional Factors. *Tissue Eng*. 2001;7(6):679-689. doi:10.1089/107632701753337645

128. Shastri VP, Martin I, Langer R. Macroporous polymer foams by hydrocarbon templating. *Proc Natl Acad Sci U S A*. 2000;97(5):1970-1975. doi:10.1073/PNAS.97.5.1970

129. Pandolfi V, Pereira U, Dufresne M, Legallais C. Alginate-Based Cell Microencapsulation for Tissue Engineering and Regenerative Medicine. *Curr Pharm Des*. 2017;23(26):3833-3844. doi:10.2174/1381612823666170609084016

130. Shin H, Quinten Ruhé P, Mikos AG, Jansen JA. In vivo bone and soft tissue response to injectable, biodegradable oligo(poly(ethylene glycol) fumarate) hydrogels. *Biomaterials*. 2003;24(19):3201-3211. doi:10.1016/S0142-9612(03)00168-6

131. Alexander A, Ajazuddin, Khan J, Saraf S, Saraf S. Polyethylene glycol (PEG)–Poly(N-isopropylacrylamide) (PNIPAAm) based thermosensitive

injectable hydrogels for biomedical applications. *Eur J Pharm Biopharm*. 2014;88(3):575-585. doi:10.1016/j.ejpb.2014.07.005

132. Holloway JL, Spiller KL, Lowman AM, Palmese GR. Analysis of the in vitro swelling behavior of poly(vinyl alcohol) hydrogels in osmotic pressure solution for soft tissue replacement. *Acta Biomater*. 2011;7(6):2477-2482. doi:10.1016/j.actbio.2011.02.016

133. Refojo MF, Leong F-L. Poly(methyl acrylate-co-hydroxyethyl acrylate) hydrogel implant material of strength and softness. *J Biomed Mater Res*. 1981;15(4):497-509. doi:10.1002/jbm.820150406

134. Santoro M, Tatara AM, Mikos AG. Gelatin carriers for drug and cell delivery in tissue engineering. *J Control Release Off J Control Release Soc*. 2014;190:210-218. doi:10.1016/j.jconrel.2014.04.014

135. Wang D, Liu H, Fan Y. Silk fibroin for vascular regeneration. *Microsc Res Tech*. 2017;80(3):280-290. doi:10.1002/jemt.22532

136. Sack BS, Mauney JR, Estrada CR. Silk Fibroin Scaffolds for Urologic Tissue Engineering. *Curr Urol Rep*. 2016;17(2):16. doi:10.1007/s11934-015-0567-x

137. de la Puente P, Ludeña D. Cell culture in autologous fibrin scaffolds for applications in tissue engineering. *Exp Cell Res*. 2014;322(1):1-11. doi:10.1016/j.yexcr.2013.12.017

138. Briganti E, Spiller D, Mirtelli C, et al. A composite fibrin-based scaffold for controlled delivery of bioactive pro-angiogenetic growth factors. *J Controlled Release*. 2010;142(1):14-21. doi:10.1016/j.jconrel.2009.09.029

139. Miron RJ, Fujioka-Kobayashi M, Bishara M, Zhang Y, Hernandez M, Choukroun J. Platelet-Rich Fibrin and Soft Tissue Wound Healing: A Systematic Review. *Tissue Eng Part B Rev*. 2017;23(1):83-99. doi:10.1089/ten.TEB.2016.0233

140. Noori A, Ashrafi SJ, Vaez-Ghaemi R, Hatamian-Zaremi A, Webster TJ. A review of fibrin and fibrin composites for bone tissue engineering. *Int J Nanomedicine*. 2017;Volume 12:4937-4961. doi:10.2147/IJN.S124671

141. Gonzalez de Torre I, Weber M, Quintanilla L, et al. Hybrid elastin-like recombinamer-fibrin gels: physical characterization and in vitro evaluation for cardiovascular tissue engineering applications. *Biomater Sci*. 2016;4(9):1361-1370. doi:10.1039/c6bm00300a

142. Sudha PN, Rose MH. Beneficial Effects of Hyaluronic Acid. In: *Advances in Food and Nutrition Research*. Vol 72. ; 2014:137-176. doi:10.1016/B978-0-12-800269-8.00009-9

143. Hemshekhar M, Thushara RM, Chandranayaka S, Sherman LS, Kemparaju K, Girish KS. Emerging roles of hyaluronic acid bioscaffolds in tissue engineering and regenerative medicine. *Int J Biol Macromol*. 2016;86:917-928. doi:10.1016/j.ijbiomac.2016.02.032

144. El-Sherbiny IM, Yacoub MH. Hydrogel scaffolds for tissue engineering: Progress and challenges. *Glob Cardiol Sci Pract*. 2013;2013(3):316-342. doi:10.5339/gcsp.2013.38

145. Nuttelman CR, Rice MA, Rydholm AE, Salinas CN, Shah DN, Anseth KS. Macromolecular Monomers for the Synthesis of Hydrogel Niches and Their Application in Cell Encapsulation and Tissue Engineering. *Prog Polym Sci*. 2008;33(2):167-179. doi:10.1016/j.progpolymsci.2007.09.006

146. Ferreira LS, Gerecht S, Fuller J, Shieh HF, Vunjak-Novakovic G, Langer R. Bioactive hydrogel scaffolds for controllable vascular differentiation of human embryonic stem cells. *Biomaterials*. Published online 2007. doi:10.1016/j.biomaterials.2007.01.021

147. Drury JL, Mooney DJ. Hydrogels for tissue engineering: Scaffold design variables and applications. *Biomaterials*. Published online 2003. doi:10.1016/S0142-9612(03)00340-5

148. Sensini A, Cristofolini L. Biofabrication of Electrospun Scaffolds for the Regeneration of Tendons and Ligaments. *Materials*. 2018;11(10):1963. doi:10.3390/ma11101963

149. Jin G, He R, Sha B, et al. Electrospun three-dimensional aligned nanofibrous scaffolds for tissue engineering. Published online 2018. doi:10.1016/j.msec.2018.06.065

150. Song R, Murphy M, Li C, Ting K, Soo C, Zheng Z. Current development of biodegradable polymeric materials for biomedical applications. *Drug Des Devel Ther*. 2018;Volume 12:3117-3145. doi:10.2147/DDDT.S165440

151. Seyednejad H, Ghassemi AH, van Nostrum CF, Vermonden T. Functional aliphatic polyesters for biomedical and pharmaceutical applications. *J Controlled Release*. 2011;152(1):168-176. doi:10.1016/J.JCONREL.2010.12.016

152. Cameron DJA, Shaver MP. Aliphatic polyester polymer stars: synthesis, properties and applications in biomedicine and nanotechnology. *Chem Soc Rev*. 2011;40(3):1761-1776. doi:10.1039/C0CS00091D

153. He L, Liao S, Quan D, et al. Synergistic effects of electrospun PLLA fiber dimension and pattern on neonatal mouse cerebellum C17.2 stem cells. *Acta Biomater*. 2010;6(8):2960-2969. doi:10.1016/J.ACTBIO.2010.02.039

154. Kijeńska E, Prabhakaran MP, Swieszkowski W, Kurzydlowski KJ, Ramakrishna S. Electrospun bio-composite P(LLA-CL)/collagen I/collagen III scaffolds for nerve tissue engineering. *J Biomed Mater Res B Appl Biomater*. 2012;100B(4):1093-1102. doi:10.1002/jbm.b.32676

155. Mahoney CM, Imbarlina C, Yates CC, Marra KG. Current Therapeutic Strategies for Adipose Tissue Defects/Repair Using Engineered Biomaterials and Biomolecule Formulations. *Front Pharmacol*. 2018;9:507. doi:10.3389/fphar.2018.00507

156. Gudapati H, Dey M, Ozbolat I. A comprehensive review on droplet-based bioprinting: Past, present and future. *Biomaterials*. 2016;102:20-42. doi:10.1016/j.biomaterials.2016.06.012

157. Skardal A, Atala A. Biomaterials for Integration with 3-D Bioprinting. *Ann Biomed Eng*. 2015;43(3):730-746. doi:10.1007/s10439-014-1207-1

158. Wang Z, Tian Z, Jin X, Holzman JF, Menard F, Kim K. Visible light-based stereolithography bioprinting of cell-adhesive gelatin hydrogels. In: *2017 39th Annual International Conference of the IEEE Engineering in Medicine and Biology Society (EMBC)*. Vol 2017. IEEE; 2017:1599-1602. doi:10.1109/EMBC.2017.8037144

159. Melchels FPW, Feijen J, Grijpma DW. A review on stereolithography and its applications in biomedical engineering. *Biomaterials*. 2010;31(24):6121-6130. doi:10.1016/j.biomaterials.2010.04.050

160. Panwar A, Tan L. Current Status of Bioinks for Micro-Extrusion-Based 3D Bioprinting. *Molecules*. 2016;21(6):685. doi:10.3390/molecules21060685

161. Ozbolat IT, Hospodiuk M. Current advances and future perspectives in extrusion-based bioprinting. *Biomaterials*. 2016;76:321-343. doi:10.1016/j.biomaterials.2015.10.076

162. Lode A, Meyer M, Brüggemeier S, et al. Additive manufacturing of collagen scaffolds by three-dimensional plotting of highly viscous dispersions. *Biofabrication*. 2016;8(1):015015. doi:10.1088/1758-5090/8/1/015015

163. Bertassoni LE, Cardoso JC, Manoharan V, et al. Direct-write bioprinting of cell-laden methacrylated gelatin hydrogels. *Biofabrication*. 2014;6(2):024105. doi:10.1088/1758-5082/6/2/024105

164. Jia J, Richards DJ, Pollard S, et al. Engineering alginate as bioink for bioprinting. *Acta Biomater*. 2014;10(10):4323-4331. doi:10.1016/j.actbio.2014.06.034

165. Zehnder T, Sarker B, Boccaccini AR, Detsch R. Evaluation of an alginate-gelatine crosslinked hydrogel for bioplotting. *Biofabrication*. 2015;7(2):025001. doi:10.1088/1758-5090/7/2/025001

166. Kolesky DB, Homan KA, Skylar-Scott MA, Lewis JA. Three-dimensional bioprinting of thick vascularized tissues. *Proc Natl Acad Sci*. 2016;113(12):3179-3184. doi:10.1073/pnas.1521342113

167. Petta D, Armiento AR, Grijpma D, Alini M, Eglin D, D'Este M. 3D bioprinting of a hyaluronan bioink through enzymatic-and visible light-crosslinking. *Biofabrication*. 2018;10(4):044104. doi:10.1088/1758-5090/aadf58

168. Pati F, Ha D-H, Jang J, Han HH, Rhie J-W, Cho D-W. Biomimetic 3D tissue printing for soft tissue regeneration. *Biomaterials*. 2015;62:164-175. doi:10.1016/j.biomaterials.2015.05.043

169. Chhaya MP, Melchels FPW, Holzapfel BM, Baldwin JG, Hutmacher DW. Sustained regeneration of high-volume adipose tissue for breast reconstruction using computer aided design and biomanufacturing. *Biomaterials*. 2015;52:551-560. doi:10.1016/j.biomaterials.2015.01.025

170. Im H, Kim SH, Kim SH, Jung Y. Skin Regeneration with a Scaffold of Predefined Shape and Bioactive Peptide Hydrogels. *Tissue Eng Part A*. 2018;24(19-20):1518-1530. doi:10.1089/ten.tea.2017.0489

171. Rutz AL, Hyland KE, Jakus AE, Burghardt WR, Shah RN. A Multimaterial Bioink Method for 3D Printing Tunable, Cell-Compatible Hydrogels. *Adv Mater*. 2015;27(9):1607-1614. doi:10.1002/adma.201405076

172. Hong S, Sycks D, Chan HF, et al. 3D Printing of Highly Stretchable and Tough Hydrogels into Complex, Cellularized Structures. *Adv Mater*. 2015;27(27):4035-4040. doi:10.1002/adma.201501099

173. Zhang M, Vora A, Han W, et al. Dual-Responsive Hydrogels for Direct-Write 3D Printing. *Macromolecules*. 2015;48(18):6482-6488. doi:10.1021/acs.macromol.5b01550

174. Hockaday LA, Kang KH, Colangelo NW, et al. Rapid 3D printing of anatomically accurate and mechanically heterogeneous aortic valve hydrogel scaffolds. *Biofabrication*. 2012;4(3):035005. doi:10.1088/1758-5082/4/3/035005

175. Pravin S, Sudhir A. Integration of 3D printing with dosage forms: A new perspective for modern healthcare. *Biomed Pharmacother*. 2018;107:146-154. doi:10.1016/j.biopha.2018.07.167

176. Thiol–Ene Photopolymerizations Provide a Facile Method To Encapsulate Proteins and Maintain Their Bioactivity | Biomacromolecules. Accessed

September 21, 2020. https://pubs-acs-org.proxy-um.researchport.umd.edu/doi/abs/10.1021/bm300671s

177. P. Singh S, P. Schwartz M, Y. Lee J, D. Fairbanks B, S. Anseth K. A peptide functionalized poly(ethylene glycol) (PEG) hydrogel for investigating the influence of biochemical and biophysical matrix properties on tumor cell migration. *Biomater Sci*. 2014;2(7):1024-1034. doi:10.1039/C4BM00022F

178. Lin C-C, Ki CS, Shih H. Thiol-norbornene photo-click hydrogels for tissue engineering applications. *J Appl Polym Sci*. 2015;132(8). doi:10.1002/app.41563

179. Shin H, Nichol JW, Khademhosseini A. Cell-adhesive and mechanically tunable glucose-based biodegradable hydrogels. *Acta Biomater*. 2011;7(1):106-114. doi:10.1016/j.actbio.2010.07.014

180. Rahman Z, Barakh Ali SF, Ozkan T, Charoo NA, Reddy IK, Khan MA. Additive Manufacturing with 3D Printing: Progress from Bench to Bedside. *AAPS J*. 2018;20(6):101. doi:10.1208/s12248-018-0225-6

181. Morrison RJ, Kashlan KN, Flanangan CL, et al. Regulatory Considerations in the Design and Manufacturing of Implantable 3D-Printed Medical Devices. *Clin Transl Sci*. 2015;8(5):594-600. doi:10.1111/cts.12315

182. Fairbanks BD, Schwartz MP, Halevi AE, Nuttelman CR, Bowman CN, Anseth KS. A Versatile Synthetic Extracellular Matrix Mimic via Thiol-Norbornene Photopolymerization. *Adv Mater*. 2009;21(48):5005-5010. doi:10.1002/adma.200901808

183. Shin H, Nichol JW, Khademhosseini A. Cell-adhesive and mechanically tunable glucose-based biodegradable hydrogels. *Acta Biomater*. 2011;7(1):106-114. doi:10.1016/j.actbio.2010.07.014

184. Hong S, Sycks D, Chan HF, et al. 3D Printing of Highly Stretchable and Tough Hydrogels into Complex, Cellularized Structures. *Adv Mater*. 2015;27(27):4035-4040. doi:10.1002/adma.201501099

185. Jin Y, Liu C, Chai W, Compaan A, Huang Y. Self-Supporting Nanoclay as Internal Scaffold Material for Direct Printing of Soft Hydrogel Composite Structures in Air. *ACS Appl Mater Interfaces*. 2017;9(20):17456-17465. doi:10.1021/acsami.7b03613

186. Liaw C-Y, Ji S, Guvendiren M. Engineering 3D Hydrogels for Personalized In Vitro Human Tissue Models. *Adv Healthc Mater*. 2018;7(4):1701165. doi:10.1002/adhm.201701165

187. Lin C-C, Ki CS, Shih H. Thiol-norbornene photo-click hydrogels for tissue engineering applications. *J Appl Polym Sci*. 2015;132(8). doi:10.1002/app.41563

188. Vats K, Marsh G, Harding K, Zampetakis I, Waugh RE, Benoit DSW. Nanoscale physicochemical properties of chain- and step-growth polymerized PEG hydrogels affect cell-material interactions. *J Biomed Mater Res A*. 2017;105(4):1112-1122. doi:10.1002/jbm.a.36007

189. Zhang Y, An D, Pardo Y, et al. High-water-content and resilient PEG-containing hydrogels with low fibrotic response. *Acta Biomater*. 2017;53:100-108. doi:10.1016/j.actbio.2017.02.028

190. Temenoff JS, Athanasiou KA, Lebaron RG, Mikos AG. Effect of poly(ethylene glycol) molecular weight on tensile and swelling properties of oligo(poly(ethylene glycol) fumarate) hydrogels for cartilage tissue engineering. *J Biomed Mater Res*. 2002;59(3):429-437. doi:10.1002/jbm.1259

191. Liu S, Li L. Ultrastretchable and Self-Healing Double-Network Hydrogel for 3D Printing and Strain Sensor. *ACS Appl Mater Interfaces*. 2017;9(31):26429-26437. doi:10.1021/acsami.7b07445

192. Yang F, Tadepalli V, Wiley BJ. 3D Printing of a Double Network Hydrogel with a Compression Strength and Elastic Modulus Greater than those of Cartilage. *ACS Biomater Sci Eng*. 2017;3(5):863-869. doi:10.1021/acsbiomaterials.7b00094

193. Zehnder T, Sarker B, Boccaccini AR, Detsch R. Evaluation of an alginate–gelatine crosslinked hydrogel for bioplotting. *Biofabrication*. 2015;7(2):025001. doi:10.1088/1758-5090/7/2/025001

194. Kuo C-Y, Wilson E, Fuson A, et al. Repair of Tympanic Membrane Perforations with Customized Bioprinted Ear Grafts Using Chinchilla Models. *Tissue Eng Part A*. 2017;24(5-6):527-535. doi:10.1089/ten.tea.2017.0246

195. Kuo C-Y, Shevchuk M, Opfermann J, et al. Trophoblast–endothelium signaling involves angiogenesis and apoptosis in a dynamic bioprinted placenta model. *Biotechnol Bioeng*. 2019;116(1):181-192. doi:10.1002/bit.26850

196. Arumugasaamy N, Navarro J, Kent Leach J, Kim PCW, Fisher JP. In Vitro Models for Studying Transport Across Epithelial Tissue Barriers. *Ann Biomed Eng*. 2019;47(1):1-21. doi:10.1007/s10439-018-02124-w

197. Arumugasaamy N, Ettehadieh LE, Kuo C-Y, et al. Biomimetic Placenta-Fetus Model Demonstrating Maternal–Fetal Transmission and Fetal Neural Toxicity of Zika Virus. *Ann Biomed Eng*. 2018;46(12):1963-1974. doi:10.1007/s10439-018-2090-y

198. Wang Y, Ma M, Wang J, et al. Development of a Photo-Crosslinking, Biodegradable GelMA/PEGDA Hydrogel for Guided Bone Regeneration Materials. *Materials*. 2018;11(8). doi:10.3390/ma11081345

199. Choi JR, Yong KW, Choi JY, Cowie AC. Recent advances in photo-crosslinkable hydrogels for biomedical applications. *BioTechniques*. 2019;66(1):40-53. doi:10.2144/btn-2018-0083

200. Iivarinen JT, Korhonen RK, Jurvelin JS. Experimental and numerical analysis of soft tissue stiffness measurement using manual indentation device - significance of indentation geometry and soft tissue thickness. *Skin Res Technol*. 2014;20(3):347-354. doi:10.1111/srt.12125

201. Töyräs J, Lyyra-Laitinen T, Niinimäki M, et al. Estimation of the Young's modulus of articular cartilage using an arthroscopic indentation instrument and ultrasonic measurement of tissue thickness. *J Biomech*. 2001;34(2):251-256. doi:10.1016/S0021-9290(00)00189-5

202. Arda K, Ciledag N, Aktas E, Aribas BK, Köse K. Quantitative assessment of normal soft-tissue elasticity using shear-wave ultrasound elastography. *AJR Am J Roentgenol*. 2011;197(3):532-536. doi:10.2214/AJR.10.5449

203. Eo S, Kim SS, Da Lio AL. Nipple Reconstruction With C-V Flap Using Dermofat Graft. *Ann Plast Surg*. 2007;58(2):137–140. doi:10.1097/01.sap.0000235445.86570.80

204. Yl C, E L, Th K, A R, Ca A, Ca V. Tissue-engineered nipple reconstruction. *Plast Reconstr Surg*. 1998;102(7):2293-2298. doi:10.1097/00006534-199812000-00002

205. Tanabe HY, Tai Y, Kiyokawa K, Yamauchi T. Nipple-Areola Reconstruction with a Dermal-Fat Flap and Rolled Auricular Cartilage. *Plast Reconstr Surg*. 1997;100(2):431–438.

206. Nakagawa T, Yano K, Hosokawa K. Cryopreserved Autologous Nipple-Areola Complex Transfer to the Reconstructed Breast. *Plast Reconstr Surg*. 2003;111(1):141–147. doi:10.1097/01.PRS.0000037863.12680.39

207. Collins B, Williams JZ, Karu H, Hodde JP, Martin VA, Gurtner GC. Nipple Reconstruction with the Biodesign Nipple Reconstruction Cylinder: A Prospective Clinical Study. *Plast Reconstr Surg Glob Open*. 2016;4(8). doi:10.1097/GOX.0000000000000846

208. Burdock GA. Safety assessment of hydroxypropyl methylcellulose as a food ingredient. *Food Chem Toxicol*. 2007;45(12):2341-2351. doi:10.1016/j.fct.2007.07.011

209. Lott JR, McAllister JW, Wasbrough M, Sammler RL, Bates FS, Lodge TP. Fibrillar Structure in Aqueous Methylcellulose Solutions and Gels. *Macromolecules*. 2013;46(24):9760-9771. doi:10.1021/ma4021642

210. Li L, Thangamathesvaran PM, Yue CY, Tam KC, Hu X, Lam YC. Gel Network Structure of Methylcellulose in Water. *Langmuir*. 2001;17(26):8062-8068. doi:10.1021/la010917r

211. Nasatto PL, Pignon F, Silveira JLM, Duarte MER, Noseda MD, Rinaudo M. Methylcellulose, a Cellulose Derivative with Original Physical Properties and Extended Applications. *Polymers*. 2015;7(5):777-803. doi:10.3390/polym7050777

212. Stalling SS, Akintoye SO, Nicoll SB. Development of photocrosslinked methylcellulose hydrogels for soft tissue reconstruction. *Acta Biomater*. 2009;5(6):1911-1918. doi:10.1016/j.actbio.2009.02.020

213. De Jong WH, Eelco Bergsma J, Robinson JE, Bos RRM. Tissue response to partially in vitro predegraded poly-L-lactide implants. *Biomaterials*. 2005;26(14):1781-1791. doi:10.1016/j.biomaterials.2004.06.026

214. Belleghem SV, Torres L, Santoro M, et al. Hybrid 3D Printing of Synthetic and Cell-Laden Bioinks for Shape Retaining Soft Tissue Grafts. *Adv Funct Mater*. 2020;30(3):1907145. doi:10.1002/adfm.201907145

215. Muschler GF, Raut VP, Patterson TE, Wenke JC, Hollinger JO. The Design and Use of Animal Models for Translational Research in Bone Tissue Engineering and Regenerative Medicine. *Tissue Eng Part B Rev*. 2009;16(1):123-145. doi:10.1089/ten.teb.2009.0658

216. Courtney T, Sacks MS, Stankus J, Guan J, Wagner WR. Design and analysis of tissue engineering scaffolds that mimic soft tissue mechanical anisotropy. *Biomaterials*. 2006;27(19):3631-3638. doi:10.1016/j.biomaterials.2006.02.024

217. Bružauskaitė I, Bironaitė D, Bagdonas E, Bernotienė E. Scaffolds and cells for tissue regeneration: different scaffold pore sizes-different cell effects. *Cytotechnology*. 2016;68(3):355-369. doi:10.1007/s10616-015-9895-4

218. Boehler RM, Graham JG, Shea LD. Tissue engineering tools for modulation of the immune response. *BioTechniques*. 2011;51(4):239-240, 242, 244 passim. doi:10.2144/000113754

219. Corradetti B, Taraballi F, Corbo C, et al. Immune tuning scaffold for the local induction of a pro-regenerative environment. *Sci Rep*. 2017;7(1):17030. doi:10.1038/s41598-017-16895-0

220. Macleod TM, Williams G, Sanders R, Green CJ. Histological evaluation of Permacol™ as a subcutaneous implant over a 20-week period in the rat model. *Br J Plast Surg*. 2005;58(4):518-532. doi:10.1016/j.bjps.2004.12.012

221. Gomes-Filho JE, Gomes BPFA, Zaia AA, Ferraz CR, Souza-Filho FJ. Evaluation of the biocompatibility of root canal sealers using subcutaneous implants. *J Appl Oral Sci*. 2007;15(3):186-194. doi:10.1590/S1678-77572007000300007

222. Su JT, Simpson SM, Sung S, et al. A Subcutaneous Implant of Tenofovir Alafenamide Fumarate Causes Local Inflammation and Tissue Necrosis in Rabbits and Macaques. *Antimicrob Agents Chemother*. 2019;64(3):e01893-19, /aac/64/3/AAC.01893-19.atom. doi:10.1128/AAC.01893-19

223. Kumka M, Bonar J. Fascia: a morphological description and classification system based on a literature review. *J Can Chiropr Assoc*. 2012;56(3):179-191.

224. Nestle FO, Di Meglio P, Qin J-Z, Nickoloff BJ. Skin immune sentinels in health and disease. *Nat Rev Immunol*. 2009;9(10):679-691. doi:10.1038/nri2622

225. Anderson JM. Chapter 4 Mechanisms of inflammation and infection with implanted devices. *Cardiovasc Pathol*. 1993;2(3, Supplement):33-41. doi:10.1016/1054-8807(93)90045-4

226. Brohim RM, Foresman PA, Hildebrandt PK, Rodeheaver GT. Early Tissue Reaction to Textured Breast Implant Surfaces: *Ann Plast Surg*. 1992;28(4):354-362. doi:10.1097/00000637-199204000-00010

227. Minutti CM, Knipper JA, Allen JE, Zaiss DMW. Tissue-specific contribution of macrophages to wound healing. *Semin Cell Dev Biol*. 2017;61:3-11. doi:10.1016/j.semcdb.2016.08.006

228. Witte MB, Barbul A. GENERAL PRINCIPLES OF WOUND HEALING. *Surg Clin North Am*. 1997;77(3):509-528. doi:10.1016/S0039-6109(05)70566-1

229. Fu X, Fang L, Li H, Li X, Cheng B, Sheng Z. Adipose tissue extract enhances skin wound healing. *Wound Repair Regen*. 2007;15(4):540-548. doi:10.1111/j.1524-475X.2007.00262.x

230. Rosengren A, Danielsen N, Bjursten LM. Reactive capsule formation around soft-tissue implants is related to cell necrosis. *J Biomed Mater Res*. 1999;46(4):458-464. doi:10.1002/(SICI)1097-4636(19990915)46:4<458::AID-JBM3>3.0.CO;2-I

231. Hammond JB, Kosiorek HE, Cronin PA, et al. Capsular contracture in the modern era: A multidisciplinary look at the incidence and risk factors after mastectomy and implant-based breast reconstruction. *Am J Surg*. Published online September 21, 2020. doi:10.1016/j.amjsurg.2020.09.020

232. Minami E, Koh IHJ, Ferreira JCR, et al. The Composition and Behavior of Capsules around Smooth and Textured Breast Implants in Pigs. *Plast Reconstr Surg*. 2006;118(4):874–884. doi:10.1097/01.prs.0000240878.24213.b7

233. Spano A, Palmieri B, Taidelli TP, Nava MB. Reduction of Capsular Thickness around Silicone Breast Implants by Zafirlukast in Rats. *Eur Surg Res*. 2008;41(1):8-14. doi:10.1159/000121501

234. Martin Y, Vermette P. Bioreactors for tissue mass culture: Design, characterization, and recent advances. *Biomaterials*. 2005;26(35):7481-7503. doi:10.1016/j.biomaterials.2005.05.057

235. Smallman A, Crittenden T, MiinYip J, Dean NR. Does nipple-areolar tattooing matter in breast reconstruction? A cohort study using the BREAST-Q. *JPRAS Open*. 2018;16:61-68. doi:10.1016/j.jpra.2018.01.003

236. Cha HG, Kwon JG, Kim EK, Lee HJ. Tattoo-only nipple-areola complex reconstruction: Another option for plastic surgeons. *J Plast Reconstr Aesthetic Surg JPRAS*. 2020;73(4):696-702. doi:10.1016/j.bjps.2019.11.011

237. Ashammakhi N, Ahadian S, Zengjie F, et al. Advances and Future Perspectives in 4D Bioprinting. *Biotechnol J*. 2018;13(12):1800148. doi:10.1002/biot.201800148

238. Gao B, Yang Q, Zhao X, Jin G, Ma Y, Xu F. 4D Bioprinting for Biomedical Applications. *Trends Biotechnol*. 2016;34(9):746-756. doi:10.1016/j.tibtech.2016.03.004

239. Sydney Gladman A, Matsumoto EA, Nuzzo RG, Mahadevan L, Lewis JA. Biomimetic 4D printing. *Nat Mater*. 2016;15(4):413-418. doi:10.1038/nmat4544